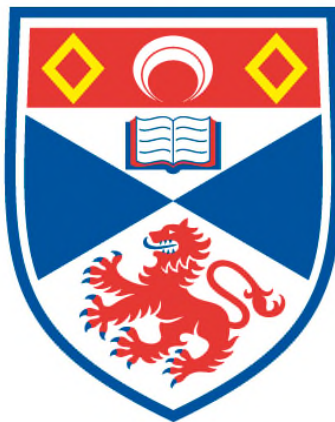


**SYNTHESIS, CHARACTERIZATION AND FORMATION
MECHANISM OF ALLOY AND METAL OXIDE
NANOPARTICLES**

Fengjiao Yu

**A Thesis Submitted for the Degree of PhD
at the
University of St Andrews**



2014

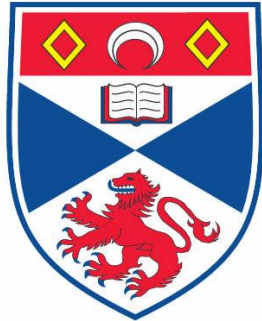
**Full metadata for this item is available in
St Andrews Research Repository
at:
<http://research-repository.st-andrews.ac.uk/>**

**Please use this identifier to cite or link to this item:
<http://hdl.handle.net/10023/6365>**

This item is protected by original copyright

Synthesis, Characterization and Formation Mechanism of Alloy and Metal Oxide Nanoparticles

Fengjiao Yu



This thesis is submitted in partial fulfilment for the degree of PhD
at the
University of St Andrews

Declaration

I, Fengjiao Yu, hereby certify that this thesis, which is approximately 37,700 words in length, has been written by me, that it is the record of work carried out by me and that it has not been submitted in any previous application for a higher degree.

I was admitted as a research student in September 2010 and as a candidate for the degree of PhD in September 2011; the higher study for which this is a record was carried out in the University of St Andrews between 2010 and 2014.

Date signature of candidate

I hereby certify that the candidate has fulfilled the conditions of the Resolution and Regulations appropriate for the degree of PhD in the University of St Andrews and that the candidate is qualified to submit this thesis in application for that degree.

Date signature of supervisor.....

In submitting this thesis to the University of St Andrews I understand that I am giving permission for it to be made available for use in accordance with the regulations of the University Library for the time being in force, subject to any copyright vested in the work not being affected thereby. I also understand that the title and the abstract will be published, and that a copy of the work may be made and supplied to any bona fide library or research worker, that my thesis will be electronically accessible for personal or research use unless exempt by award of an embargo as requested below, and that the library has the right to migrate my thesis into new electronic forms as required to ensure continued access to the thesis. I have obtained any third-party copyright permissions that may be required in order to allow such access and migration, or have requested the appropriate embargo below.

The following is an agreed request by candidate and supervisor regarding the electronic publication of this thesis:

Access to all of printed copy but embargo of all of electronic publication of thesis for a period of two years on the following ground: publication would preclude future publication.

Date signature of candidate

signature of supervisor

Acknowledgements

First of all, I would like to express my great gratitude to my supervisor, Prof. Wuzong Zhou. Without his guidance and help, this thesis would not have been possible. The offer to join his group on this project three years ago, brings me into the realm of nanomaterial research and the opportunity to study in the UK. His patience and helpful instruction has not only helped me acquire scientific knowledge and skills, but also on aspects of the right attitude towards life and the peace of mind.

I also would like to thank my industry supervisors: Dr. Ronan Bellabarba and Dr. Pascal Lignier from Sasol for their assistance, and Prof. Robert Tooze for his support.

I am grateful to those who have offered help in many ways. I would like to thank Dr. Christopher Baddeley for the discussion in IR spectra, Dr. Xiaoxiang Xu for photocatalysis testing, Mr. Ross Blackley for help in HRTEM and SEM and Mrs Sylvia Williamson for TGA results. I would also like to thank Mr Yuhui Chen for his patience and help in IR and ORR testing.

I would like to say thanks to all my group members: Heather Greer, Chang-Yang Chiang and Katherine Self, for their help and the good times. I'm grateful that Sasol funded my project and University of St Andrews who gave me a SORS scholarship award.

Last but not least, I owe profound gratitude to my parents and friends, whose love and understanding are really valuable to me. I feel so lucky to have their encouragement and support all the time.

Abstract

Metal nanoparticles can possess intriguing properties due to their nanoscale dimensions, and are intensively applied in research. With the development of synthetic systems, classic crystal growth theories become limited and cannot explain current conditions very well. The aim of this project is to find out the factors that influence crystal growth at the nanoscale and develop general methods to prepare shape-controlled nanomaterials.

The growth process of CuPt nanorods is studied and a ligand mediated mechanism is proposed. It reveals that surface ligands are crucial in guiding the one dimensional growth through their mutual interactions. Solvent effect is discovered to be able to control the nanoparticles morphology, by indirectly tuning the interactions between ligands and the surface of a particle. Based on this mechanism, titanate nanosheets with a monolayer thickness are prepared with the assistance of surface ligands. An effective, one-step method is developed to prepare CuPd nanowire networks, which demonstrates its versatility in the preparation of other alloyed networks. The growth process of CuPt nanoparticles are investigated, and show that the growth pathway can be a reversed, surface-to-core crystallization route. The effect of dealloying, including acid etching and galvanic replacement, is studied and used to fabricate nanoparticles with various morphologies.

The findings in this project highlight the influence of surface ligands in the synthesis of nanocrystals, provide new perspectives of crystal growth mechanisms and offer practical knowledge for nanostructuring materials.

Contents

Declaration	I
Acknowledgements	II
Abstract	III
Contents.....	IV

Chapter 1 Introduction.....	1
1.1 Theory of crystal growth	2
1.1.1 Classic crystal growth.....	2
1.1.2 Growth by aggregation and oriented attachment.....	5
1.1.3 Reversed crystal growth mechanism	7
1.2 Shape control of nanomaterials by alloying and dealloying	8
1.2.1 Alloyed nanoparticles	8
1.2.1.1 Mixing patterns of bimetallic nanoparticles	8
1.2.1.2 Applications of Pt-group bimetallic nanoparticles.....	9
1.2.1.3 Lattice strain of metallic nanoparticles	10
1.2.2 Dealloying: a versatile approach to control nanostructures.....	12
1.3 Characterization methods of nanomaterials	14
1.3.1 Microscopy	14
1.3.1.1 Electron microscopy.....	14
1.3.1.2 Scanning probe microscopy	15
1.3.2 Diffraction.....	16
1.3.3 Spectroscopic analysis	17
1.4 Aims and overview	17
References.....	18

Chapter 2 Experimental	22
2.1 Synthetic methods for metallic nanoparticles	22
2.2 Characterization techniques	23
2.2.1 High resolution transmission electron microscopy.....	23
2.2.2 Scanning electron microscopy.....	31
2.2.3 Energy dispersive X-ray spectroscopy	33
2.2.4 X-ray diffraction	35
2.2.5 Infrared spectroscopy.....	38
2.2.6 Thermogravimetric analysis	40
References.....	41

Chapter 3 Ligand Mediated Synthesis of Cu, Pt, Pd Alloyed Nanoparticles	43
3.1 Ligand mediated growth of CuPt nanorods	43
3.1.1 Introduction.....	43
3.1.2 Experimental section	44
3.1.3 CuPt nanorods and growth process.....	48
3.1.4 Crystallographic orientation of CuPt nanorods	52
3.1.5 Effect of surface ligands	54
3.1.6 Two-step synthesis.....	58
3.1.7 Surface characterization of the CuPt nanorods.....	60
3.1.8 Proposed formation mechanism	64
3.1.9 Photocatalysis performance	67
3.2 Ligands capped monometallic, bimetallic and trimetallic nanoparticles	68
3.2.1 Experimental section	69
3.2.2 Monometallic Cu and Pt nanoparticles.....	70
3.2.3 Trimetallic CuPdPt nanospheres.....	72
3.2.4 Bimetallic CuPd and PdPt nanoparticles	74
3.3 Solvent effect	76
3.3.1 Experimental section	76
3.3.2 Solvent effect in the synthesis of CuPdPt nanospheres	78
3.3.3 Solvent effect in the synthesis of Pt nanoparticles	79
3.3.4 Solvent effect in synthesis of CuPd nanoparticles.....	82
3.4 Implication of ligand-mediated growth mechanism	83
References.....	85
Chapter 4 Ligand Assisted Formation of Nanosheets Unrolled from Titanate Nanotubes	88
4.1 Introduction.....	88
4.2 Experimental section.....	89
4.3 Titanate nanotubes	91
4.4 Unrolling nanotubes into nanosheets	93
4.4.1 Unrolling tubes with primary amine ligands	94
4.4.2 Unrolling nanotubes with bulky ligands.....	96
4.4.3 Unrolling with assistance of ultrasonication	99
References.....	100
Chapter 5 One-step Synthesis and Shape-Control of CuPd Nanowire Networks	102
5.1 Introduction.....	102
5.2 Experimental section.....	103
5.3 CuPd nanowire networks	105
5.4 Growth process	108
5.5 Surface characterization and shape control.....	111

5.6 Electrochemical performances	113
5.7 Other Pd-based nanoparticles	115
5.7.1 Pd	115
5.7.2 AgPd	118
5.7.3 AuPd and AuCuPd.....	119
References.....	124
Chapter 6 Alloying and Dealloying of CuPt Nanoparticles.....	126
6.1 Introduction.....	126
6.2 Experimental section.....	127
6.3 Reversed crystal growth of CuPt nanoparticles	129
6.4 Alloying Cu and Pt by varying nominal ratios	134
6.5 Size and composition dependent morphology of dealloyed nanoparticles	141
6.5.1 Dealloying of CuPt nanospheres	141
6.5.2 Dealloying of Cu ₇ Pt ₃ nanoparticles	142
References.....	144
Chapter 7 Conclusions and Future Work.....	146
7.1 Conclusions.....	146
7.2 Future work.....	148
Publications.....	149

Chapter 1 Introduction

The last two decades have witnessed explosions in nanotechniques and nanoscience for controllable synthesis, manipulating structures and biological applications. Nanomaterials, defined as having at least one dimension between 1 and 100 nanometers, can have exceptional properties due to quantum size effect and surface effect.¹⁻³

Based on their structural dimensions, nanomaterials are classified into different types: zero-dimensional (0D), one-dimensional (1D), two-dimensional (2D) and three-dimensional (3D). For example, 0D structures are sized in the nanoscale in all three dimensions, such as quantum dots, nanospheres and nanocubes. Other materials nanosized in only two dimensions, such as nanowires and nanorods, are known as 1D materials. Nanosheets and graphene are popular 2D materials, and metal organic frameworks (MOFs) are intensively studied as a kind of 3D materials.

Metal elements constitute more than two thirds of the periodic table. Most metals have the same face-centered-cubic lattice, which is highly symmetric and easy for characterization. Metal nanocrystals possess intriguing properties that could be exploited in sensing,⁴ catalysis,⁵⁻¹⁰ memory and logic circuits¹¹ and so on.

Metallic nanoparticles with various shapes such as, pyramid, cubes, rods with circular, rectangular or pentagonal cross section, polyhedra, truncated polyhedra, to name a few have been developed and successfully synthesized in the last few decades. The underlying growth mechanisms and understanding of these synthetic processes are yet less explored in comparison with achievements in fabricating nanomaterials. In contrast to numerous organic compounds that can be designed, metallic nanocrystals have limited structures and chemical composition. The chemical reactions applied in the synthesis of nanocrystals are usually quite simple, but the nucleation and growth process behind them are extremely complex. The rapid growth of nanomaterials also increases the difficulty in investigations. The growth mechanism can be found by observations of the nanostructures and detailed investigations involving size,

morphology and phase transformation. Despite that solution-phase synthesis of crystals is a familiar process and plenty of research work has been done, many problems still remain unsolved.

In this thesis, alloyed metallic nanoparticles with a controlled morphology have been prepared. In order to reveal the growth mechanism, detailed growth processes have been studied. These results provide new knowledge about the effect of surface ligands on shape evolution, as well as alloying and dealloying of Pt- and Pd-based nanoparticles. A brief background on crystal growth and alloyed nanoparticles is given in the following sections, organized as: an overview of crystal growth mechanisms, features and types of bimetallic nanoalloys produced by alloying and dealloying and common characterization methods for nanomaterials.

1.1 Theory of crystal growth

The classic crystal growth theories have been accepted for about one hundred and twenty years. They are widely applied to explain particle coarsening for many materials, which are prepared in systems that allow significant dissolution of crystals into the solution medium. The development of new synthetic systems and the usage of capping agents, however, can change the saturation state of the solutes. With more and more research on crystal evolution and growth behaviors, the Ostwald ripening mechanism cannot well explain all the models. Therefore, other crystal growth routes have emerged as new mechanisms, and have been demonstrated in many systems.

1.1.1 Classic crystal growth

Classically, a crystal is known to develop from the repeated addition of atoms or monomers to an existing nucleus. Nucleation can be generally classified into three types: homogeneous nucleation, heterogeneous nucleation and secondary nucleation. In most typical

preparations of metal nanoparticles, homogeneous nucleation occurs when the solution is supersaturated. The change of overall free energy, ΔG , for spherical particles can be described by the following equation, in which the first term is the released energy associated with the new volume, and the second term is the energy consumed to create new interfaces:

$$\Delta G = -\frac{4}{V}\pi r^3 k_B T \ln(S) + 4\pi r^2 \gamma$$

where

V : molecular volume of the precipitation r : radius of the nucleus

k_B : Boltzmann constant S : saturation ratio

γ : surface free energy per unit surface area T : temperature

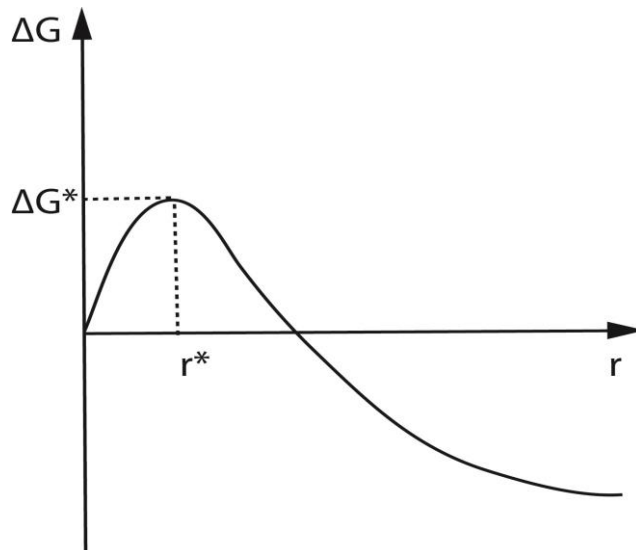


Figure 1.1 Plot of free energy ΔG as a function of nuclei radius, r . The maximum value of ΔG^* is obtained at a critical size r^*

Plotting ΔG against the nuclei radius r will give a curve as shown in **Figure 1.1**. When $S > 1$, the maximum value of ΔG^* is obtained at a critical size r^* . When S is constant, particles with a size larger than r^* will continue to grow with further decreasing free energy, while

particles with $r < r^*$ will dissolve. The critical size r^* can be calculated by setting $d\Delta G / dr = 0$ and can be described by equation:

$$r^* = \frac{2V\gamma}{3k_B T \ln(S)}$$

From this equation it can be concluded that the critical size r^* decreases with increasing S .

It is not yet clear how exactly nuclei develop from precursors. LaMer and colleagues¹² proposed a mechanism for nucleation *via* a decomposition route in 1950, which is very common in the synthesis of metallic nanoparticles. This mechanism suggests that the concentration of atoms increases with the decomposition of precursor, until the supersaturation point is reached and nuclei will form. When the concentration of atoms drops below that of minimum supersaturation, nucleation will stop.

As the reaction proceeds, Ostwald ripening¹³ will occur due to the low concentration of remaining reactants. Since the saturation ratio, S is smaller, resulting in larger r^* . Particles larger than this new critical size will grow, but ones smaller than r^* will reduce their sizes and eventually dissolve. No more reactant is supplied and the critical size will continue to increase. As a result, large particles grow at the expense of small ones.

Shape evolution occurs during the crystal growth and the relative growth rate of different facets is one of the factors that determine the morphology of crystals. The Bravais-Friedel-Donnay-Harker (BFDH) law¹⁴⁻¹⁶ states that the final morphology of a crystal is dominated by the slow-growing facets as the fast-growing facets will grow out and are usually not displayed in the final morphology. The growth rate is proportional to the surface attachment energy, which is released when one slice is attached to a growing crystal surface.¹⁷ The highest attachment energies lead to the fastest growing surfaces, and usually disappear in the final morphology. From another point of view, The Wulff construction^{18, 19} indicates that the equilibrium shape of a crystal in inert gas or vacuum is a polyhedron that minimizes its total surface energy. Wulff theorem is more general than the BFDH mechanism, and does not set restrictions on crystal growth rates. For example, hollow crystals can also adopt characteristic

habits to minimize the surface energy. Although the Wulff theorem was established more than 100 years ago, it is still a powerful tool to predict and understand the shape of particles. In the last few decades, synthesis of shape-controlled nanoparticles has attracted huge interest, and extensions and modifications of the Wulff theorem have been made. In all these models, the thermodynamically stable shape is independent of the particle size, except significant strain effect is involved. A discussion about the strain effect later will be made in this chapter.

Both the BFDH and the Wulff theorems are correct. However, the former is a kinetic measurement; the latter is from the perspective of thermodynamic measurement.

1.1.2 Growth by aggregation and oriented attachment

In addition to classical crystal growth as an amplification process *via* atom deposition, particles can also grow by aggregation of as-formed building units in a mesoscopic assembly process.²⁰ The two different growth modes are illustrated in **Figure 1.2**. This process takes place through the coalescence of primary nanoparticles into aggregates. The interactions between the primary building units are dependent on many factors, for example, dipole-dipole interactions, electrostatic and van de Waals forces, and in many cases the solvent effect can't be ignored.

Solution phase synthesis is a very common method to prepare nanocrystals, in which process capping agents are usually involved. Many research investigations have demonstrated that crystal habit can be influenced by selective adsorption of capping agents on crystal faces, which leads to inhibition of growth. Moreover, the primary particles can be well stabilized by introducing organic ligands, which have a strong attraction with the inorganic surfaces of the primary particles. As a result, hybrid particles with an inorganic core and an organic shell anchored to the surface are produced. When these hybrid primary particles assemble, they are influenced by van der Waals forces, steric hindrance and hydrophobic/hydrophilic interactions from the chains of the adsorbed ligands.

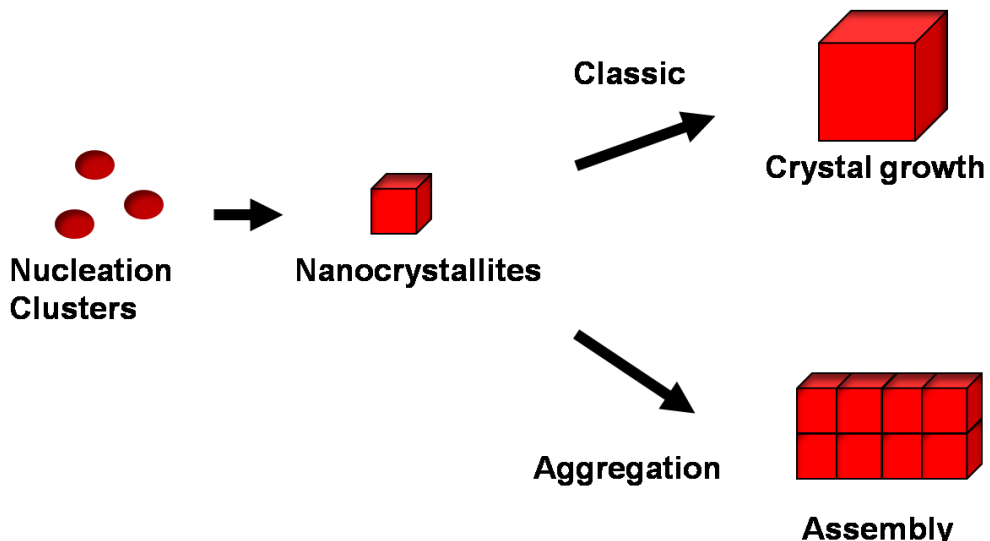


Figure 1.2 Illustration of alternative growth mechanisms: classic crystal growth and aggregation.

If the primary particles assemble by sharing the same crystallographic orientation, single crystals are produced in this oriented attachment (OA) mechanism. Ever since Penn and Banfield^{21, 22} proposed this OA mechanism, anisotropic materials fabricated by the self-assembly of nanoparticles are in abundance.²³ The most reported 1D materials are usually growing along a specific crystallographic orientation driven by elimination of high energy facets, such as growth along the [001] zone axis of TiO₂ nanorods and [111] of Au nanowires, etc.^{24, 25} In addition, stress caused by mismatch and defects at the interface could induce the building units to rotate and adjust their orientations, in order to be well aligned in a single-crystal-like manner.²⁶ The kinetic model of OA is also developed, in which the coalescence of primary particles are taken as a collision between molecules.²⁷ Adding ligands or capping agents are believed to be important factors to suppress the Ostwald ripening process and facilitate OA.

1.1.3 Reversed crystal growth mechanism

Recent studies reveal that crystal growth can also follow a reversed route, in which crystallization extends from surface to core.²⁸⁻³⁰ This reversed crystal growth mechanism is illustrated in **Figure 1.3**.

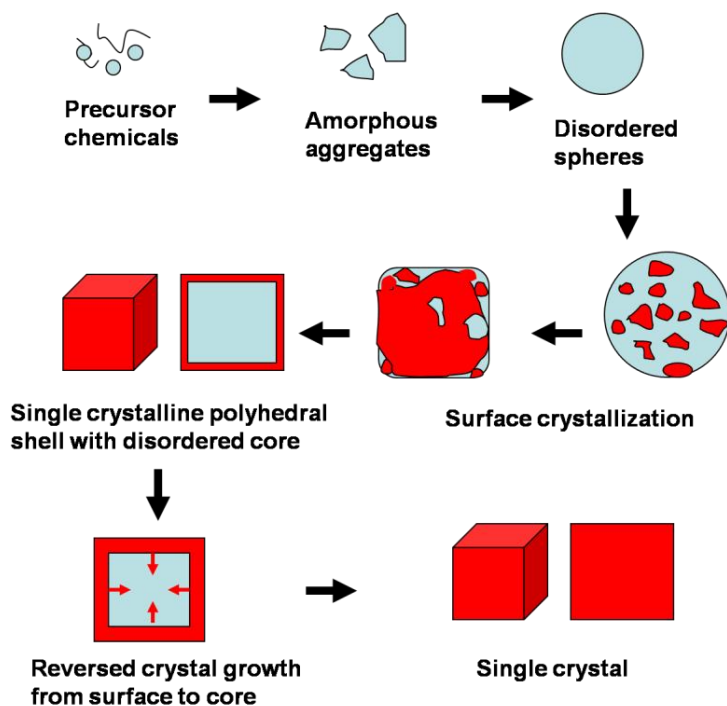


Figure 1.3 Illustration of reversed crystal growth mechanism demonstrating that crystallization extends from surface to core.

The use of surfactants in synthesis can enhance the aggregation in the early stages and lead to crystallization on the surface of the disordered aggregates. Since the surface of the disordered sphere is in contact with solution, thus it is more active than the interior. When surface crystallization covers the whole surface of the aggregate, a core-shell particle is formed with a characteristic polyhedral morphology involving a disordered core. The crystallization will then extend from surface to core, resulting in a single crystal at last. It is noteworthy that the mass diffusion and transportation will become difficult when the surface is covered

completely by the crystalline shell. High density crystal is produced from consuming the disordered core. Therefore, this transformation usually leaves behind a hole in the core of each particle.

The first reported example of reversed crystal growth was zeolite analcime with an icositetrahedral morphology.²⁸ Since then the reversed crystal growth has been observed in many other materials, such as perovskites,³¹ organic crystals³² and zeolite A³³. In fact, Wulff's theory can also explain the formation of characteristic polyhedral morphology *via* reversed crystal growth. A crystal habit is a consequence of minimizing surface energy, independent of the inner structure. For example, zeolite analcime²⁸ has an icositetrahedral morphology with a very thin single-crystalline shell and disordered interior.

1.2 Shape control of nanomaterials by alloying and dealloying

1.2.1 Aligned nanoparticles

Bimetallic alloyed nanoparticles, which are composed of two distinct metal elements, are emerging as a new class of nanomaterials. Their properties are excellent and in general enhanced due to the synergistic effect, compared to the monometallic counterparts.³⁴ Alloying provides an attractive prospect for nanoparticle design to reduce cost, improve activity and retain good stability. For instance, the high cost is one of the major barriers for commercialization of precious metal containing electrodes or catalysts. Replacing rare precious metals with a less expensive alloy and retaining close efficiency has been stimulating worldwide interest.

1.2.1.1 Mixing patterns of bimetallic nanoparticles

Based on the mixing type of two different metals, bimetallic nanoparticles can be classified into core-shell, heterostructure, and intermetallic or alloyed structures.

Core-shell structure (**Figure 1.4a**) consists of a core formed by one type of metal atoms A and surrounded by a shell of another kind of metal atoms B. It is usually formed *via* the following process: metal ions A are reduced first to form an inner core whilst the other kind of metal atom B prefers to nucleate and subsequently grow around the core to form a shell. Nevertheless, the two types of metal atoms can go through individual nucleation and grow separately under appropriate conditions. Heterostructure (**Figure 1.4b**) is produced when segregated A and B clusters share the interface.

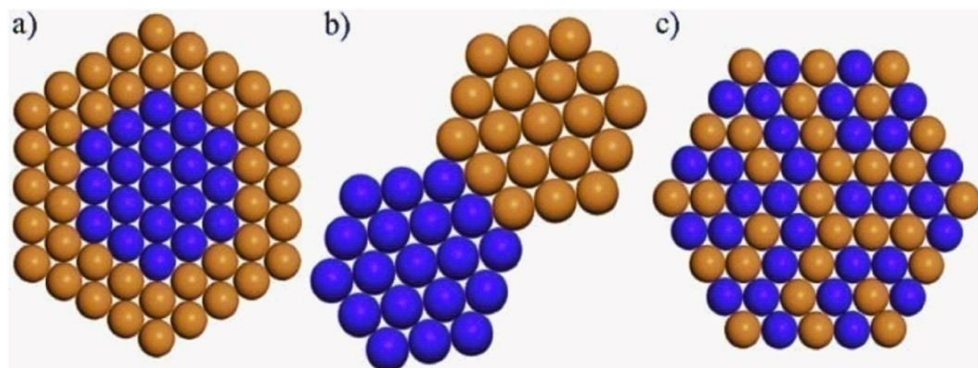


Figure 1.4 Bimetallic nanoparticles with different structures: (a) core-shell, (b) heterostructure and (c) alloyed structure.

The alloyed structure as shown in **Figure 1.4c** consists of either ordered or randomly mixed A and B atoms. Powder X-ray diffraction (XRD) patterns can distinguish alloys from core-shell or heterostructure bimetallic nanoparticles: the latter structures present two sets of peaks corresponding to the characteristic diffraction from the two different metals. In the XRD pattern of alloy, however, these individual peaks will be absent and new diffraction peaks appear which are from the alloyed structure.

1.2.1.2 Applications of Pt-group bimetallic nanoparticles

Bimetallic nanoparticles have fascinating properties and have been widely applied in a number of fields, such as catalysis, optical devices, biodiagnostics and so on.³⁴ Pt-group metals have significantly important roles in catalysis and there are enormous research results. Herein we mainly focus on the applications of CuPd and CuPt, which are studied in this thesis. CuPd

nanoalloy is a very attractive catalyst. For example, Zhang³⁵ and Wang³⁶ demonstrated electrocatalytic activity of CuPd nanoparticles towards oxygen reduction reaction (ORR). CuPd nanoalloys supported on TiO₂ are excellent photocatalysts for hydrogen generation to synthesize ammonia.³⁷ In addition, CuPd bimetallic nanoparticles are outstanding catalysts in applications such as the combustion of methane³⁸ and hydration of acrylonitrile.³⁹ On the other hand, CuPt bimetallic nanoparticles have shown enhanced catalytic performances in selective oxidation of CO in excess hydrogen,⁴⁰ ORR in polymer electrolyte membrane fuel cells (PEMFCs),⁵ methanol oxidation,⁴¹ heterogeneous NO_x reduction⁶ and many other reactions.

1.2.1.3 Lattice strain of metallic nanoparticles

Surface lattice strain is a principle factor which affects the intrinsic properties of metallic nanoparticles.⁴²⁻⁴⁴ Strains can form in the overlayer when growing one metal on top of another, caused by the lattice mismatch. Strain can also come from the local deformation of single metal crystals.⁴⁵ Such stain can change the adsorption ability of the metal by influencing the bonding structure. Other reasons why strains are induced in metallic nanoparticles are, for example, CO gas molecules can restructure the metal surface,⁴⁶ but lattice mismatch contributes the most to strain in bimetallic nanoalloys.⁴⁴ For instance, core-shell bimetallic nanoparticles have strains generated from the lattice mismatch between core and shell metals. Compressive or tensile strains also form in alloyed nanoparticles, when another kind of atoms with a different size substitutes in the lattice points.

Surface stress, f_{rr} can be described by the Laplace–Young law⁴⁷ as following

$$f_{rr} = -\frac{3}{2} \frac{\Delta a}{a} \frac{r}{K}$$

in which $\Delta a/a$ is the relative lattice parameter change, a is the lattice parameter, r is the radius of nanoparticles and K is the bulk compressibility of the metal.

Surface energy per unit area, γ can be described as the total surface energy divided by the surface area of the cluster:

$$\gamma = \frac{N\epsilon_{\text{bulk}} - E_{\text{cluster}}}{4\pi r^2}$$

ϵ_{bulk} bulk cohesive energy

N number of atoms

E_{cluster} total binding energy of the cluster

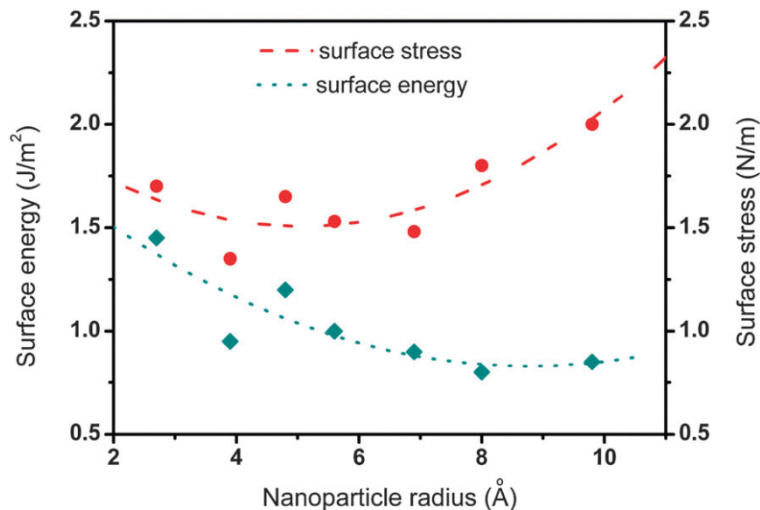


Figure 1.5 Surface energy per unit area and surface stress of Al nanoparticles plotted according to DFT calculations.^{44, 48} (Image reproduced with permission from ref. 44)

Density functional theory (DFT) calculations of Al nanoparticles⁴⁸ as shown in **Figure 1.5** illustrate the relationship between cluster radius and surface energy and surface stress. Generally, the surface energy increases as the particle size decreases. In contrary, surface stress decreases when particle size decreases. Surface strain can cause shift of the d-band center in transition metals,⁴⁹ which is one explanation why some activity is only possessed by metallic nanoparticles with a small size.

1.2.2 Dealloying: a versatile approach to control nanostructures

Dealloying is defined as the selective removal of one active metal element out of an alloy. In history, people used dealloying for depletion gilding. In 1927, Murray Raney, an American engineer, developed the well-known Raney Ni catalyst for hydrogenation reactions by dealloying Ni-Al alloy with sodium hydroxide to produce a porous structure.⁵⁰ Recently dealloying has attracted renewed attention as an effective method to fabricate nanostructures especially core-shell and nanoporous nanomaterials.⁵¹⁻⁵⁴

Dealloying methods include electrochemical dealloying and chemical dealloying which usually involves acid etching. As an example for the former, Strasser and co-workers electrochemically dealloyed Pt bimetallic alloys and used the core-shell product as fuel cell electrocatalyst. This showed high activity towards oxygen reduction reactions.^{5, 52} They suggested the lattice strain in the Pt shell resulted in a shift of the *d* band of the Pt atoms and an increase of the catalytic activity. In comparison, chemical dealloying has lower requirements for instruments and can be easily carried out. For instance, Wang *et al.* dealloyed Pt-Ni and other Pt bimetallic nanocrystals with nitric acid and produced nanoporous particles with increased surface areas.⁵¹

Galvanic replacement is another common method that has similar effect as dealloying. Different from chemical and electrochemical dealloying, galvanic replacement is based on reduction potentials of the two metals involved. It is a redox process, in which one metal is oxidized and corroded by the ions of the second metal. Subsequently, the second metal is reduced and deposited on the surface of first metal.

Figure 1.6 illustrates the processes of galvanic replacement and dealloying. Both alloying and dealloying processes are involved in the galvanic replacement. Ions with a higher redox potential, denoted as A ions, deposit on the surface of the other metal (say B metal) to produce an incomplete layer. Segregated or epitaxial A layer can form, depending on whether the lattice constants of two metals match well. Accompanying the deposition of A atoms, alloying between A and underlying B atoms may also take place. Continuous dissolution of B

atoms will generate vacancies. As the vacancies coalesce, porous or hollow structures can be obtained. Further galvanic replacement can also dealloy B atoms out of the A-B alloy wall.

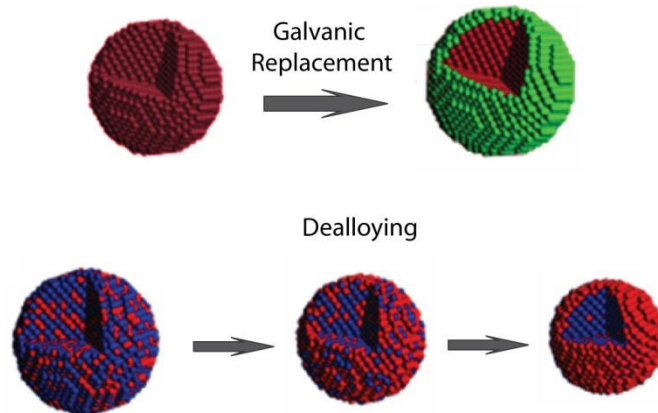


Figure 1.6 Illustration of galvanic replacement and dealloying processes.⁵⁵

A good example is the replacement of Pd^{2+} or Pt^{2+} ions and Ag nanocubes,⁵⁶ which is illustrated in **Figure 1.7a**. Xia and co-workers reported that the reaction of Ag nanocubes with Pd^{2+} produced single-crystalline PdAg alloyed nanoboxes with smooth surfaces (**Figure 1.7b**). However, reaction with Pt^{2+} ions produced polycrystalline nanoboxes with Pt nanoparticles attached to the surface (**Figure 1.7c**). This is because Pt doesn't interfuse into the Ag atoms. Instead, Pt atoms form islands, due to the much higher bonding energy of Pt-Pt (307 kJ/mol) compared to that of Pt-Ag (218 kJ/mol). On the other hand, the bonding energy of Pd-Ag is 137 kJ/mol, and is favored over Pd-Pd (100 kJ/mol). As a result, conformal AgPd alloy, rather than segregated phases formed.

Xia and co-workers have also reported many other successful preparations of various structures formed by a galvanic replacement reaction, such as nanocages, nanorattles and nanoshells with multiple walls.⁵⁸⁻⁶⁰

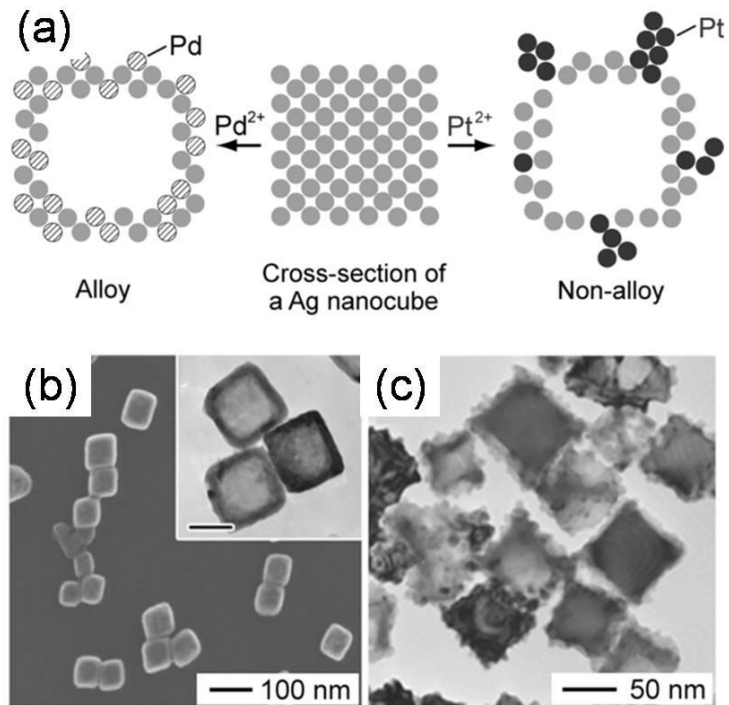


Figure 1.7 (a) Illustration of the galvanic replacement between Ag nanocubes and Pt or Pd ions. (b) SEM image of nanoboxes prepared after reaction with Pd ions, inset is a TEM image. (c) TEM image of bumpy nanoboxes prepared after reaction with Pt ions. (Image reproduced with permission from ref. 57 and 58)^{57, 58}

1.3 Characterization methods of nanomaterials

1.3.1 Microscopy

Microscopy is an important technique to obtain information on the size distribution, morphology and structure of nanoparticles.

1.3.1.1 Electron microscopy

Transmission electron microscopy (TEM) is particularly powerful for characterization of nanoparticles. Electrons pass through the specimen during TEM, and are recorded by a charge coupled device to produce an image. Other than the morphology of nanoparticles, TEM

also offers resolution down to the angstrom scale to reveal the atomic structure. Chemical information of the nanocrystals can be provided with the assistance of EDX on the TEM. Nowadays, in situ observation is possible in TEM, and live monitoring of growth process has been achieved.⁶¹ In situ observations are performed in liquid cells. On the stage, a cell entraps a little amount of liquid containing precursors. The growth of nanocrystals is then initiated by the electron beam.⁶² In this way, the growth can be studied in real time.

One advantage of TEM over scanning tunneling microscopy (see the introduction of STM below) is the high contrast between nanocrystals and surface capping organic polymers or molecules. As a result, TEM is able to provide clear images of atom distributions even when the nanoparticles surface is capped.

Bright field and dark field are two modes in TEM operation. In bright field images, the transmitted electron beam contributes most, but in dark field the diffracted beam is selected for imaging. Dark field imaging is helpful when studying bimetallic nanocrystals such as Au-Ag, in which the two elements have close lattice constants. It is hard to distinguish between them from bright field TEM images. The difference in their atomic numbers leads to different electron scattering abilities, and will produce differences in contrast in dark field images to reveal their structure. The high angle annular dark field (HAADF) technique is commonly used to characterize core-shell structured bimetallic nanoalloys.⁵²

In **scanning electron microscopy (SEM)**, an electron beam is scanned across the specimen, which generates secondary electrons to form images. SEM images usually have lower resolution, but better depth of view. SEM is more suitable to image bulk samples and can show 3D morphological information.

1.3.1.2 Scanning probe microscopy

Scanning probe microscopy provides high resolution images of surfaces, using a sharp tip to scan across the surface. Topography and surface chemistry information can be mapped out. The advantage of scanning probe microscopy is that the operation can be done under ambient or liquid environment.

Scanning tunneling microscopy (STM) is a technique based on the theory of quantum tunneling, that is, when the conductive tip is brought very close to the surface of a conductive material, tunneling current can flow between them after a voltage is applied. The current is sensitive to the position of the tip. The image is acquired by monitoring the tip scanning across the surface. STM is widely applied in studies on the adsorption of molecules on metal surfaces.

Atomic force microscopy (AFM) is another probe microscopy technique. When the tip approaches closely to a specimen surface, the small force between them will be sensed and recorded, to further produce images of the surface. The advantage of AFM over STM is that the specimen does not necessarily have to conduct. One application of AFM is to determine the thickness of 2D nanosheets by examining the height profile.

1.3.2 Diffraction

X-ray diffraction (XRD) is an effective tool to study nanocrystals. It offers information on crystallinity, particle size, lattice parameters and chemical composition. The shift of peaks in XRD indicates the change of lattice parameters. Taking CuPt nanoalloys as an example, increase of the Cu content will lead to a shift towards the high angle 2θ direction, due to a decrease of the lattice parameters. XRD can also distinguish alloyed structures from core-shell and heterostructures. The latter structures have two sets of XRD peaks from the parent metals.

XRD patterns are statistically an average from large amount of atoms, and reflect the macroscopical property of the material. On the other hand, electron diffraction, which uses electrons as the incident beam, can be carried out on individual particles. The diffraction produces reciprocal lattice points, from which the geometry and crystal structure can be obtained.

1.3.3 Spectroscopic analysis

Energy-dispersive X-ray spectroscopy (EDX) is widely used for elemental analysis, and is usually applied in conjunction with SEM and TEM. The principle of EDX is based on each element having unique peaks in the X-ray spectrum. Nanoparticles' chemical composition can be examined with EDX, and elemental mapping can also be performed with EDX to give the elemental distribution.

X-ray photoelectron spectroscopy (XPS) is an analytical technique used for surface characterization. XPS relies on the photoelectric effect. Electrons are ejected from a material following irradiation by X-rays. By measuring the number and the kinetic energy of the escaped electrons, information such as the chemical composition, binding mode of ligands on surfaces and the electronic state of elements in the specimen can be found.

Infrared spectroscopy (IR) is very frequently used to study the infrared spectrum of molecules adsorbed on the surfaces of metal nanoparticles. IR spectroscopy investigates the vibration of molecules, and can probe surface composition and structure.

Ultraviolet-visible spectroscopy (UV-vis) is often used to investigate the optical properties, surface plasmon resonance in particular, of nanoparticles. Shift of peaks in UV-vis spectrum can be used to study the structure of nanoparticles. For example, peaks in the UV-vis spectrum of hybrid core-shell CdSe nanoparticles with dye molecules in the shell shifted towards longer wavelength compared to the CdSe nanoparticles.⁶³

1.4 Aims and overview

Nanomaterials have been intensively studied. It is largely due to the diversity, complexity and rapid growth rate of nanoparticles that our current understanding of synthesis and growth pathways is still limited. The aim of this project is to study the growth process, shape control, structures and catalytic applications of Pt-group based bimetallic nanoparticles. The idea is to

reveal the growth mechanism of metallic nanoparticles and the effect of surface ligands, and subsequently use the knowledge to design nanostructures.

This project first investigates how surface ligands influence the shape of CuPt nanorods. The objectives are: (1) to reveal the underlying growth mechanism and find out the driving force for 1D growth, (2) using the ligand interaction between solvent and metal to interpret the ligand effect on nanoparticle morphology.

With this understanding, the next target is to synthesize monolayer titanate nanosheets with the assistance of ligands. This work aims to find out suitable experimental conditions such as the solvent and the surface ligands, for yielding nanosheets.

A one-step synthetic method of CuPd nanowire networks is demonstrated in chapter 5. This section of work aims to reveal the growth process, and to tune the morphology by varying the surface ligands and solvent. To study the versatility of this synthetic method, Pd based nanoparticles alloyed with another metal are prepared.

Chapter 6 investigates the alloying and dealloying of CuPt nanoparticles. The goal is to find out the evolution of particles in different growth stages, and reveal the factors affecting the morphology and composition in alloying and dealloying.

References

1. A. P. Alivisatos, *Science*, 1996, **271**, 933-937.
2. M. A. El-Sayed, *Acc. Chem. Res.*, 2004, **37**, 326-333.
3. C. B. Murray, C. R. Kagan and M. G. Bawendi, *Annu. Rev. Mater. Sci.*, 2000, **30**, 545-610.
4. F. Patolsky and C. M. Lieber, *Mater. Today*, 2005, **8**, 20-28.
5. S. Koh and P. Strasser, *J. Am. Chem. Soc.*, 2007, **129**, 12624-12625.
6. S. Zhou, B. Varughese, B. Eichhorn, G. Jackson and K. McIlwrath, *Angew. Chem. Int. Ed.*, 2005, **44**, 4539-4543.

7. Z. W. Chen, M. Waje, W. Z. Li and Y. S. Yan, *Angew. Chem. Int. Ed.*, 2007, **46**, 4060-4063.
8. S. J. Guo, S. Zhang, X. L. Sun and S. H. Sun, *J. Am. Chem. Soc.*, 2011, **133**, 15354-15357.
9. C. Koenigsmann, W. P. Zhou, R. R. Adzic, E. Sutter and S. S. Wong, *Nano Lett.*, 2010, **10**, 2806-2811.
10. H. W. Liang, X. A. Cao, F. Zhou, C. H. Cui, W. J. Zhang and S. H. Yu, *Adv. Mater.*, 2011, **23**, 1467-1471.
11. H. Yan, H. S. Choe, S. W. Nam, Y. J. Hu, S. Das, J. F. Klemic, J. C. Ellenbogen and C. M. Lieber, *Nature*, 2011, **470**, 240-244.
12. V. K. LaMer and R. H. Dinegar, *J. Am. Chem. Soc.*, 1950, **72**, 4847-4854.
13. W. Ostwald, *Lehrbuch der Allgemeinen Chemie*, W. Engelmann Leipzig, Germany, 1896.
14. J. D. H. Donnay and D. Harkei, *Am. Mineral.*, 1937, **22**, 446-466.
15. M. G. Friedel, *Bull. Soc. Fr. Mineral. Cristallogr.*, 1907, **30**, 326-455.
16. A. Bravais, *Études Cristallographic*, Gauthier-Villars, Paris 1866.
17. R. Docherty, G. Clydesdale, K. J. Roberts and P. Bennema, *J. Phys. D Appl. Phys.*, 1991, **24**, 89-99.
18. G. Z. Wulff, *Kristallogr.*, 1901, **34**, 449-530.
19. L. D. Marks, *Rep. Prog. Phys.*, 1994, **57**, 603-649.
20. H. Colfen and S. Mann, *Angew. Chem. Int. Ed.*, 2003, **42**, 2350-2365.
21. R. L. Penn and J. F. Banfield, *Science*, 1998, **281**, 969-971.
22. J. F. Banfield, S. A. Welch, H. Z. Zhang, T. T. Ebert and R. L. Penn, *Science*, 2000, **289**, 751-754.
23. J. Zhang, F. Huang and Z. Lin, *Nanoscale*, 2010, **2**, 18-34.
24. J. Polleux, N. Pinna, M. Antonietti and M. Niederberger, *Adv. Mater.*, 2004, **16**, 436-439.
25. A. Halder and N. Ravishankar, *Adv. Mater.*, 2007, **19**, 1854-1858.
26. M. Yeadon, M. Ghaly, J. C. Yang, R. S. Averback and J. M. Gibson, *Appl. Phys. Lett.*, 1998, **73**, 3208-3210.
27. F. Huang, H. Z. Zhang and J. F. Banfield, *Nano Lett.*, 2003, **3**, 373-378.

28. X. Chen, M. Qiao, S. Xie, K. Fan, W. Zhou and H. He, *J. Am. Chem. Soc.*, 2007, **129**, 13305-13312.
29. W. Z. Zhou, *Adv. Mater.*, 2010, **22**, 3086-3092.
30. H. F. Greer, F. J. Yu and W. Z. Zhou, *Sci. China Chem.*, 2011, **54**, 1867-1876.
31. X. F. Yang, J. X. Fu, C. J. Jin, J. A. Chen, C. L. Liang, M. M. Wu and W. Z. Zhou, *J. Am. Chem. Soc.*, 2010, **132**, 14279-14287.
32. J. R. G. Sander, D. K. Bucar, J. Baltrusaitis and L. R. MacGillivray, *J. Am. Chem. Soc.*, 2012, **134**, 6900-6903.
33. H. Greer, P. S. Wheatley, S. E. Ashbrook, R. E. Morris and W. Z. Zhou, *J. Am. Chem. Soc.*, 2009, **131**, 17986-17992.
34. R. Ferrando, J. Jellinek and R. L. Johnston, *Chem. Rev.*, 2008, **108**, 845-910.
35. L. Zhang, F. Hou and Y. W. Tan, *Chem. Commun.*, 2012, **48**, 7152-7154.
36. X. P. Wang, N. Kariuki, J. T. Vaughey, J. Goodpaster, R. Kumar and D. J. Myers, *J. Electrochem. Soc.*, 2008, **155**, B602-B609.
37. M. Yamauchi, R. Abe, T. Tsukuda, K. Kato and M. Takata, *J. Am. Chem. Soc.*, 2011, **133**, 1150-1152.
38. P. Reyes, A. Figueroa, G. Pecchi and J. L. G. Fierro, *Catal. Today*, 2000, **62**, 209-217.
39. N. Toshima and Y. Wang, *Adv. Mater.*, 1994, **6**, 245-247.
40. T. Komatsu and A. Tamura, *J. Catal.*, 2008, **258**, 306-314.
41. D. Xu, Z. P. Liu, H. Z. Yang, Q. S. Liu, J. Zhang, J. Y. Fang, S. Z. Zou and K. Sun, *Angew. Chem. Int. Ed.*, 2009, **48**, 4217-4221.
42. B. Gilbert, F. Huang, H. Z. Zhang, G. A. Waychunas and J. F. Banfield, *Science*, 2004, **305**, 651-654.
43. G. Ouyang, G. Yang, C. Sun and W. Zhu, *Small*, 2008, **4**, 1359-1362.
44. J. B. Wu, P. P. Li, Y. T. Pan, S. Warren, X. Yin and H. Yang, *Chem. Soc. Rev.*, 2012, **41**, 8066-8074.
45. M. Gsell, P. Jakob and D. Menzel, *Science*, 1998, **280**, 717-720.
46. H. Yoshida, Y. Kuwauchi, J. R. Jinschek, K. J. Sun, S. Tanaka, M. Kohyama, S. Shimada, M. Haruta and S. Takeda, *Science*, 2012, **335**, 317-319.
47. C. Solliard and M. Flueli, *Surf. Sci.*, 1985, **156**, 487-494.
48. B. Medasani and I. Vasiliev, *Surf. Sci.*, 2009, **603**, 2042-2046.

49. M. J. Walsh, K. Yoshida, A. Kuwabara, M. L. Pay, P. L. Gai and E. D. Boyes, *Nano Lett.*, 2012, **12**, 2027-2031.
50. M. Raney, *U.S Pat.*, 1628190, 1927.
51. D. S. Wang, P. Zhao and Y. D. Li, *Sci. Rep.*, 2011, **1**.
52. P. Strasser, S. Koh, T. Anniyev, J. Greeley, K. More, C. F. Yu, Z. C. Liu, S. Kaya, D. Nordlund, H. Ogasawara, M. F. Toney and A. Nilsson, *Nat. Chem.*, 2010, **2**, 454-460.
53. X. M. Lu, H. Y. Tuan, J. Y. Chen, Z. Y. Li, B. A. Korgel and Y. N. Xia, *J. Am. Chem. Soc.*, 2007, **129**, 1733-1742.
54. J. Erlebacher, M. J. Aziz, A. Karma, N. Dimitrov and K. Sieradzki, *Nature*, 2001, **410**, 450-453.
55. H. Yang, *Angew. Chem. Int. Ed.*, 2011, **50**, 2674-2676.
56. J. Y. Chen, B. Wiley, J. McLellan, Y. J. Xiong, Z. Y. Li and Y. N. Xia, *Nano Lett.*, 2005, **5**, 2058-2062.
57. H. Zhang, M. S. Jin, J. G. Wang, M. J. Kim, D. R. Yang and Y. N. Xia, *J. Am. Chem. Soc.*, 2011, **133**, 10422-10425.
58. X. Xia, Y. Wang, A. Ruditskiy and Y. Xia, *Adv. Mater.*, 2013, **25**, 6313-6333.
59. S. E. Skrabalak, J. Y. Chen, Y. G. Sun, X. M. Lu, L. Au, C. M. Cobley and Y. N. Xia, *Acc. Chem. Res.*, 2008, **41**, 1587-1595.
60. Y. Sun, B. T. Mayers and Y. Xia, *Nano Lett.*, 2002, **2**, 481-485.
61. H. G. Liao and H. M. Zheng, *J. Am. Chem. Soc.*, 2013, **135**, 5038-5043.
62. H. Zheng, R. K. Smith, Y.-w. Jun, C. Kisielowski, U. Dahmen and A. P. Alivisatos, *Science*, 2009, **324**, 1309-1312.
63. A. Guchhait, A. K. Rath and A. J. Pal, *Chem. Mater.*, 2009, **21**, 5292-5299.

Chapter 2 Experimental

2.1 Synthetic methods for metallic nanoparticles

Metallic nanomaterials can be synthesized in a variety of methods: in solid state, gaseous phase and in solution. Among these approaches, the solution-based method has advantages to produce uniform and small nanoparticles, by controlling reaction parameters such as temperature, surfactants and reactant concentration. The first colloidal approach was reported by Faraday in 1857,¹ in which what are known as gold particles nowadays were prepared in the presence of phosphorus. This colloidal approach was developed and optimized by Turkevich since 1951.²

Alloyed nanoparticles can be prepared by co-reduction of two or several kinds of metal precursor salts in the solution with reducing agents such as NaBH₄. In particular, the **polyol process** is one of the most widely applied methods to synthesize well-tuned nanoparticles of metals and their alloys. Polyols are compounds with polyhydric groups such as ethylene glycol, glycol ethers and 1,2-hexadecanediol, which have a mild reducing ability and chelating property.³ During the redox reaction, the hydroxyl group is oxidized to carbonyl, while the metal precursors are reduced, followed by nucleation to produce nanoparticles. Generally speaking, the metal species with the higher redox potential is reduced first, forming a core for the second metal to deposit on. The sequence of reduction can be changed by introducing surface ligands that are able to bind strongly to the metal ions with higher redox potential to stabilize it.

Seeded growth method is another common strategy, in which as-prepared seeds are added into a solution containing a different type of metal precursors. The second metal can nucleate and grow on these seeds to produce nanoparticles possessing structures such as core-shell and heterostructure. When the second metal deposits evenly on the seed, a core-shell structure is formed. If the second metal only nucleates and grows on specific facets, this will lead to heterostructure nanoparticles.

In this project, a variety of synthetic methods were applied. In general, metallic nanoparticles were all prepared by a polyol process. Polyols, ethylene glycol and 1,2-decanediol were used as reducing agents. Various surface ligands including hydrophilic and hydrophobic molecules and polymers were applied in the synthesis. Seeded growth method was used in the preparation of AuCuPd nanowires. Dealloying treatment was performed on CuPt nanoparticles by either chemical acid etching or galvanic replacement. Photocatalytic and electrochemical properties of the bimetallic nanoparticles were tested. Detailed synthetic procedures are described in experimental section of each chapter.

2.2 Characterization techniques

Nanoparticles were analyzed by several techniques, including high resolution transmission electron microscopy (HRTEM), scanning electron microscopy (SEM), energy dispersive X-ray spectroscopy (EDX), powder X-ray diffraction (XRD), infrared spectroscopy (IR) and thermogravimetric analysis (TGA). The principles of these techniques are discussed in the following content.

2.2.1 High resolution transmission electron microscopy

HRTEM is the most important and frequently used technique in this project. The basic principles of TEM, as well as the analysis technique of selected area electron diffraction (SAED) are included in this section.

High resolution due to electron beam

Microscopes magnify objects that people can hardly observe with naked eyes. Enhancement of resolution is a major target of a microscope, but resolution is not always

increased as magnification increases. Resolution can be determined as the smallest distance of two points that can be distinguished. The resolution ability of human eyes is around 0.1 mm. If two points are closer than this distance, we see them as a single one.

The maximum of the resolution of a microscope can be expressed as:

$$r = \frac{0.61 \lambda}{n \sin \alpha}$$

Where λ is the wavelength of the light source, and $n \sin \alpha$ is a general term for the microscope numerical aperture.⁴

This equation indicates that the resolution of a microscope is determined by the wavelength of the light source: if the wavelength is shorter, the resolution can be higher. The wavelength of visible light falls in the range of 390–760 nm, resulting in the limitation of optical microscope. To further increase the resolution of a microscope, a light source with a shorter wavelength needs to be applied. Once electrons were discovered to have the wave-particle duality, they were soon used to develop electron microscopes.

Louis-Victor de Broglie proposed in 1924 that the wavelength of electrons can be calculated with equation

$$\lambda = \frac{h}{mv}$$

in which h Planck's constant

m mass of electron

v velocity of electron

The velocity of electrons depends on the accelerated voltage, V in TEM, that is, the potential energy of an electron equals to its kinetic energy.

$$eV = \frac{1}{2} mv^2$$

If accelerated by high voltage, electrons can approach the speed of light, c . Under this circumstance, relativistic corrections should be considered for a final expression of

$$\lambda = \frac{h}{\sqrt{2m_0eV(1 + \frac{eV}{2m_0c^2})}}$$

When the accelerated voltage is 200 kV, which is normally used during the operation of TEM, the wavelength of electron beam is calculated to be 0.00251 nm. This is much smaller than the wavelength of visible light and is able to offer atomic resolution.

Components of TEM

A TEM is composed of an illumination system, a specimen stage, an imaging system and a data recording system. A simplified illustration of TEM is shown in **Figure 2.1**.

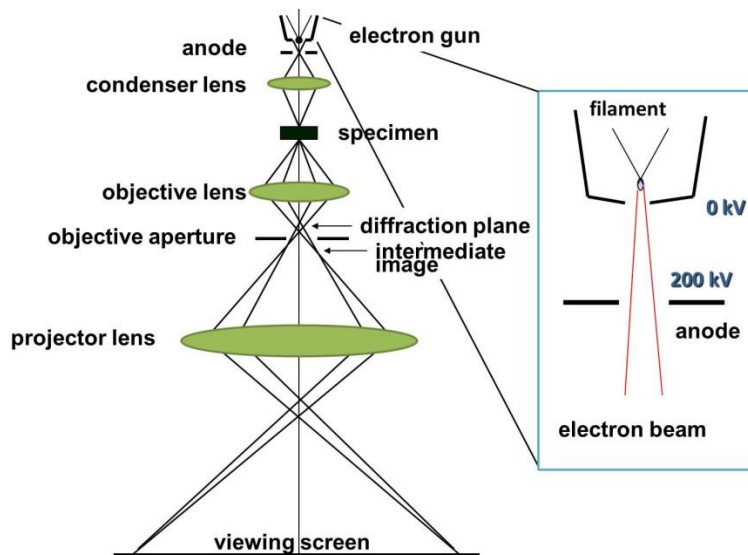


Figure 2.1 Simplified illustration of the main components in a TEM in which the electron beams pass through a series of electromagnetic lenses. The inset is an enlarged image of the electron gun.⁵

Illumination system includes electron gun, condenser lens and some adjustment devices. The electron gun is the core part in the illumination system, which usually uses a tungsten (W)

filament, a lanthanum hexaboride (LaB_6) source or a field emission source. The first two thermionic sources generate free electrons by heating the filament to a high temperature, at which electrons have energies high enough to overcome the work function. On the other hand, the field emission gun is a cold source, because the emitter serves as a cathode, which generates free electrons due to its potential gradient relative to a nearby anode. The electrons will be accelerated towards the anode, which has a high voltage (usually 200 kV), to form a beam. When electrons arrive at the anode they have a high kinetic energy and no potential energy. The condenser lens will focus and converge the accelerated electron beam. A field emission gun gives higher current density and beam coherence, thus producing better image resolution and images with a higher quality.⁶ In this project, our TEM (JEOL-2011) uses a thermionic electron gun.

The specimen stage is where a target specimen is placed. The objective lens actually determines the quality of the TEM images. Intermediate lenses and projection lenses control the magnification, up to as high as 1.5 million. Images are recorded by a charge coupled device (CCD) beneath the viewing screen. TEM requires a high vacuum in order to prolong service life of its filament, reduce the collision between electrons and gas, as well as to reduce sample contamination.

In summary, this is how a TEM works: first, an electron beam is generated in an electron gun by heating a filament in vacuum, and further accelerated towards the anode by applying a high voltage. Then, the beam travels through the condenser lens, forms a coherent beam and transmits through the specimen. The objective lens and the projector lens focus these transmitted electrons, to form a final image on the fluorescent screen.

Image and Contrast

Image formation

When the electron beam passes through a crystal sample, it is diffracted into Bragg beams, with phase and amplitude information that can reflect the structure of specimen. Unfortunately,

a real lens is imperfect and causes phase shifts of diffracted electron waves. A phase shift is introduced by the spherical aberration, and can be offset by the defocus effect of the lens.

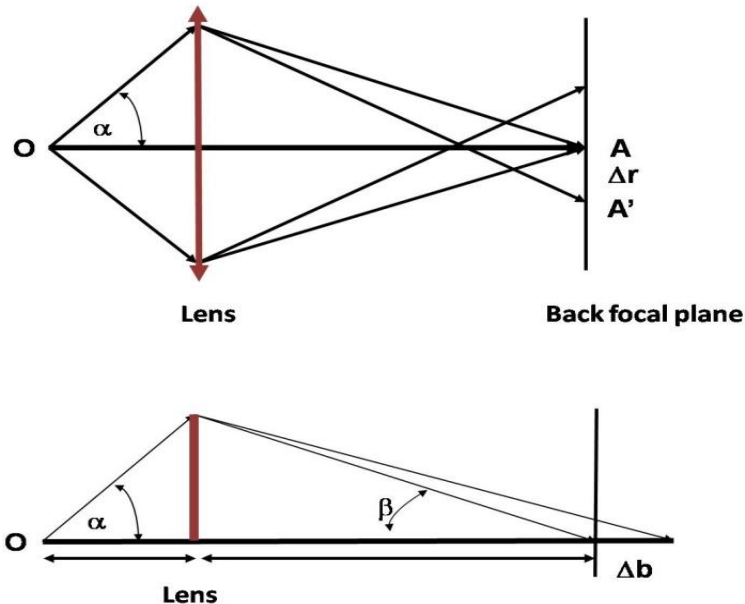


Figure 2.2 Diagrams showing that an imperfect lens can cause distortion of an image (top). A defocus condition of the objective lens can move an image behind the focal plane (bottom). This factor can cancel out the phase shift caused by spherical aberration.

An ideal lens focuses all the incoming waves on the axis of the back focal plane. Spherical aberration, however, leads to rays far away from the lens optical axis (in the outer portion) focusing closer to the lens, as demonstrated in **Figure 2.2**. If the lens is ideally perfect, all rays will intersect at point A. Due to spherical aberration, rays with a scattered angle α reach at the point A' on the plane. The deflected distance, Δr is proportional to the magnification, M . It can be expressed as:

$$\Delta r = MC_s \alpha^3$$

where C_s is the spherical aberration coefficient and α is the scattered angle.⁵ Broadening image is observed on the back focal plane. Variation in focal length generates a path difference, hence a phase shift can be calculated as:

$$W_s(\alpha) = \left(\frac{2\pi}{\lambda}\right) \frac{1}{4} C_s \alpha^4$$

Defocus of the lens also generates phase shift, which can compensate the shift introduced by spherical aberration. As shown at the bottom of **Figure 2.2**, defocus of lens increases the path length and produces a phase shift of:

$$W_f(\alpha) = \left(\frac{2\pi}{\lambda}\right) \frac{1}{2} \Delta F \alpha^2$$

in which ΔF is the lens defocus.⁵ In this way, the total phase shift equals to:

$$\chi(\alpha) = \frac{2\pi}{\lambda} \left(\frac{1}{2} \Delta F \alpha^2 - \frac{1}{4} C_s \alpha^4 \right)$$

In practical TEM operation, images are usually recorded in slightly under-focused state to eliminate spherical aberration as much as possible. In the recent decades, there has been big breakthroughs in aberration corrected TEM. For instance, FEI Titan 80-300 can reach a point resolution of 0.08 nm with Cs-corrector of the objective lens.⁷

Contrast

Three types of contrast dominate in TEM images: mass thickness contrast, diffraction contrast and phase contrast.

The effect of thickness on the contrast is easy to understand: the thicker the specimen, the darker the contrast. But the effect of mass also needs to be considered. Elements with different atomic numbers differ in their ability to scatter electrons. Heavy elements are normally darker in bright field TEM images, because more electrons are scattered. Under high angle dark field mode, the contrast is reversed: heavy atoms look brighter. In either mode, the contrast is based on the differences in scattering ability.

Diffraction contrast is caused by differences in diffraction intensity: the intensity of the transmitted beam is weakened by strong diffraction. Besides, the interference of defects or

strain on the wave intensities of an electron beam emphasizes the distortion, so that it is useful to study defects in crystalline materials. Phase contrast comes from a phase shift of the electron beam when they transmit the specimen. It is sensitive to the atom distribution of the sample.

In a HRTEM image, which corresponds to atoms, the white spots or the black ones? In fact, it depends on the defocus. White and black spots can reverse their contrast when the defocus of the objective lens is changed. Simulated HRTEM images of Au nanoparticles in **Figure 2.3** show the contrast reversal with different defocuses. TEM images are a 2D projection of a 3D specimen. Atom spots represent rows of atoms whose orientations are parallel to the direction of the incident beam.

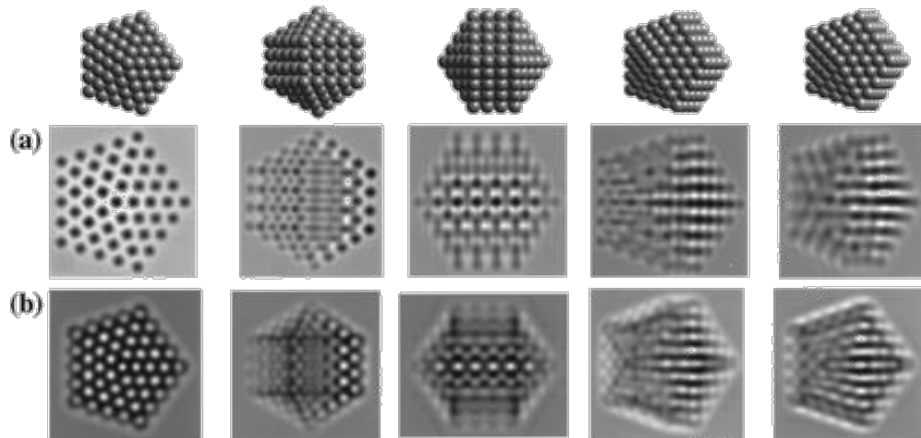


Figure 2.3 Simulated images of decahedral Au nanoparticles recorded at focuses of (a) $\Delta F = 42$ nm and (b) $\Delta F = 70$ nm.⁸

Selected area electron diffraction

Selected area electron diffraction (SAED) can determine the crystallography of a sample. Electron beams are diffracted to certain angles dependent on the crystal structure of the specimen. By choosing apertures, users can examine a selected area of the specimen and only this area contributes to the diffraction pattern. SAED is able to reveal the crystal structure of

a single small particle, which differs from X-ray diffraction. Basically, there are three different types of diffraction patterns corresponding to different crystallinities as shown in **Figure 2.4**.

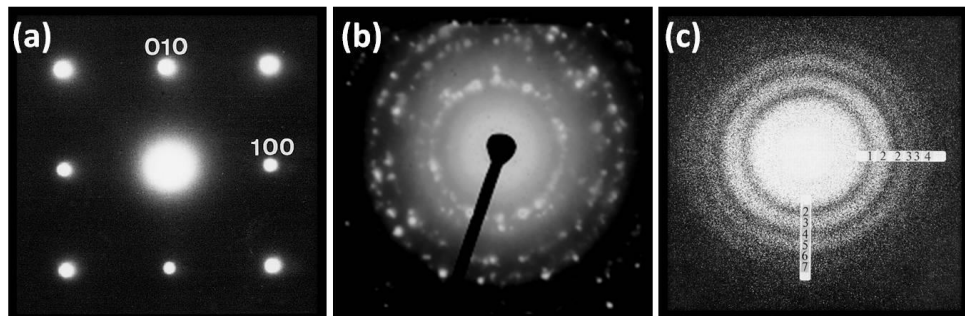


Figure 2.4 SAED patterns showing (a) a regular two-dimensional arrangement of spots typical of a single crystal; (b) dotted rings recorded from a polycrystalline particle and (c) solid rings from an amorphous particle.⁵

Single crystals produce a 2D pattern of regular spots like **Figure 2.4a**, while polycrystalline particles produce dotted rings due to the different crystal orientations. One ring represents all sets of reflection planes giving similar *d*-spacings. Amorphous particles give no diffraction spots, only solid rings. In order to get the best diffraction pattern, the specimen usually needs be tilted in both the x and y direction, which requires a double tilt specimen holder. An SAED pattern is a reciprocal projection of a lattice, which means low index planes correspond to diffraction spots nearer to the center.

HRTEM and SAED normally suffer from a problem called multiple scattering, which alters intensities of beams related to the specimen thickness. However, for nanomaterials, this effect can be ignored.

In this project, TEM characterization was carried out on a JEOL JEM-2011 microscope fitted with a LaB₆ filament. TEM image were recorded using a Gatan 794 CCD camera.

2.2.2 Scanning electron microscopy

Scanning electron microscopy (SEM) forms images by scanning a focused electron beam across a specimen. **Figure 2.5** shows a diagram of an SEM. An electron beam is focused onto the sample after passing through the first and second condenser lenses and then through pairs of scanning coils which deflect the beam in the x and y axis. After the electron beam interacts with the sample, various signals such as secondary electrons, backscattered electrons and X-rays, are generated and collected by detectors. Different from TEM, SEM has no lens behind specimen stage. SEM increases the magnification by scanning smaller areas of the specimen.

The most common mode for SEM image is to collect secondary electrons that have low energy (< 50 eV⁹). Because secondary electrons are emitted usually from 0–10 nm beneath the surface,⁹ and their production is sensitive to the surface morphology. Therefore, they are mainly used for morphology imaging. The direction of incident beam is fixed in an SEM, but the uneven surface of the specimen leads to various incident angles and different brightness in final image.

Another imaging mode is to collect backscattered electrons, which are sensitive to atomic numbers. Backscattered electrons have higher energy, because they are formed by the Rutherford backscattering which is an elastic interaction between incident electrons and sample atoms. Consequently, areas containing heavy elements give brighter contrast than those with light elements. This is an effective method for qualitative characterization of elemental distribution of domains.

If the specimen is conductive, it needs no special preparation for SEM. Poorly conductive specimens, however, have to be coated with a very thin layer of gold or carbon before characterization. Otherwise charge accumulation will affect the imaging. This is because a non-conductive sample will become either positively or negatively charged after interaction with the incident electron beam. This creates an electric field which deflects the beam and causes image distortion. Since a thick coating layer may mask the real surface of the sample, another method of avoiding charging effect is to work at a lower working voltage, usually

smaller than 1.5 kV, to keep the original surface. But image resolution will decrease in such a condition.

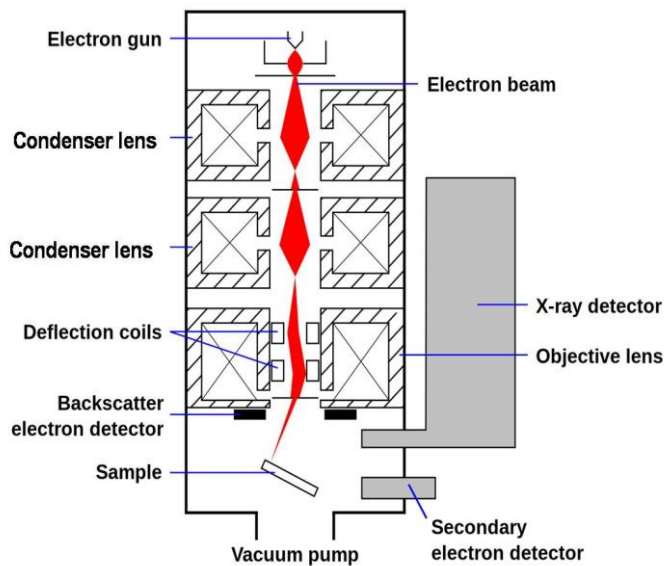


Figure 2.5 Schematic diagram showing the main components within an SEM.

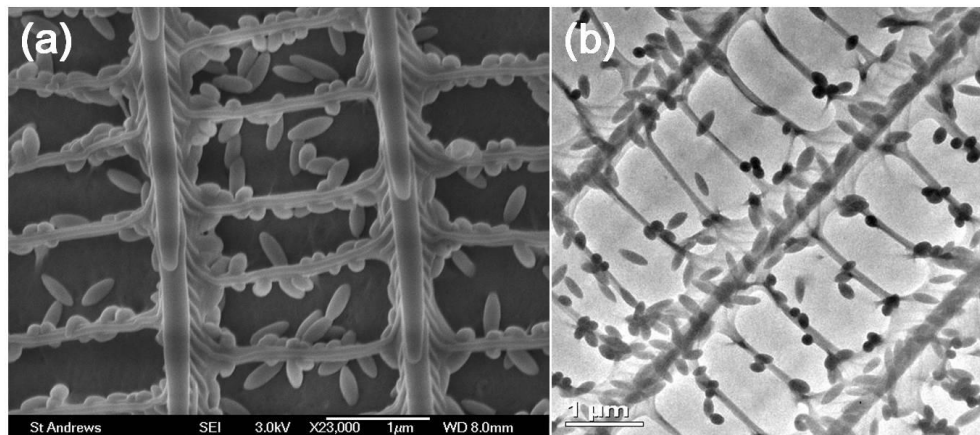


Figure 2.6 (a) SEM and (b) TEM images of a butterfly wing scale. The two images were taken under a similar magnification. These images are from my own work.

One important advantage of SEM is its larger depth of field. 3D structure can be well resolved in SEM. For example, **Figure 2.6** shows SEM and TEM images of a butterfly wing scale taken under a similar magnification, which is a topic I investigated in my Phd but not included in this thesis. It is obvious that the SEM image better reveals the 3D periodic structure

of the wing scale. In contrast, the TEM image is a 2D projection and loses space information. In particular, details of the “ridges” are observed clearly in the SEM image, but the TEM image flattens them and gives an overlapped view of morphology.

Samples in this project were examined by a field-emission scanning electron microscopy (FE-SEM) on a JEOL JSM-6700F microscope operating at 2-5 kV.

2.2.3 Energy dispersive X-ray spectroscopy

Energy dispersive X-ray spectroscopy (EDX) is a common technique used to analyze the chemical composition and elemental distribution in a specimen. EDX works by analysis of the X-ray produced by the specimen after collision with the incident electron beam, and is widely equipped in TEMs and SEMs.

An atom has different shells, which are termed with “K”, “L”, “M” and “N” *etc.* If the incident electron beam knocks out one electron in the K shell, this creates a vacancy. An electron in a higher-energy shell will drop down to fill this vacancy (see illustration in **Figure 2.7**). At the same time, radiation will be emitted in the form of an X-ray, based on the energy conservation laws. The wavelength of the released X-ray corresponds to the energy difference between two levels, taking the L shell as an example:

$$h\nu = E_{\text{L shell}} - E_{\text{K shell}}$$

This radiation from L to K shell is K_α . The newly created vacancy in the L shell can be occupied by an electron from the M shell, giving out an L_α X-ray. The intensity of K_α is stronger than K_β , due to the higher probability of electrons dropping from an L shell to a K shell.

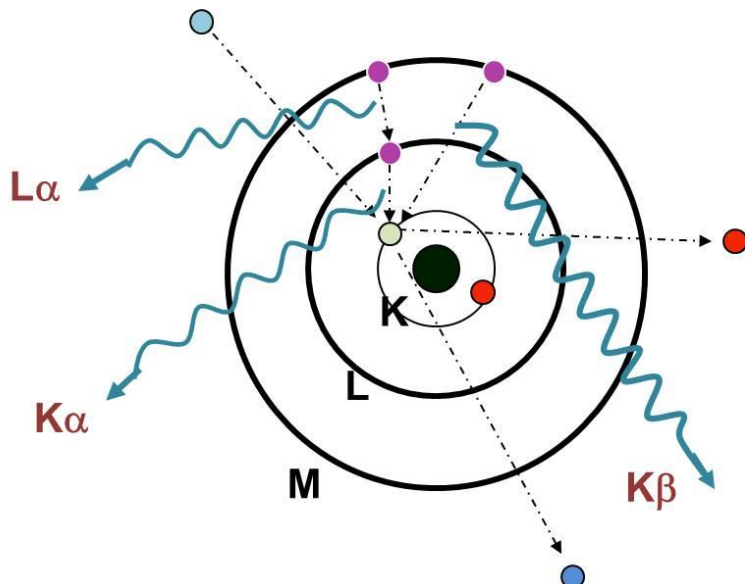


Figure 2.7 Diagram demonstrating that an electron in K-shell is ejected and the vacancy is filled with an electron dropping from the M-shell. An X-ray is emitted in compensation for this energy difference.

As a result, a series of discrete X-rays are generated, which are characteristic to each element due to their unique atomic structure. When the X-ray photon hits the detector, it is converted into digital signal which is measured by the number of counts. These counts produce the overall EDX spectrum for the sample. By studying the position and intensity of the spectrum, the element composition can be determined both quantitatively and qualitatively.

In EDX analysis, we should notice that the intensity of an X-ray generated from a specimen decreases during travelling towards the detector. In the process before an X-ray reaches the detector, many factors affect the X-ray intensity: electron scattering in the solid sample, excitation and absorption of X-rays, and fluorescence excitation and absorption, *etc.* As a result, the production of X-rays in a sample does not simply correspond to a function of composition. For example, the incident electron beam does not only interact with the surface atoms in a sample, but can penetrate to a depth of 1–2 μm into the sample. Therefore, an X-ray generated inside the sample needs to pass through matter. In such a process X-rays will be absorbed. The absorption, in fact, strongly depends on the identity of the absorber. Generally speaking, low energy X-rays have large mass absorption coefficients (are more easily absorbed), according to calculations from Heinrich's parameterization.⁹ Consider both Al and

Ni generating K_{α} X-rays (Al 1.49 keV, Ni 7.47 keV) at 1 μm beneath the surface, it can be calculated Al X-ray only has 8 % probability of reaching the surface while Ni has a 94 % probability. A large difference exists in absorption between various elements.

ZAF corrections (Z: atomic number, A: absorption, F: fluorescence excitation and absorption) have been developed to permit corrections of EDX analysis for a more precise composition. After all, EDX results rely on so many variables, making high-quality quantitative analysis difficult. In this project, most elements examined are heavy metals, such as Cu, Pt and Pd, which can give more reliable EDX results than light elements. EDX results from at least ten different spots in each sample have been measured and averaged in the analysis, to maximize the accuracy of quantitative examination.

EDX used in this project was carried out using an Oxford Instruments X-ray Analysis ISIS 300 system on the TEM and Oxford INCA system on SEM.

2.2.4 X-ray diffraction

X-ray diffraction (XRD) is a widely used technique for phase identification and structural analysis. When X-rays strike a crystal sample, secondary spherical waves are produced after the interactions between X-rays and electrons without any loss in energy. This scattering process is elastic scattering, where the frequency of secondary waves is the same as the original waves. Ordered arrangement of atoms can generate interference peaks that have the same symmetry as the crystal.

Incident X-ray can produce a peak when the path difference is a multiple of the wavelength λ , so that the interference is constructive. This is expressed by the Bragg's law:

$$2d \sin \theta = n \lambda$$

For lattice planes with spacing of d , the lower beam travels an extra distance of $2d \sin \theta$, where θ is the incident angle (see illustration in **Figure 2.8**). Here n is an integer, and represents the order of diffraction peak.

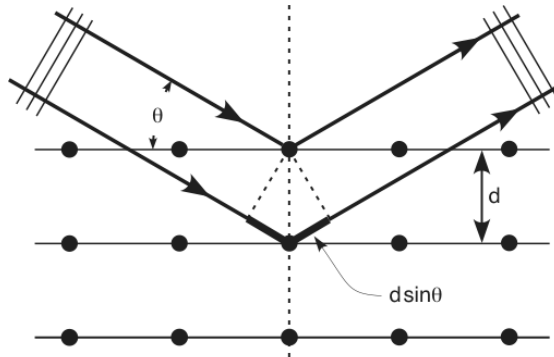


Figure 2.8 Schematic diagram of Bragg's diffraction.

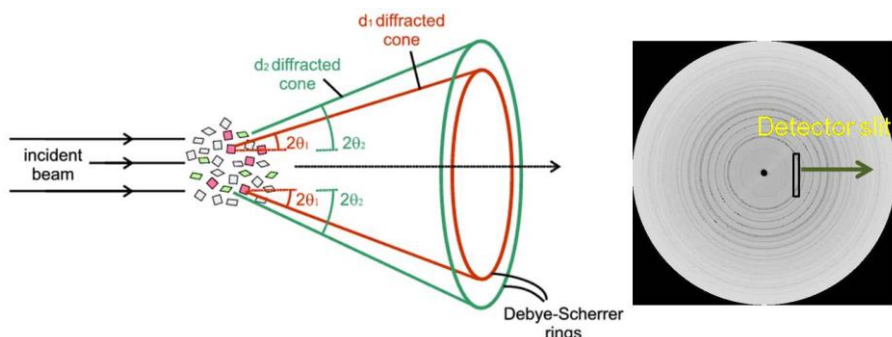


Figure 2.9 Schematic diagram of powder XRD and data collection.

According to Bragg's equation, these spherical waves add constructively in certain directions. Therefore, part of the incident beam is reflected by an angle of 2θ . With the fixed λ , different planes in the crystal reflect the beam at different angles. In powder diffraction, crystals have a variety of orientations, resulting in diffraction rings: the Derby-Scherrer rings. In order to obtain a diffraction pattern, the detector in most designs rotates to various 2θ angles to measure diffraction intensities from the sample (see **Figure 2.9**).

A crystal has atoms arranged in a periodic manner. The atomic positions in one unit cell can affect the phase difference and intensity of the X-ray scattering. The sum of scattered waves from one unit cell for $(h k l)$ reflection can be calculated with the following equation, also known as structure factor¹⁰:

$$F_{hkl} = \sum f_i \exp[2\pi i(hx_i + ky_i + lz_i)]$$

where f is the atomic scattering factor, (x, y, z) are the fractional coordinates.

Amplitude of the scattered wave is defined by the absolute value of F , so that the intensity of the resultant wave is proportional to $|F_{hkl}|^2$.

$$|F(hkl)|^2 = \left[\sum_n f_n \cos 2\pi(hx_n + ky_n + lz_n) \right]^2 + \left[\sum_n f_n \sin 2\pi(hx_n + ky_n + lz_n) \right]^2$$

In this project, most metallic alloys investigated are face-centered-cubic (fcc) structure, in which one unit cell contains 4 kinds of atomic positions

$$(000), (\frac{1}{2} \frac{1}{2} 0), (\frac{1}{2} 0 \frac{1}{2}), (0 \frac{1}{2} \frac{1}{2})$$

The structure factor is given as:

$$\begin{aligned} F_{hkl} &= f \left(1 + e^{i\pi(h+k)} + e^{i\pi(h+l)} + e^{i\pi(k+l)} \right) \\ &= f \left[1 + (-1)^{h+k} + (-1)^{h+l} + (-1)^{k+l} \right] \end{aligned}$$

Only when $h k l$ are all even or odd, the result is $4f$, otherwise is 0. In the final XRD pattern, reflection peaks such as (100) and (110) cannot be observed, due to this systematical absence phenomenon.

XRD is a powerful tool to identify the crystallinity and crystal phase of materials. By comparing XRD patterns with a reference Powder Diffraction File (PDF) from JCPDS database, we are able to index peaks in the patterns. A XRD pattern also provides information of crystal sizes according to the Scherrer equation:

$$\tau = \frac{K\lambda}{\beta \cos \theta}$$

The average size of crystalline domain τ is determined by: X-ray wavelength λ , which is usually copper K_{α} 0.154 nm; β , the full width at half maximum (FWHM) intensity of the peak ; the shape factor K, which is typically 0.9 but varies with the specific shape of particles; and diffraction angle θ of the peak.

XRD was performed on a PANalytical Empyrean diffractometer with Cu K_{α} radiation in this project.

2.2.5 Infrared spectroscopy

Infrared (IR) spectroscopy is a very common technique used for the identification of compounds and analysis of their structure. It measures the various IR frequencies absorbed by the sample. Different functional groups in the sample have characteristic absorption of IR frequencies; therefore can be determined by the IR spectroscopy.

IR region is divided into three parts: near IR, mid IR and far IR. Mid IR is the most commonly used region, which is suitable to analyze the vibration frequencies.

	Near IR	Mid IR	Far IR
wavelength/ μm	0.78–2.5	2.5–50	50–1000
wavenumber/ cm^{-1}	13000–4000	4000–200	200–10

Atoms in a molecule are in vibration. When the frequency of one vibration equals to that of the incident IR radiation, absorption will occur. The molecule will jump to a higher energy state, which has the same vibrational frequency but larger amplitude. The excited molecule can only remain in this higher vibrational state for a short time, then returns to the ground state by releasing the extra energy in the form of heat to the surrounding environment. Although

the vibrational energy levels are quantized, the excitation is usually accompanied with rotational motions, which leads to absorption bands rather than discrete lines in the final IR spectrum.

Two major vibration types are stretching and bending, which can be further specialized into detailed categories such as symmetric/asymmetric stretching, scissoring and rocking. Bands observed in the IR spectrum are fewer than the fundamental vibrations. One major reason is that only vibration modes that can change the dipole moment of the molecule can absorb IR radiation. Generally speaking, the more polar the bond is, the more it can absorb IR radiation. For example, the absorption ability of carbonyl group is much stronger than alkyne group. Some vibrations are infrared inactive, because of no change in the dipole moment. For instance, CO₂ symmetric stretching results in no absorption because two C=O bonds stretch in an opposite, linear direction.

In this project, metallic nanoparticles are prepared with surface ligands, which play crucial roles during the growth process for shape control. IR spectroscopy tests have been carried out to confirm the existence of these surface ligands on the as-prepared nanoparticles. IR is performed on a Thermo Fisher NICOLET 6700 FT-IR spectrometer, which is attenuated total reflection infrared (ATR-IR) spectroscopy. In ATR-IR, examination of samples can be carried out directly without any preparation.

When the refractive index of the crystal is larger than that of the sample, total reflection can take place when the angle of incidence is greater than the critical angle. The basic principle of ATR is that the IR beam reflects internally in the crystal and the sample (**Figure 2.10**). Therefore, the absorption of the sample is enhanced after multiple interactions with IR radiation.

Total reflection requires the crystal to have a large refractive index. Commonly used ATR crystals include ZnSe, diamond, and Ge and thallium bromide/thallium iodide. ZnSe and diamond have a similar refractive index of 2.4. ZnSe is the most common ATR crystal but needs to be applied in a pH range of 5-9.¹¹ Diamond has no limitation of pH conditions but is

rather costly. Ge has a high refractive index of 4.0 but is very brittle, and thallium bromide/thallium iodide is toxic. In Thermo Fisher NICOLET 6700 FT-IR spectrometer, which is used in the present work, diamond is the ATR crystal.

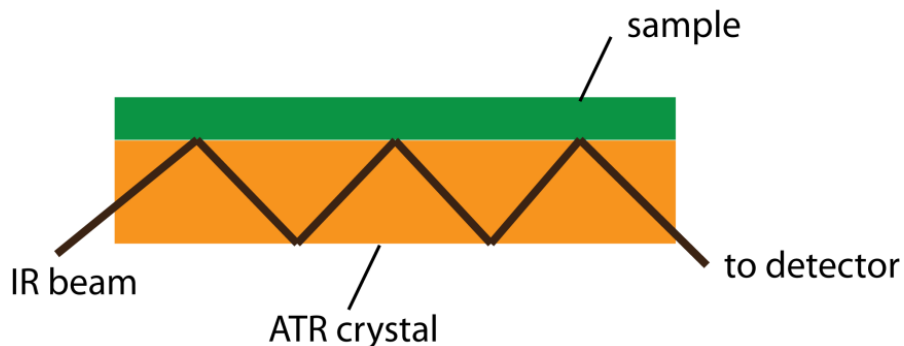


Figure 2.10 Schematic diagram showing multiple reflections in an ATR system.

Compared with conventional transmission FTIR, ATR-FTIR has several advantages: preparation of sample is simple and non-destructive. It is a surface technique and obtains spectrum information from the sample surface, thus particularly suitable for surface characterization. It can also acquire information from different depths of the sample by adjusting parameters.

2.2.6 Thermogravimetric analysis

Thermogravimetric analysis (TGA) is a thermal method in which the mass of the sample is measured as a function of temperature or time. The basic principle of TGA is that the specimen loses weight when heated to high temperature owing to evaporation or decomposition. TGA depends on the precision of mass loss, temperature and temperature change. A programmable furnace is used as well as a thermocouple in order to accurately monitor the temperature.

A typical TGA curve is illustrated in **Figure 2.11**. A sample is usually heated up at a constant rate. When the temperature reaches T_1 , the sample starts to lose weight. The weight loss process can last over a fairly wide temperature range, before the plateau comes out from T_2 . The weight loss ($m_1 - m_2$) is associated with the chemical or physical properties of the sample, for example decomposition content, reduction or combustion. The mass change can be used for calculation to obtain quantitative result.

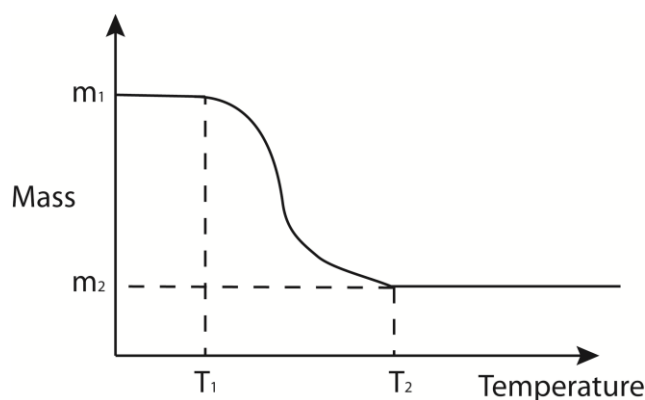


Figure 2.11 Schematic diagram of a TGA curve.

TGA can be used to (1) study the thermal stability of a sample, (2) investigate the reaction kinetics and degradation mechanism, and (3) determine organic or inorganic components in a sample. In this project, TGA is carried out on CuPt nanorods capped with surface ligands, to determine the content of organic ligands. The test was carried out on NETZSCH TG 209 instrument at a heating rate of 5 °C/min in air.

References

1. M. Faraday, *Phil. Trans. R. Soc. Lond.*, 1857, **147**, 145-181.
2. J. Turkevich, P. C. Stevenson and J. Hillier, *Discuss. Faraday Soc.*, 1951, **11**, 55-75.
3. F. Fi évet and R. Brayner, in *Nanomaterials: A Danger or a Promise?*, Springer London, 2013.

4. O. Scherzer, *J. Appl. Phys.* 1949, **20**, 20-29.
5. W. Z. Zhou, in *Introduction to electron microscopy*, Lecture CH5515, University of St Andrews.
6. Z. L. Wang, Y. Liu and Z. Zhang, *Handbook of Nanophase and Nanostructured Materials*, Springer, New York, 2003.
7. M. Haider, P. Hartel, H. Muller, S. Uhlemann and J. Zach, *Microsc. Microanal.*, 2010, **16**, 393-408.
8. Z. L. Wang, *J. Phys. Chem. B*, 2000, **104**, 1153-1175.
9. H. Seiler, *J. Appl. Phys.*, 1983, **54**, R1-R18.
10. D. C. Bell and A. J. Garratt-Reed, *Energy-Dispersive X-Ray Analysis in the Electron Microscope*, BIOS Scientific, London, 2003.
11. Y. Waseda, E. Matsubara and K. Shinoda, *X-ray diffraction crystallography: Introduction, examples and solved problems.*, Springer, Berlin, 2011.
12. B. C. Smith, *Fundamentals of Fourier Transform Infrared Spectroscopy*, CRC press, 2011.

Chapter 3 Ligand Mediated Synthesis of Cu, Pt, Pd Alloyed Nanoparticles

In this chapter, study of the growth process of CuPt bimetallic nanorods reveals a novel ligand mediated mechanism, in which the 1D growth of the nanorods is strongly influenced by the surface ligand monolayer, rather than by the crystal orientation. Photocatalysis testing carried out on CuPt nanorods shows better activity than that of pure Pt rods. In the same synthetic system, trimetallic CuPdPt nanospheres with very uniform shape were prepared, and PdPt and CuPd nanoparticles were also investigated. With the understanding that surface ligands play important roles in morphology control, the solvent effect was studied by varying the solvent to change interactions between surface and ligands.

3.1 Ligand mediated growth of CuPt nanorods

3.1.1 Introduction

One dimensional nanomaterials, such as nanowires and nanorods, demonstrate fascinating properties,¹ and have been widely exploited in memory and logic circuits,² sensing³ etc. A range of approaches have been established to prepare 1D nanomaterials. Template method is a very common approach, in which the 1D nanomaterial is shaped in the template, which serves as a scaffold. A variety of materials can be used, including porous materials with channels,⁴ stepped solid substrates,⁵ or micelles self-assembled from surfactant molecules.⁶

Self-assembly of nanoparticles by means of oriented attachment (OA)^{7, 8} is also widely reported. Primary particles can attach together driven by sharing the same crystallographic orientation. The vital question about the assembly method to produce 1D structures is why the material grows one dimensionally. Currently, there are two principal mechanisms to explain this. One is that surfactants can selectively bind to some particular facets, in order that fusion

takes place between facets with fewer surfactants on them (**Figure 3.1a**).^{9, 10} However, this mechanism cannot explain the formation of CuPt rods. Taking the <111> direction as an example, there are four equivalent <111> directions with an angle of 70.52 ° in fcc-structured CuPt alloy. If fusion occurs in these planes, we should expect a branched structure instead of 1D nanorods. The other mechanisms believe that dipole interactions are the driving force to form 1D nanostructures of semiconductors (**Figure 3.1b**).¹¹⁻¹³ This mechanism cannot explain the 1D growth of metallic nanowires. Therefore, CuPt nanorods are investigated to find out the driving force for 1D growth in the following work. It turns out that surface ligands are an important factor to control 1D growth and the final morphology.

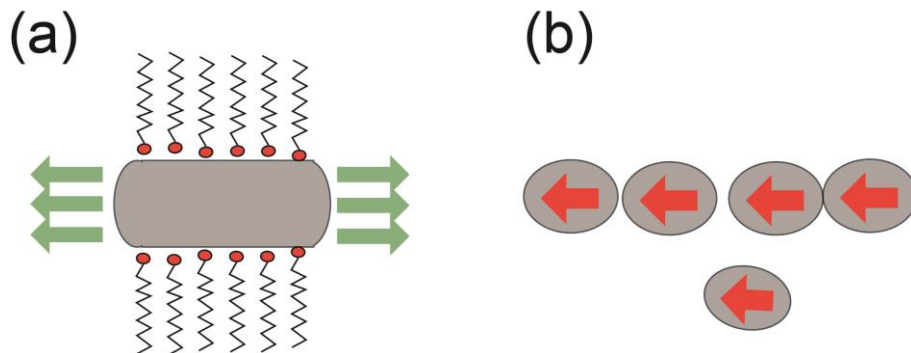


Figure 3.1 Illustrations of two mechanisms to form 1D nanomaterials, driven by (a) surfactants selectively capped on specific planes and (b) dipole-dipole interaction.

3.1.2 Experimental section

Synthesis of CuPt nanorods

CuPt nanorods were prepared by a modified synthetic method previously reported by Liu *et al.*¹⁴ in the ambient atmosphere. A mixture of 40 mg of platinum acetylacetone [Pt(acac)₂], 26 mg of copper acetylacetone [Cu(acac)₂], 70 mg of 1,2-decanediol as reducing agent, 460 mg of hexadecanoic acid, 450 mg of hexadecylamine and 5.0 mL of diphenyl ether as solvent were added to a round-bottom flask. The mixture was heated to 120 °C to completely dissolve

all solids, producing transparent blue solution. The solution was then heated to 225 °C and maintained for 30 min. A series of color changes from blue to green, to yellow and finally black was observed during the heating process. The flask was cooled down to room temperature and a black powder product was collected by centrifugation. The as-prepared specimens often contained both nanospheres and nanorods. The majority of nanospheres can be removed by adding cyclohexane and ethanol, followed by centrifugation. The supernatant contains only nanospheres and the precipitate contains mainly nanorods. The precipitate can be well dispersed in cyclohexane. The solid specimens were washed with ethanol to remove the remaining organic molecules.

The nominal amounts of hexadecanoic acid, hexadecylamine and 1,2-decanediol were varied to systematically examine their effects on the morphology of nanorods. A two-step method was also used to produce strands of ultrathin CuPt wires. The first step was the same as described above, except no hexadecylamine was added. The solution was cooled down to room temperature after a 30 min reaction. In the second step, amine was added to the solution and the procedure was repeated. The details of experimental conditions for the preparation of CuPt nanorods are summarized in **Table 3.1**. The mixed ligands (hexadecanoic acid and hexadecylamine) were also replaced by (octanoic acid, octylamine), (dodecylamine, dodecanoic acid) and (stearic acid, octadecylamine) with the same molar amount to study how the chain length of the surface ligands affect the growth of nanorods.

Pt nanorods for catalysis testing were prepared with the same method only in the absence of Cu(acac)₂ precursor. Graphitic carbon nitride (g- C₃N₄) was synthesized by melamine condensation.¹⁵ Melamine was calcined in an alumina crucible covered with aluminum foil at 600 °C for 2 h. The resulting yellow powder was inspected by XRD and confirmed to be pure g- C₃N₄ phase. Loading of cocatalysts (Pt or CuPt nanorods) onto g- C₃N₄ was simply performed by dispersing g- C₃N₄ and Pt or CuPt in cyclohexane solution. The dispersion solution was then dried at 100 °C and subsequent calcination at 180 °C for 2 h.

Table 3.1 Experiment conditions in the synthesis of CuPt nanorods. T: reaction time; Amine: hexadecylamine; Acid: hexadecanoic acid and L: dimension of nanoparticles, length of nanorods or diameter of nanospheres. Except for the systems marked by C8: octylamine and octanoic acid; C12: dodecylamine and dodecanoic acid; C18: octadecylamine and stearic acid.

Sample amine: acid	T/ h	Amine/ mmol	Acid/ mmol	Molar ratio metal: amine: acid	L/ nm
1: 1	0.5	1.8	1.8	1: 9: 9	15.7 (rods) 2.8 (spheres)
1: 1.5	0.5	1.8	2.7	1: 9: 13.5	11.7 (rods)
1.5: 1	0.5	2.7	1.8	1: 13.5: 9	24.3 (rods)
1.5: 1.5	0.5	2.7	2.7	1: 13.5: 13.5	24.0 (rods)
0.5: 0.5	0.5	0.9	0.9	1: 4.5: 4.5	2.0 (spheres)
2: 1	0.5	3.6	1.8	1: 18: 9	28.9 (rods)
1: 1 (2-step)	0.5	1.8	1.8	1: 9: 9	strands of nanowires
1.5: 1 (2-step)	2	2.7	1.8	1: 13.5: 9	strands of nanowires
1.5: 1.5 (2 step)	0.5	2.7	2.7	1: 13.5: 13.5	nanorods
2: 1 at 160 °C (2-step)	2	3.6	1.8	1: 18: 9	nanospheres
double decanediol	0.5	1.8	1.8	1: 9: 9	15.6 (rods)
1: 1 C8	0.5	1.8	1.8	1: 9: 9	9.5 (rods)
1: 1 C12	0.5	1.8	1.8	1: 9: 9	11.4 (rods)
1: 1 C18	0.5	1.8	1.8	1: 9: 9	15.2 (rods)

Characterization

TEM and HRTEM characterizations were carried out on a JEOL-2011 electron microscope operated at 200 kV. Samples were diluted in hexane and drop-cast onto a holey carbon-coated copper grid followed by solvent evaporation in air at room temperature. Metallic ratios in the samples were examined by EDX using an Oxford INCA system fitted in a JEOL JSM-6700F field emission scanning microscope operating at 15 kV. Powder XRD was performed on a PANalytical Empyrean diffractometer with Cu K α radiation. Attenuated Total Reflection FTIR (ATR-FTIR) was performed on Thermo Fisher NICOLET 6700 FT-IR spectrometer. TGA was carried out on NETZSCH TG 209 instrument at a heating rate of 5 °C/min in air.

Photocatalytic hydrogen evolution

The section of photocatalytic testing was carried out by Dr. Xiaoxiang Xu in University of St Andrews. Measurement of the photocatalytic hydrogen production was carried out in a home-made Teflon reactor.¹⁶ In a typical experiment, 0.2 g catalyst was dispersed in 200 mL oxalic acid solution (0.025M) and was sealed within the Teflon reactor. The reactor was then purged with pure Ar gas as a protective atmosphere. A 250 W iron doped metal halide UV-Vis lamp (Borosilicate Coated Glass HM07, UQG (optic) Ltd., Cambridge UK) filtered with UV cut-off filter $\lambda \geq 420$ nm was used as the light source. The photon flux of the lamp generated is calibrated using a quantum meter (Apogee MQ-200), which is $1305 \pm 27 \mu\text{mol}\cdot\text{m}^{-2} \text{ s}^{-1}$. The gas composition within the reactor was monitored by an on-line gas chromatograph (Aglient 3000 Micro Gas Chromatograph). The measurements were generally carried out for 20 h and the average results were calculated and used in the manuscript.

3.1.3 CuPt nanorods and growth process

CuPt nanorods with a length of 15.7 ± 2.5 nm and width of 2.1 ± 0.2 nm were prepared after a reaction for 0.5 h, as displayed in **Figure 3.2**. As-prepared product contained a portion of CuPt nanospheres, 2.8 ± 0.2 nm in diameter (**Figure 3.2d**), and they can be separated by further purification *via* centrifugation. When the reaction time was extended to 3 h, there were still a large amount of nanospheres observed in the product. **Figure 3.2e** presents a HRTEM image of three nanorods. As marked by the arrows, a *d*-spacing of 0.218 nm was measured from the lattice fringes, which is assigned to the (111) planes of CuPt 1: 1 alloy. EDX analysis shows a Cu: Pt atomic ratio of 46: 54, consistent with a nearly 1: 1 CuPt alloy composition. The crystallographic orientations are obviously not uniform either within one single rod or among different rods.

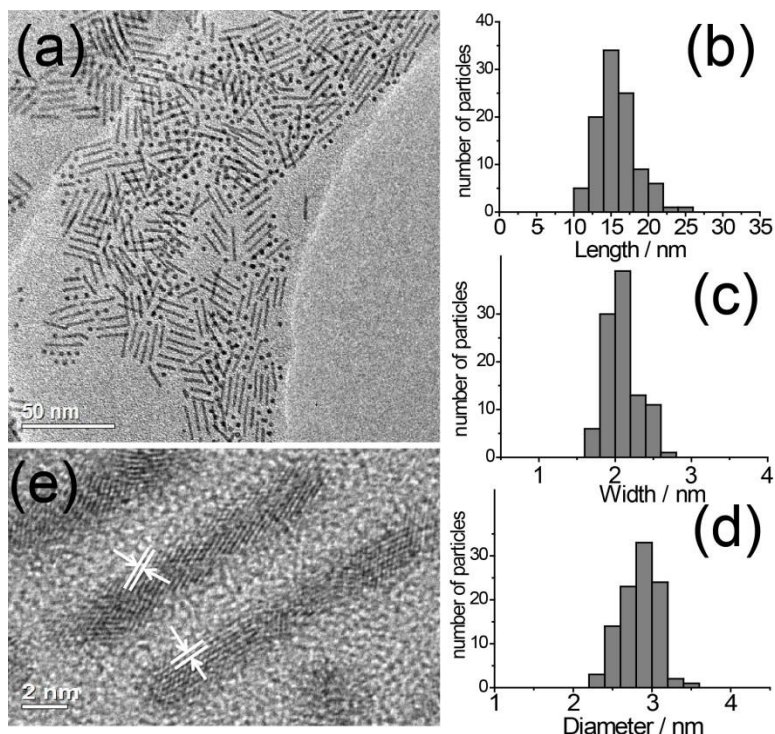


Figure 3.2 (a) TEM image of as-synthesized CuPt sample after 0.5 h reaction. (b-d) Histograms are displayed of (b) length of the rods, (c) width of rods and (d) diameter of nanospheres. (e) HRTEM image of three nanorods. The lattice fringes marked by the arrows are measured to have a *d*-spacing of 0.218 nm, corresponding to the (111) planes of CuPt.

Both nanospheres and nanorods are well aligned with a uniform distance from each other. Owing to their uniform size, they can self-organize on the carbon film during the evaporation of solvent (**Figure 3.2a**). The concentration of rods in the droplet gradually increased as it vaporized. As a result, the uniform distance between these rods is kept by the ligands on rods' surface, regardless of deposition concentration. An inter-particle spacing of ~2.3 nm is observed, maintained by the surface ligands: hexadecanoic acid and hexadecylamine. The existence of these two surface ligands is confirmed by FTIR in the latter section. Hexadecylamine and hexadecanoic acid are bound to the metallic surface *via* amine and acid functional groups, leaving behind alkyl tails pointing outwards. These rods can be well-dispersed in a non-polar solvent like cyclohexane, due to these hydrophobic tails. The length of alkyl chain of the capping agents is estimated to be ~1.9 nm long. Considering that: (1) the equilibrium distance between the alkyl chains is 4.6 Å.¹⁷ If all the surface ligands are perpendicularly absorbed on the surface, the intermolecular spacing between them then will be around 5.4 Å, considering the distance of surface atoms Cu and Pt. Therefore, the absorbed ligand molecules will tilt to achieve the shorter equilibrium distance. (2) Molecules are ranged along the curvature of the surface in a radial way, it is plausible that capping agents interdigitate into this depth. This inter-particle distance also indicates that these nanorods are covered by a monolayer of ligands.

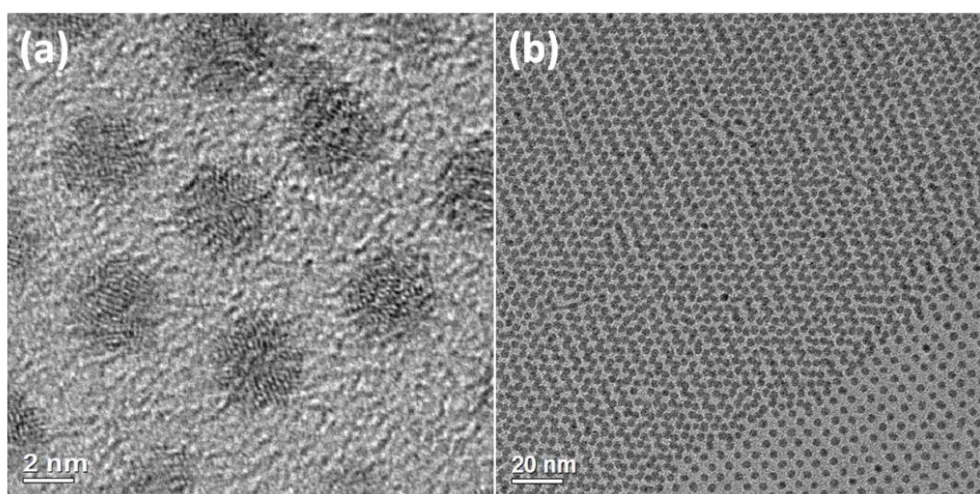


Figure 3.3 (a) HRTEM image of nanospheres from the 1: 1 sample, reaction time is 3 h. (b) TEM image of nanospheres at a low magnification showing the self-assemble of nanospheres into one layer (right bottom corner) and two layers.

As seen from **Figure 3.3**, the majority of the nanospheres are polycrystalline. They can self-assemble into a close-packed monolayer and a double-layered superstructure, when nanorods are absent. **Figure 3.3b** shows the assembly. On the left side it is double-layered while in the bottom right corner it turns into a monolayer. Likewise, these spheres are bound with surface ligands to keep them separated from each other with a uniform distance.

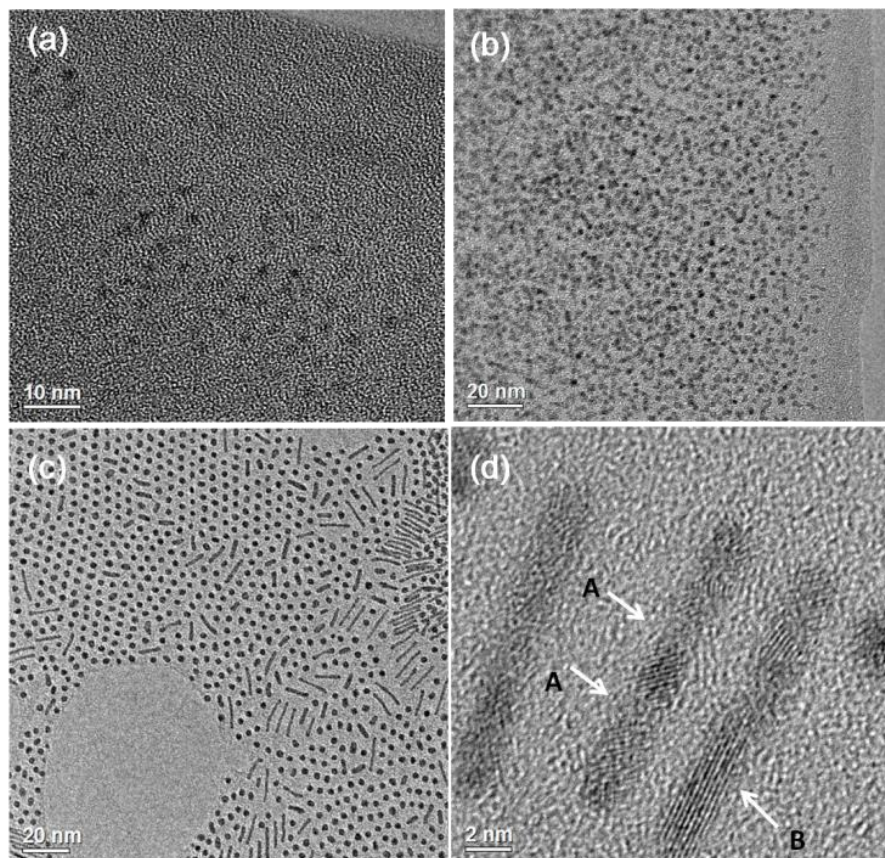


Figure 3.4 TEM images of intermediates collected at (a) 10 min, (b) 15 min, (c) 25min and (d) HRTEM image of nanorods observed from product of 3 h reaction. Boundaries between nanocrystallites are marked by arrows A and a large single crystalline domain is marked by the arrow B.

Intermediates were collected at 10, 15 and 25 min during heating from 120 °C (when the mixture was totally dissolved) to 225 °C, so as to study the growth process of the CuPt nanorods. Very small CuPt nanoparticles were produced at 10 min (**Figure 3.4a**). In the 15 min specimen (**Figure 3.4b**), nanoparticles grew up to an average diameter of 2.1 ± 0.2 nm. In comparison to the nanospheres from the final product (**Figure 3.3**) that have an average

diameter of 2.8 nm, the ones at 15 min were poorly crystalline, smaller and had a less regular shape. They were randomly sitting on the carbon film rather than well aligned. It indicates that their surfaces lack the dense coating layer. The low crystallinity of these nanoparticles may be attributed to the partially reduced metal precursors.

After 25 min, nanospheres exhibited a close-packed manner on the grid and nanorods with different lengths started to appear (**Figure 3.4c**). Notably, most of the nanorods were obviously shorter and wider than the final product at 0.5 h. Plotting the length against width of the nanorods (see scatter diagram in **Figure 3.5a**) shows that the width decreases as the length increases. This result rules out the possibility of a seeded growth mechanism, under which conditions the width would increase or at least remain unchanged.¹⁸ When reaction time was extended to 3 h, the nanorods were still polycrystalline. Obvious boundaries (arrows A) as well as single crystalline domains (arrow B) can be observed in **Figure 3.4d**. The segment regions may be caused by disorder of the atomic arrangement. In the present work, these amorphous regions appear in nanorods and are repeated in a periodic manner (about every 2–3 nm in distance). It's unlikely to form such structure in a seed-deposition growth mode, in which atoms deposit onto the existing rod.

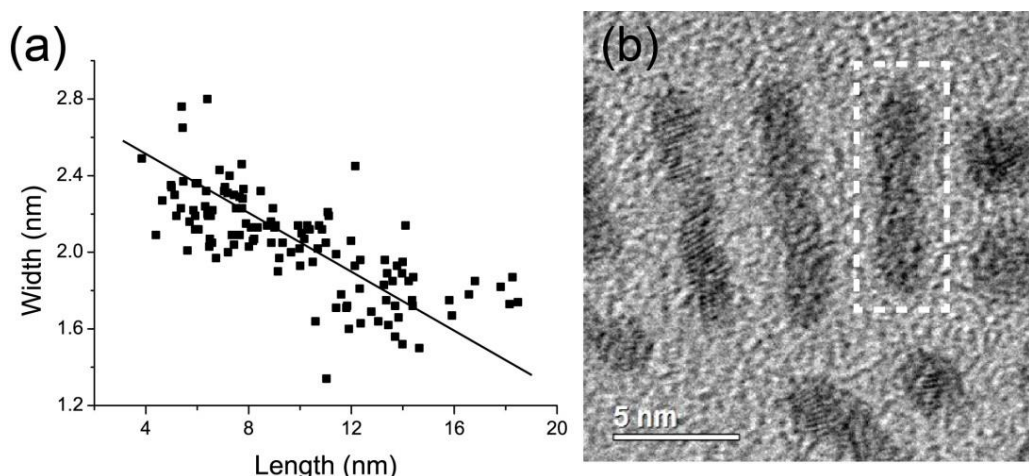


Figure 3.5 (a) Plot of width versus length of the nanorods in the 25 min sample. (b) TEM image showing a newly formed, dumbbell-shaped particle, as indicated by the dashed lines.

Figure 3.5b presents one short rod with a dumbbell shape, marked by a rectangle. It consists of two nanospheres which are joined together and show the smoothing process is not yet complete. The join has a concave shape, which has lower chemical potential. As a result, atoms on the surfaces of the spheres would migrate to the join, to fill up the gap. Consequently, the newly formed rods have a smaller diameter than that of the original spheres. This explains why the rods become thinner as the length becomes longer.

Observations above reveal that nanorods are formed *via* attachment of nanospheres as building units. The spherical crystallites fuse to produce single crystalline domains *via* further Ostwald ripening process. Long rods grow slower than the shorter ones due to diffusion-controlled growth. Consequently the size distribution is narrowed, similar to the “focusing” effect.¹⁹

3.1.4 Crystallographic orientation of CuPt nanorods

Many as reported 1D nanomaterials grow along one specific crystallographic orientation to eliminate pairs of high energy facets, for instance growth along the [111] zone axis of Au nanowires and [001] of TiO₂ nanorods *etc.*^{9, 10} After examining many HRTEM images of CuPt nanorods, it turns out that nanorods in the present work do not grow along one uniform crystal zone axis.

Figure 3.6 shows some examples of the different crystallographic orientations in the nanorods. The red lines in the figures represent the growth direction of nanorods, while the yellow arrows show the [111] direction. Different angles are observed between these two directions, which suggest that the nanorods do not grow along a uniform direction. For example, in **Figure 3.6a**, the rod grow along a direction perpendicular to [111], which is most likely to be the [110] or [211] direction. In **Figure 3.6d**, the growth direction has an angle of 55 °with [111] direction. This rod is likely to grow along [100] direction.

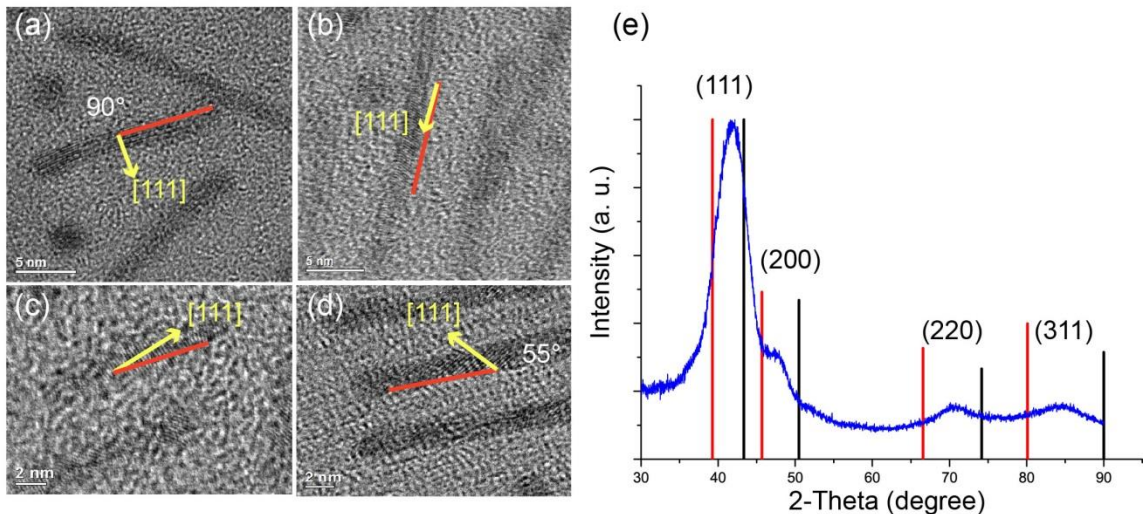


Figure 3.6 (a-d) HRTEM images of nanorods with various growth directions. Growth directions and [111] directions are marked by red lines and yellow arrows respectively.(e) XRD pattern of CuPt nanorods. Red and black vertical lines indicate peak positions of pure Pt and Cu respectively.

Moreover, the XRD pattern on the right in **Figure 3.6e** gives broadening peaks. According to the Scherrer equation, the crystal size is calculated to be about 2 nm in all zone axes.

Zone axis	(111)	(200)	(220)
Calculated crystal size/nm	1.86	2.17	1.85

In addition, the XRD pattern also indicates an alloyed CuPt phase. All peaks are located between positions of pure Cu and Pt. Two sets of peaks would be observed if Cu and Pt are segregated in the sample. HRTEM images (such as **Figure 3.4d**) have shown the spherical nanocrystallites have different crystallographic orientations within one rod. This implies the crystallographic orientation is not the dominant factor for a one-dimensional assembly. The 1D growth of nanorods must result from a different factor.

3.1.5 Effect of surface ligands

In the standard synthesis, hexadecylamine and hexadecanoic acid were applied as surface ligands. Replacing them with similar amine and acid with different alkyl chain lengths—octylamine and octanoic acid (C8), dodecylamine and dodecanoic acid (C12) and octadecylamine and stearic acid (C18) can notably alter the lengths of prepared nanorods. Using C8, C12 and C18 produced nanorods with a length of 9.5 ± 1.8 nm, 11.4 ± 1.6 nm and 15.2 ± 3.0 nm, respectively (**Figure 3.7 a-c**).

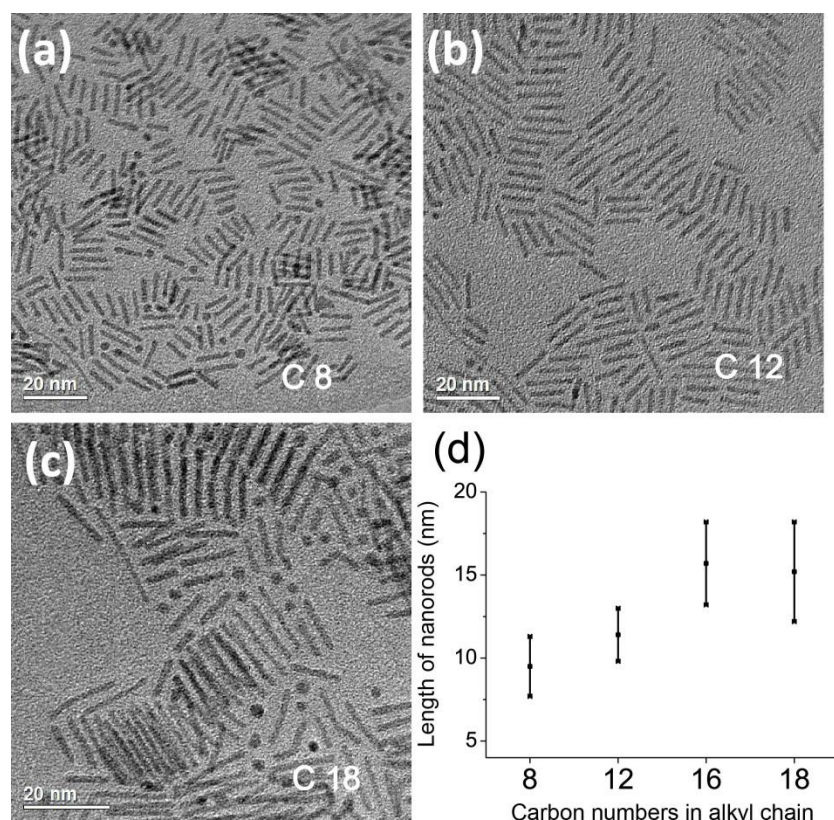


Figure 3.7 TEM images of nanorods prepared with (a) octylamine and octanoic acid (C8), (b) dodecylamine and dodecanoic acid (C12), and (c) octadecylamine and stearic acid (C18). (d) Diagram showing the relationship between nanorod lengths and alkyl chain lengths of the ligands.

Figure 3.7d summarizes the variation of length of the nanorods dependent on carbon numbers in ligand alkyl chain. Rods prepared with C8, C12 and C18 ligands have inter-particle spacings of 1.9 nm, 2.0 nm and 2.3 nm, respectively, which are consistent with the increasing

ligand length. It has been demonstrated that changing surface ligands can simply tune the lengths of nanorods. Because these ligands are merely different in alkyl chain, their chemical properties remain similar. This suggests that the growth of nanorods is strongly influenced by the supramolecular organization of surface ligands.²⁰ Increasing the length of alkyl chains enhances ligand-ligand interaction. With the assistance of short distance interactions from ligand alkyl chains, longer rods are well stabilized. On the other hand, too long chains may make organization and ordering difficult. Replacing the ligands to C18 did not produce longer nanorods.

Standard preparation condition with metal: amine: acid = 1: 9: 9 is referred to amine: acid = 1: 1 (**Table 3.1**). Raising amine: acid to 1.5: 1 by increasing the amount of amine will produce nanorods with an average length of 24.3 ± 5.3 nm (**Figure 3.8c**). Further increase of amine amount to a ratio that amine: acid = 2: 1 yielded nanorods of 28.9 ± 9.4 nm (**Figure 3.8b**). Increasing the amine content to result in longer rods is a reported phenomenon in literature.^{14, 21} But the detailed roles of the surface ligands have not been elucidated. To study the effect of acid and amine on rod morphology, a series of further experiments were carried out.

It is found that increasing the amount of acid to amine: acid = 1: 1.5 produced shorter rods (length: 11.7 ± 2.0 nm, see **Figure 3.8a**). Keeping the ratio of amine: acid = 1: 1 constant, increasing both surface ligands to 1.5 (amine: acid = 1.5: 1.5), resulted in rods with length of 24.0 ± 5.2 nm (**Figure 3.8e**), close to the length of rods prepared with amine: acid = 1.5: 1. Reducing both surface ligands to 0.5 (amine: acid = 0.5: 0.5) led to products containing mainly smaller spherical particles (~2 nm in diameter, see **Figure 3.8d**). In the presence of only acid, nanospheres with uniform sizes and a small amount of short rods were formed (**Figure 3.8f**). When amine is the sole surface ligand, the metal precursors were decomposed/reduced at lower temperature (~130 °C) and nanoparticles with wide size distribution were obtained (**Figure 3.8g**).

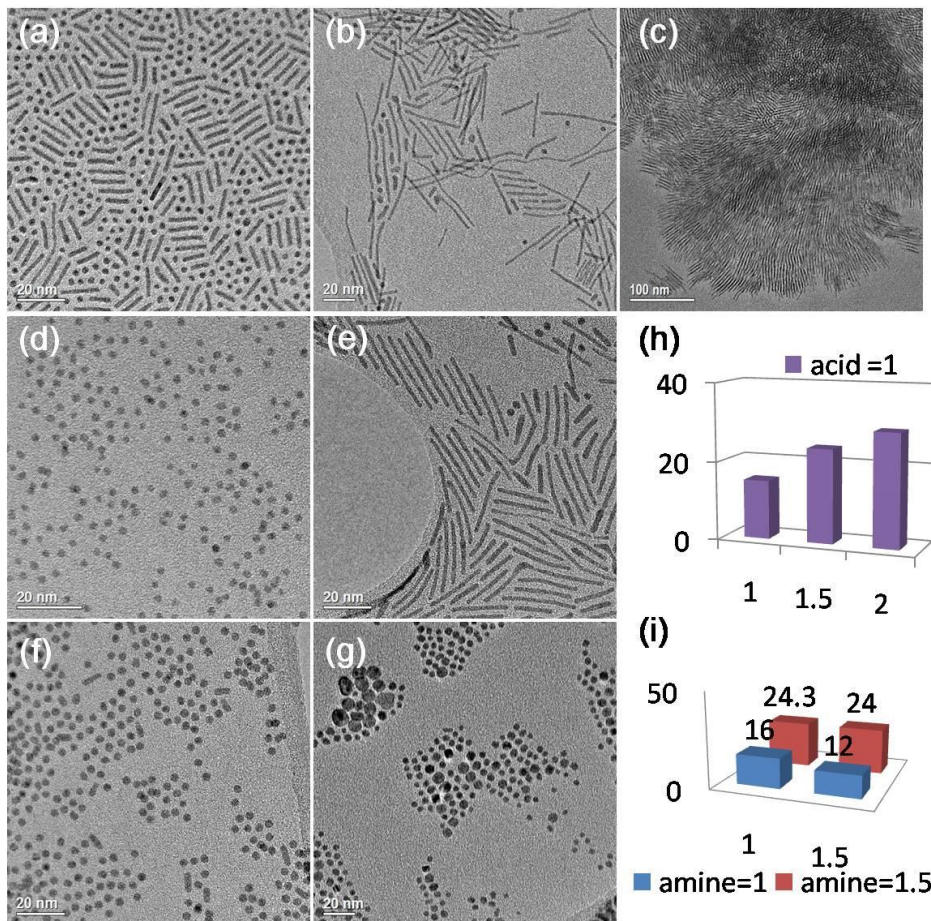


Figure 3.8 (a-g) TEM images of CuPt nanoparticles prepared with different amount of amine and acid. Amine: acid ratios (a) 1: 1.5, (b) 2: 1, (c) 1.5: 1, (d) 0.5: 0.5, (e) 1.5: 1.5, (f) acid alone and (g) amine alone. (h) Graph demonstrating that when the amount of acid remained as 1, increasing amine concentration resulted in longer rods. (i) Graph showing that when amine concentration was either 1 or 1.5, increasing acid concentration did not change the rod length much.

These results are summarized in the charts in **Figure 3.8h, 8i**. When the acid concentration is constant, increase of the amine concentration will lead to longer rods. Keeping the amine concentration constant but increasing the acid concentration has no significant effect on rod length.

Observations on the early stage intermediates suggest that the metal precursors may aggregate with organic ligands into nanospheres, after that decomposition and reduction of the precursor molecules may occur. The nanospheres may further grow *via* deposition of metal precursor molecules, and metals don't have to be fully reduced to zero-valent atoms. It is

supported by theoretical study,^{22,23} revealing that addition of ions to growing clusters takes place before their reduction. HRTEM images also revealed early stage particles have a low crystallinity. Therefore partially reduced Pt and Cu cations may be contained within the nanospheres. This state prefers surface adsorption of organic acidic molecules that have carboxylic group with negative charge. This is one reason to explain why acid serves as a stronger ligand than amine. Therefore, nanospheres with a uniform size can form in the acid-alone system (**Figure 3.8f**), but not in the amine-alone system (**Figure 3.8g**). As the metals are gradually reduced to zero-valent, adsorption of mixed acid and amine is favored in term of neutralized charge. Theoretical calculations have found that adsorption of amine functional group is preferred over the carboxylic acid group on zero-valent PtAg surface.²⁴ A similar situation in CuPt rods is expected in the present case where amine adsorption is favored when CuPt is fully reduced. Increasing of the amine concentration in the solution is able to facilitate amine adsorption, probably with partial replacement of surface acid. Experimental evidence from IR characterization is presented in a later section. Elongation of nanorods occurs owing to the increase of surface ligand density, under which circumstances the ligand interactions is enhanced to better stabilize long rods. In contrast, increasing the acid concentration in solution gives no help to increase the surface density. As a result, the length of the nanorods remains constant in spite of the extra acid.

It is known that surface ligands can help reduce monomer oversaturation.²⁵ When half the amount of amine and acid (0.5: 0.5 in **Figure 3.8c**) is used, nucleation is less suppressed and rapid in this solution with a low surface ligand concentration. This results in a large number of nanospheres with smaller sizes. On the other hand, surface ligands on these nanospheres are loosely bound, and their interactions are drastically weakened due to the low density, which is not sufficient to drive the formation of nanorods. Similarly, a reduced ligand density could be one reason to explain why nanospheres are obtained with only acid as a surface ligand.

In summary, the nominal ratio between the amine and acid determines the ligand density on surface of the spheres, which plays a critical role in subsequent nanorods formation.

3.1.6 Two-step synthesis

A two-step synthesis was performed to verify the mechanism. As discussed previously, mainly nanospheres were obtained when acid alone was used as a surface ligand (**Figure 3.9a**). The acid-capped nanospheres were used as the starting material, then amine was added into the mixture in the second step. Surprisingly, strands of CuPt nanowires were produced (see **Figure 3.9b**). The total length of these strands can be as long as several dozen micrometers. **Figure 3.9c** shows ultrathin, around 1.5 nm wide, CuPt nanowires with some nanospheres incorporated in the strands. These nanowires stack together so as to form large pieces. These nanowires have a relatively high crystallinity, as crystal fringes could be observed from HRTEM images in **Figure 3.9d**. EDX examination shows a Cu: Pt ratio of 42: 58.

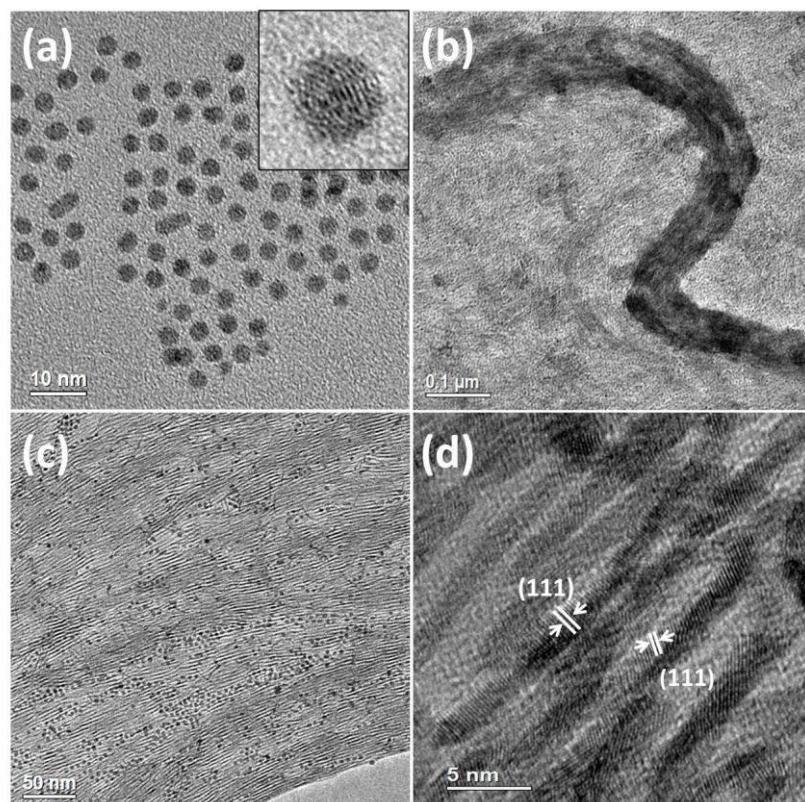


Figure 3.9 TEM images of (a) CuPt nanoparticles prepared with only acid in the first step. The inset is a HRTEM image of a sphere with lattice fringes. (b) Strands of CuPt nanowires synthesized by two-step method. (c) TEM and (d) HRTEM images of ultrathin nanowires inside the strand. The lattice fringes have a *d*-spacing of 2.16 Å, corresponding to (111) planes.

As-prepared nanospheres were used as the starting reactants in **Figure 3.9a**, which had already been reduced to nanocrystals with good crystallinity (see inset of **Figure 3.9a**, lattice fringes can be observed). Amine did not participate in any nucleation process. Therefore, the elongation could only be induced by the addition of amine in the second step. This experiment supports the proposed sphere-to-rod mechanism.

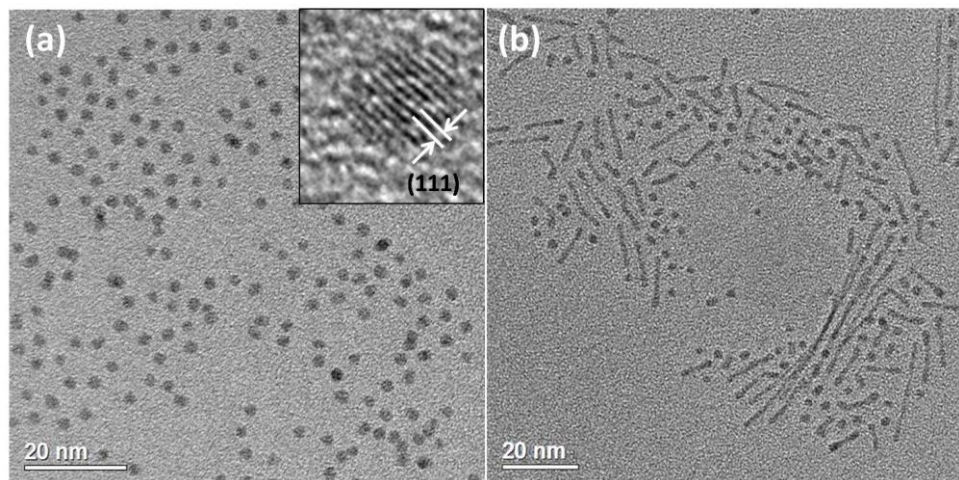


Figure 3.10 TEM images of (a) CuPt nanospheres prepared with amine: acid = 0.5: 0.5 in the first step. Inset is a HRTEM image of a nanosphere. (b) Following the addition of amine: acid = 1: 1 to the mixture in the second step, elongated nanorods were produced.

This two-step method can also be applied to the system of nanospheres prepared with amine: acid = 0.5: 0.5. Using these nanospheres as the starting material (**Figure 3.10a**) and adding amine and acid in the second step, caused elongation to occur and the formation of some nanorods (**Figure 3.10b**). Since both amine and acid were used, the nucleation environment was exactly the same as that in the one-step synthesis. The evolution of rods from spheres was caused by the addition of more ligands in the second step, which can increase the ligand density on the surface.

The two-step synthesis results above provide evidence for the sphere-to-rod mechanism. Density of surface ligands is crucial for 1D growth of CuPt nanorods. This implies that surfaces of nanospheres need to reach a threshold ligand density before they begin to join

together. Once the threshold density is satisfied, nanorods can start to form, in which process uniform crystallographic orientations are not necessary. It is an interesting yet unanswered question why very long nanowires formed following the addition of amine to acid-capped nanospheres. Amine would displace or insert into carboxylate species that already exist on the surface. One possibility is that amine invasion neutralizes the negative charge of acid and this process leads to the fast growth of nanospheres into long nanowires.

3.1.7 Surface characterization of the CuPt nanorods

Thermogravimetric analysis (TGA) and Fourier Transform Infrared (FTIR) characterizations were carried out on CuPt nanorods to investigate the surface species. Direct observation of the organization of the ligand shell by TEM is difficult under our experimental conditions because the ligand molecules of amine and acid only contains light elements and give quite light image contrast. However, Rupar *et al.*²⁶ have observed cylindrical micelles consisting of a monolayer coil shell and a crystalline core under TEM, which are formed by self-assembly of block copolymers containing heavy atoms. A monolayer shell of amine and acid can be expected to resemble the cylindrical micelles configuration on CuPt rod surface.

TGA of 1: 1 amine and acid sample gives a weight loss of 24.9 % in **Figure 3.11**. The molecular weight of surface ligands and CuPt alloy are listed below.

	hexadecylamine	hexadecanoic acid	CuPt
Molecular weight	241.5	256.4	258.6

The weight loss of 24.9 % from TGA corresponds to a ratio of ligand molecules: metal atoms = 1: 5.88. Assuming the sample consists of 75 % nanorods with length of 15.7 nm and width of 2.1 nm and 25 % nanospheres with the diameter of 2.8 nm. The metal atom density of all the surfaces are assumed to be the same as that of (100) face in the face-centered-cubic

unit cell, therefore the product has approximately 40 % atoms on the surface. Therefore, the result is ligand: metal atom = 1: 2.32. This density means one ligand on every two atoms on surface. This is a calculated result, and could be a bit larger than the real surface ligand density. Surface atom percentage out of bulk atoms could be less than 40 %, caused by the amorphous boundaries existing in the polycrystalline rods. It is worth mentioning that the specimen of amine: acid = 2: 1 has a larger weight loss of 32.2 %. It validates our previous assumption that increasing the amine concentration in the solution will increase the density of surface ligands, thus resulting in longer rods.

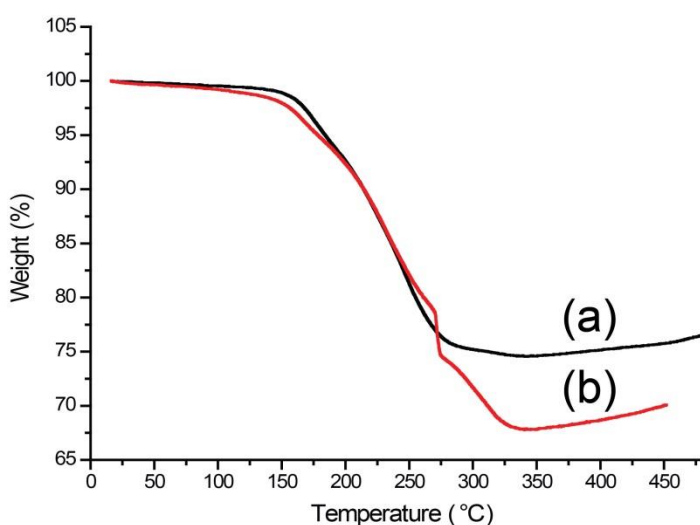


Figure 3.11 TGA results from the amine: acid of (a) 1: 1 and (b) 2: 1 nanorod samples.

IR spectra from different samples are displayed in **Figure 3.12**. Bands at about 2950, 2915 and 2848 cm^{-1} are observed commonly in the spectra, and can be attributed to the asymmetric stretch of CH_3 , asymmetric stretch of CH_2 and symmetric stretch of CH_2 , respectively. Bands located at 1473 and 1461 cm^{-1} may be from the CH_2 scissor modes of the methylene units. These bands are expected for both amine and acid.

For the pure mixture of amine and acid in **Figure 3.12a**, the absence of a band at 1700–1750 cm^{-1} indicates that no free carbonyl band exists associated with $-\text{COOH}$.²⁷ The well-defined peak at 1639 cm^{-1} is only present in **Figure 3.12a**, and may be associated with the $\delta_{\text{asym}}(\text{NH}_3^+)$ mode. The band located at 1508 cm^{-1} falls in the range of the symmetric NH_3^+

deformation.²⁸ The band at 1402 cm^{-1} might be assigned to the symmetric stretch of the carboxylate. Hence this spectrum consistently matches a mixture of carboxylate species and alkylammonium ions.

Spectrum of nanoparticles prepared with acid alone is shown in **Figure 3.12b**. The two broad bands at 1560 cm^{-1} and 1416 cm^{-1} are characteristic for the ν_{asym} and ν_{sym} (OCO) of the adsorbed carboxylate. In fact, this spectrum resembles very closely that reported for hexadecanoate on aluminum.²⁹ The band centered at 2048 cm^{-1} is assigned to adsorbed CO on Pt-like sites, possibly owing to the decomposition of acid. The especially weak band at 1699 cm^{-1} ($\nu\text{ C=O}$) is associated with a small amount of carbonyl, which may be derived from free acid. From this spectrum, it can be concluded that acid bonds to the metal surface *via* carboxylate.

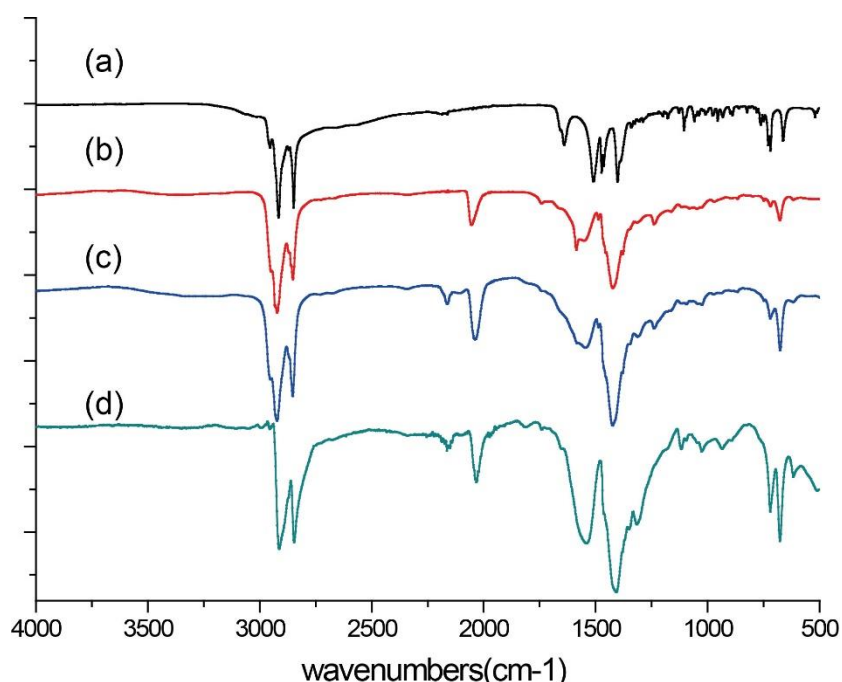


Figure 3.12 IR spectra of (a) mixture of 1: 1 amine and acid, (b) nanoparticles prepared with acid only, (c) nanorods prepared by a two-step method with amine and acid and (d) nanorods prepared in standard synthesis with amine: acid = 1: 1.

The IR spectrum of nanorods prepared by a two-step method is shown in **Figure 3.12c**. It has an extra band located at 2158 cm^{-1} compared to **Figure 3.12b**. This band is probably a

C=N stretch from adsorbed nitrile derived from dehydrogenation of the amine.³⁰ The IR spectrum from the sample with amine: acid = 1: 1 (**Figure 3.12d**) resembles that in **Figure 3.12c**. In both spectra, there is dominant feature of adsorbed carboxylate. But the spectrum in **Figure 3.12d** has a broadened 1550 cm⁻¹ band at higher wavenumber, which may be contributed from adsorbed amine or related species that has amine or alkylammonium bands in the 1580-1630 cm⁻¹ range. It can be concluded from these two spectra that both amine and acid are adsorbed.

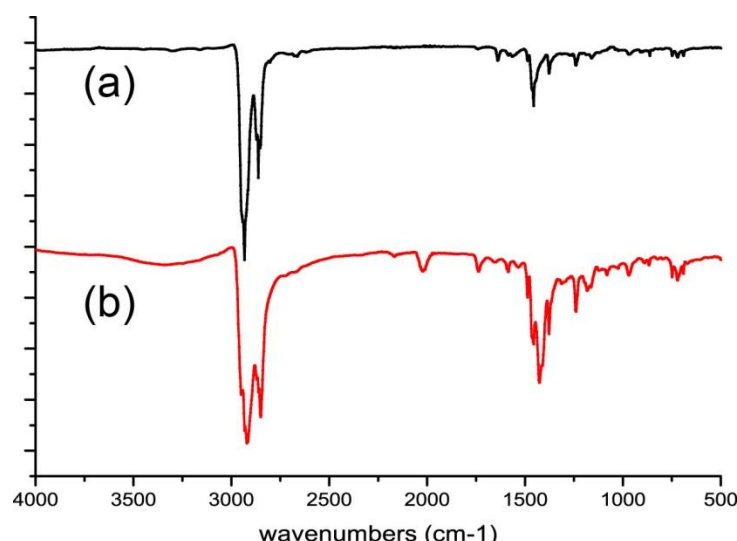


Figure 3.13 IR spectra of CuPt nanorods synthesized with (a) amine: acid = 2: 1 and (b) amine: acid = 1.5: 1. The $\nu_{\text{sym}}(\text{OCO})$ band at 1420 cm⁻¹ is observed in spectrum (b), but not in spectrum (a). Instead, the bands observed in spectrum (a) indicate that amine adsorption is dominant under these preparation conditions.

As the amine: acid ratio increases, for instance in the samples of 1.5: 1 and 2: 1, the amine adsorption becomes more obvious and carboxylate adsorption becomes increasingly less apparent (**Figure 3.13**). The amine and acid appear to adsorb competitively such that the adsorption of amine is enhanced by increasing the concentration in a one-step synthesis. A monolayer of ligands with a high density is formed on the nanorod surface when the amine concentration is increased, leading to longer nanorods.

In summary, TGA results indicate the surface of nanorods is covered by a dense layer of ligands. FTIR confirms the existence of both amine and acid adsorbed on nanorod surface.

Increasing the amine concentration in a solution will increase amine adsorption and further lead to longer rods, consistent with our previous assumption.

3.1.8 Proposed formation mechanism

Based on the experimental results, a formation mechanism of nanorods controlled by the organization of surface ligands is proposed. Previous reports^{9, 11} have proposed that the anisotropic growth of nanorods are caused by preferential coordination of ligands to a particular facet, or guided by dipole-dipole interactions to form 1D structures. Either theory cannot well explain the case in the present work. Experimental results above have excluded the probability of seeded growth or oriented attachment:

- (1) The width of intermediate nanorods decreases with increasing length, while seeded growth nanorods prepared *via* atomic deposition should have unchanged or increased width.
- (2) Nanorods can form merely using nanospheres as starting materials, in the presence of surface ligands. No deposition process is involved in this 2-step synthesis.
- (3) Changing the alkyl chain length of amine and acid molecules can alter the length of nanorods.
- (4) The nanorods are polycrystalline; nanocrystallites within one single rod can have various crystal orientations.

The fact that simply changing the ratio of amine and acid can tune the rod length suggests surface ligands play a crucial role. Based on the experimental evidences and surface analysis, a stable monolayer of surface ligands is believed to drive the 1D growth. To understand the formation mechanism of the nanorods, explanation of the connections among three spherical units will be enough. The mechanism is illustrated in **Figure 3.14**.

Either the amine or the acid, (or a mixture of both species), is bound to the nanosphere surface *via* the terminal functionality. The nanospheres move randomly in the solution with

the action of Brownian motion, solution convection and stirring, until two spheres stochastically collide. Then they fuse to form a dumbbell-shaped short rod (**Figure 3.14b**), in which process the removal of surface ligands may be involved.¹¹ Atoms on the nanospheres would migrate to the concave joint that has lower chemical potential. The “neck” goes through smoothing process, resulting in uniform circular cross-sections (**Figure 3.14c, 14d**). In this situation, nearly all the ligands are parallel to each other with stable distances on side surface, which reduce the surface energy and stabilize the side surface. Van der Waals interactions between neighboring alkyl chains drive the formation of a densely packed ligand shell. A cylinder-like secondary particle (**Figure 3.14d**) formed, which has decreased total energy in consequence of organized and denser surface ligands and elimination of solid-liquid interface.⁷ There is no crystallographic requirement for such attachment, thus the nanorods are polycrystalline containing nanocrystallites with random orientations.

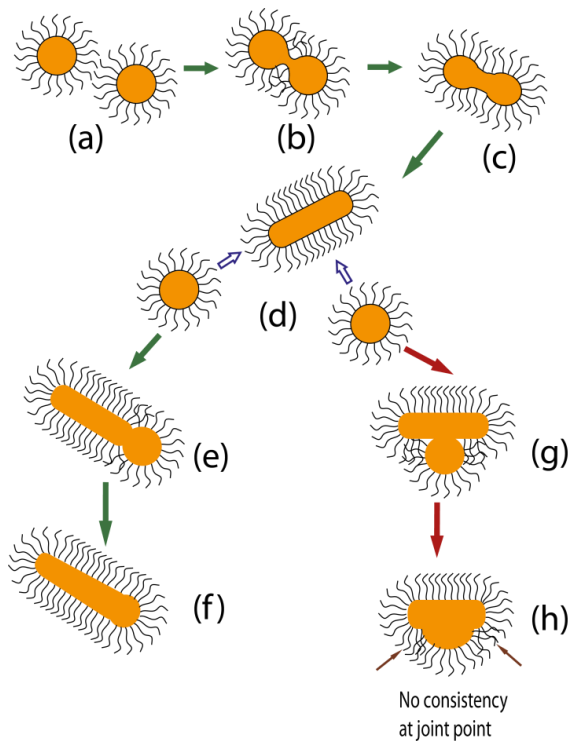
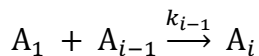
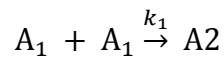


Figure 3.14 Illustration of nanorod formation controlled by the structure of the surface ligands.

The Smoluchowski equation,³¹ which has been proven to fit well for the attachment kinetics of organic ligand capped nanocrystals,^{32, 33} can analogously describe the attachment model in the present system. The model of the Smoluchowski equation involves monomer-monomer reaction and addition of monomer to multimer, and multimer-multimer reaction can be neglected.^{32,34} It can be expressed as:



In which, A_1 is a primary nanosphere, A_i is a nanorod containing i primary spheres, and k is the reaction rate constant.

It is extraordinary that the nanospheres can attach together one-dimensionally. There must be some special guiding force involved, otherwise how can the absence of branched shapes be explained? It is suspected the total energy of surface molecular organization is the dominant factor in the 1D growth. If the third sphere approaches the cylinder linearly (**Figure 3.14e**), orientations of surface ligands on the sphere and cylinder particles are consistent (**Figure 3.14f**). This guarantees the highest density of molecules bound to surface. On the contrary, a nanosphere that moves towards the side surface to form a quasi-triangle (**Figure 3.14g**) suffers strong repulsive forces from adsorbed molecular species. Under this circumstance, the ligands located at the contact points have to completely reorganize, and a triangular plate needs to be formed as a prerequisite (**Figure 3.14h**). Hence, route (d)-(e)-(f) occurred preferentially but route (d)-(g)-(h) was barely observed.

All of the experimental results support this ligand-mediated hypothesis. A mathematical model has demonstrated in the case of Au nanorods³⁵ that the ratio of surface energy between side and cap surfaces, i.e. $S = S_{\text{side}}/S_{\text{cap}}$ determines the final aspect ratio. This model is in accordance with our mechanism in that no restriction was put on the growth rates of various crystallographic directions. Due to the limited knowledge of theoretical chemistry, simulations of interactions of surface ligands were not carried out in the present work, but hopefully will

be conducted in collaboration with theoretical chemists in the future, to better support and validate this mechanism.

Based on the mechanism, it can be assumed that the attachment of a nanosphere to another nanosphere or to a nanorod only takes place when (1) the surface is covered by a sufficiently dense layer of ligands; (2) their size are properly matched.

3.1.9 Photocatalysis performance

This work was carried out by Dr. X. Xu from University of St Andrews. CuPt nanorods were loaded on C₃N₄ as co-catalyst and applied to generate hydrogen from water under visible light ($\lambda \geq 420$ nm). Pure Pt nanorods prepared by the same method only in absence of Cu precursor were also tested for comparison (**Figure 3.15**).

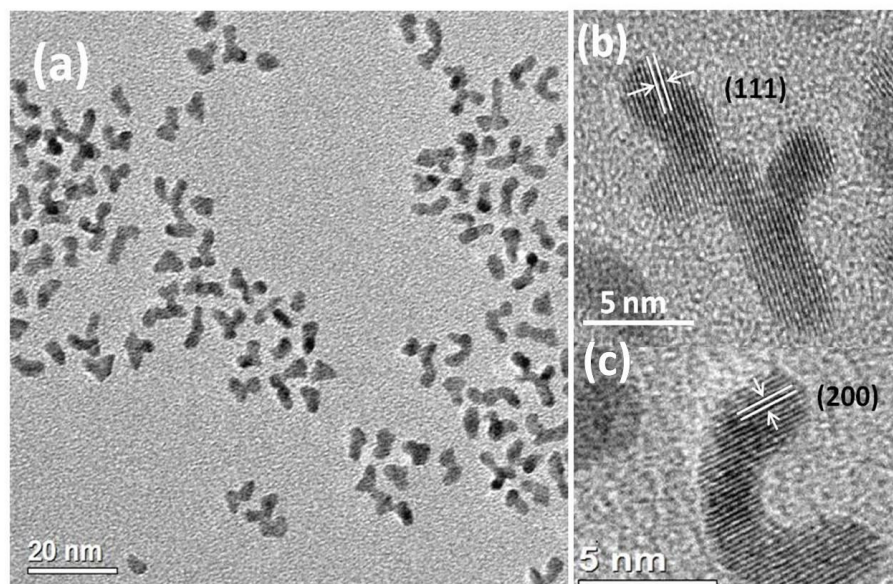


Figure 3.15 (a) TEM and (b,c) HRTEM images of pure Pt nanorods prepared under the same experimental condition as described in section 3.1.2.

As shown in **Table 3.2**, the activity of C₃N₄ is significantly improved after loading of metallic nanorods. It is noteworthy that the H₂ production rate of CuPt nanorods is 3.5 times

higher than that of pure Pt nanorods. It is known that cocatalysts promote catalytic reactions by collecting charges generated on semiconductors.³⁶ Therefore loading either CuPt or Pt nanorods can considerably enhance the catalytic activity. The better performance of CuPt over Pt nanorods may be attributed to the following three factors. (1). The work function of Cu is smaller than that of Pt (Cu: 4.53~5.10 eV, Pt: 5.12~5.93 eV).³⁷ Alloying with Cu may lower the Schottky barrier between metal CuPt and semiconductor g- C₃N₄, thus electrons transferring from g- C₃N₄ to CuPt nanorods is promoted. (2). The connections between adjacent Pt atoms are broken down by introducing Cu for substitution, in a manner that is analogous to isolated Pt clusters. Quantum size effect could be another reason. (3). The CuPt nanorods are polycrystalline, containing a large quantity of structural defects. As shown in **Figure 3.15**, it is obvious that pure Pt nanorods have a higher crystallinity. The positive effect of defects for photocatalysis activity should not be neglected.

Table 3.2 Photocatalytic hydrogen production rate for different samples under visible light.

Sample	H ₂ production rate (μmol h ⁻¹ /g catalyst)
Pure g-C ₃ N ₄	1.65
g-C ₃ N ₄ + 1wt % Pt nanorods	66.35
g-C ₃ N ₄ + 1wt % CuPt nanorods	234.08

3.2 Ligands capped monometallic, bimetallic and trimetallic nanoparticles

Monometallic Cu and Pt, bimetallic CuPd, PdPt and trimetallic CuPdPt nanoparticles were prepared under the same experimental conditions as that of CuPt nanorods, except for the usage of different metal precursors. Cu(acac)₂, Pd(acac)₂ and Pt(acac)₂ were used as metal precursors in these preparations. These single metal or alloy products were characterized by XRD, EDX, TGA and HRTEM. The relationship between the adsorption of surface ligands and morphology is discussed.

3.2.1 Experimental section

Synthesis of Cu and Pt monometallic nanoparticles

Either 40 mg of Pt(acac)₂ or 26 mg of Cu(acac)₂ was mixed with 35 mg of 1,2-decanediol as reducing agent, 230 mg of hexadecanoic acid and 225 mg of hexadecylamine in 5.0 mL of diphenyl ether solvent in a round-bottom flask. The mixture was heated to 120 °C until a clear solution was obtained. The solution was then heated to 225 °C and reacted for 30 min. The flask was removed from the heating mantle and cooled down to room temperature. The product was collected by centrifugation and washed several times with ethanol.

Synthesis of CuPdPt trimetallic nanospheres

To prepare CuPdPt nanoparticles, 20 mg of Pt(acac)₂, 15 mg of Pd(acac)₂ and 13 mg of Cu(acac)₂ were mixed with 53 mg of 1,2-decanediol, 345 mg of hexadecanoic acid and 338 mg of hexadecylamine in 5.0 mL of diphenyl ether. In the synthesis of Cu₂PdPt nanoparticles, 20 mg of Pt(acac)₂, 15 mg of Pd(acac)₂ and 26 mg of Cu(acac)₂ were mixed with 70 mg of 1,2-decanediol, 460 mg of hexadecanoic acid and 450 mg of hexadecylamine in 5.0 mL of diphenyl ether. The reaction and post-processing procedures are the same as described above.

Synthesis of CuPd and PdPt bimetallic nanoparticles

15 mg of Pd(acac)₂, 35 mg of 1,2-decanediol, 230 mg of hexadecanoic acid and 225 mg of hexadecylamine were mixed with either 13 mg of Cu(acac)₂ or 20 mg of Pt(acac)₂ in 5.0 mL of diphenyl ether. The reaction and post-processing procedures are the same as described above.

3.2.2 Monometallic Cu and Pt nanoparticles

When Cu(acac)₂ was used as the only metal precursor, large Cu nanoparticles and long rods were produced. The Cu nanoparticles were about 30 nm to 50 nm in size, and the rods could be as long as several micrometers and ~ 30 nm wide, as shown in **Figure 3.16**. The large sizes of the products indicate the weak interactions between surface ligands and Cu. When the reaction temperature was lowered to 180 °C, only a brown solution formed and no precipitate could be collected even after high speed centrifugation for a longer period of time, which suggests Cu precursor is not easy to be fully reduced. The nucleation process of Cu is slow and the surfaces are not well protected by the ligands due to their weak interactions, therefore large Cu nanocrystals are produced.

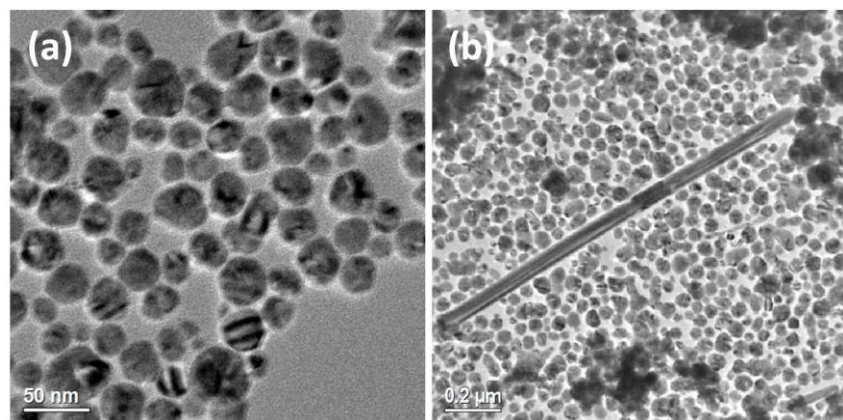


Figure 3.16 TEM images of (a) nanoparticles and (b) rods prepared with Cu(acac)₂ as the only precursor.

Pt nanoparticles with a branched structure were prepared when Pt(acac)₂ was used as a precursor (same product as that used in the photocatalysis test, **Figure 3.15**). The diameter of the nanoparticles is ~2.6 nm. After examination of many HRTEM images, it was found that the crystallographic orientations are almost uniform in these branched nanoparticles. Most particles grow along the <111> direction (**Figure 3.15b**), while the <200> can also be observed in some particles (**Figure 3.15c**). The oriented crystalline structure implies that primary

crystallites will adjust their orientations to be uniform after aggregation, probably due to the high diffusion efficiency of Pt (see **Table 3.3**).^{38,39}

Table 3.3 Self-diffusion parameters for different pure metals.³⁹

Metal	Temperature Range/ K ^a	D(T _m)/m ² s ⁻¹ ^b
Cu	1010–1352	5.97 × 10 ⁻¹³
Pt	850–1265	1.4 × 10 ⁻¹²
Pd	1323–1773	4.9 × 10 ⁻¹³

^a Temperature range of the experimental determination of D.

^b Value of D (diffusion coefficient) at the melting point.

There is more adsorption of ligands on the Pt surface than in the case of Cu, as Y-shaped nanoparticles with a smaller size are produced instead of large spheres. Here is evidence from another aspect: In the case of CuPt nanorods, Pt precursor has a higher redox potential than that of Cu thus should be reduced first and Cu should be deposited on it. But uniform CuPt alloy is formed instead of a core-shell structure, which suggests that the ligands can bind more strongly on Pt to stabilize it.

The surfaces of Pt nanoparticles are well protected and isotropic aggregation is blocked. But why does Pt form a Y-shape instead of a 1D rod? It is plausible that the formation is caused by the following two reasons. (1). Reduction of Pt precursor is so rapid that the adsorption of surface ligands is not complete. So the coalescence occurs before the complete adsorption and organization of surface ligands. (2). The effect of quick Pt diffusion and oriented crystalline structure overweighs that of ligand organization.

3.2.3 Trimetallic CuPdPt nanospheres

Trimetallic CuPdPt nanospheres were prepared with a ratio of Cu: Pd: Pt = 1: 1: 1. Nanospheres with an average diameter of ~2.7 nm were well aligned in a closed-packed manner (see **Figure 3.17a**). Self-assembly of the nanoparticles into a single layer (a), double layers (b) and multi-layers (c) can be observed (see **Figure 3.17**). CuPdPt nanospheres act as building units in a manner close to atoms in the formation of 3D superlattices.

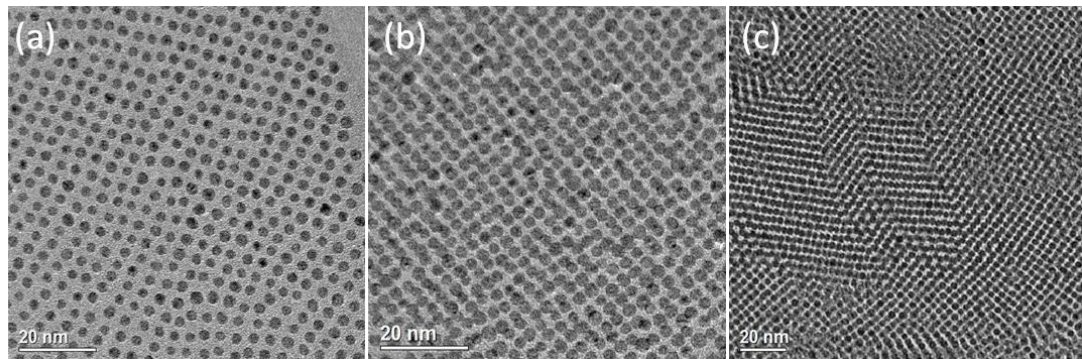


Figure 3.17 Self-assembly of CuPdPt nanodots into superlattices composed of (a) a single layer, (b) double layers and (c) multi-layers.

EDX analysis confirmed the ternary alloy composition. The XRD pattern in **Figure 3.18** shows an alloyed phase. Broadening peaks are observed, indicating the nanoscale size of the nanospheres: the calculated crystal size from (111) peak is about 2 nm, which is smaller than the TEM size due to polycrystallinity.

The preparation of trimetallic nanospheres can be extended to a Cu: Pd: Pt ratio of 2: 1: 1. Similar nanospheres were obtained and the corresponding XRD pattern shifted a little towards the high angle 2θ direction, owing to the increase of Cu composition.

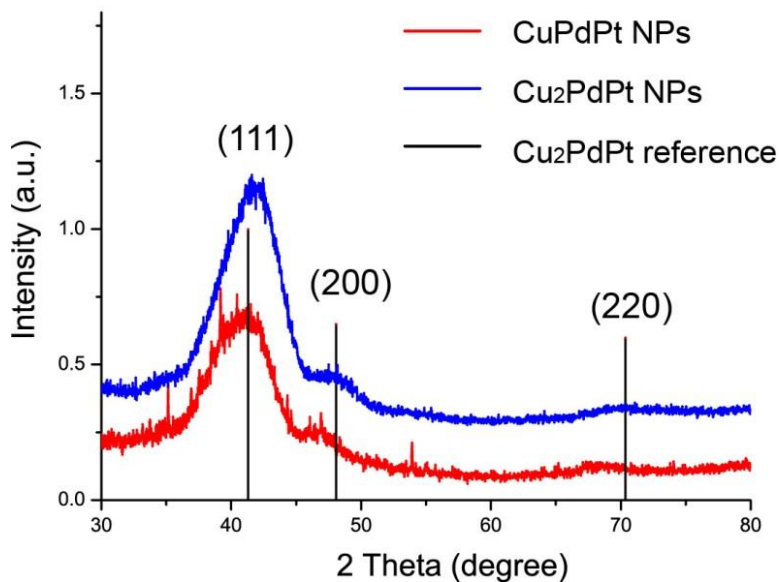


Figure 3.18 XRD patterns of CuPdPt nanoparticles (red) and Cu₂PdPt nanoparticles (blue). The black vertical line marks the position of reference Cu₂PdPt alloy (JCPDS 00-048-1550).

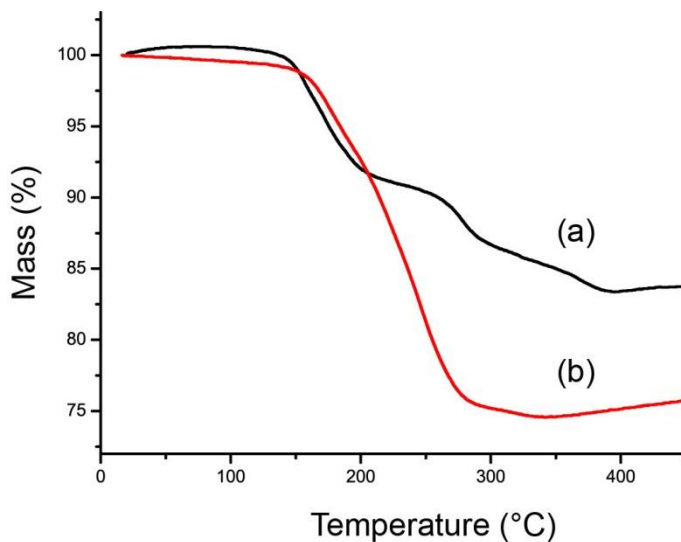


Figure 3.19 TGA results of (a) CuPdPt nanospheres and (b) CuPt nanorods.

To investigate why the CuPdPt ternary system produces nanospheres rather than nanorods, TGA was performed on the CuPdPt nanospheres. TGA examination of CuPdPt nanospheres gave a weight loss of 16.6 %, which is smaller than 24.9 % of CuPt nanorods (see **Figure 3.19**). The calculated molar ratio of ligand to metal atoms in CuPdPt nanospheres is 1: 10.23, while that of CuPt nanorods is 1: 5.88. This indicates that Pd has a weak adsorption

ability towards ligands, leading to a decreased surface ligand density. It is consistent with our previous assumption that the loosely bound surfaces will result in nanospheres. By far, it is deduced that the adsorption ability ligands can be described as: Cu < PtPd, Pd < average CuPt < Pt.

3.2.4 Bimetallic CuPd and PdPt nanoparticles

CuPd nanospheres were produced by using Cu(acac)₂ and Pd(acac)₂ as precursors and repeating the same experimental procedures (**Figure 3.20**). The sizes of the CuPd nanospheres range from 2 nm to 3 nm. **Figure 3.20d** displays a HRTEM image of nanospheres. The lattice fringes with a *d*-spacing of 1.87 Å, can be indexed to (200) planes of CuPd 1: 1 alloy (Cu d_{200} = 1.808 Å, Pd d_{200} = 1.945 Å).

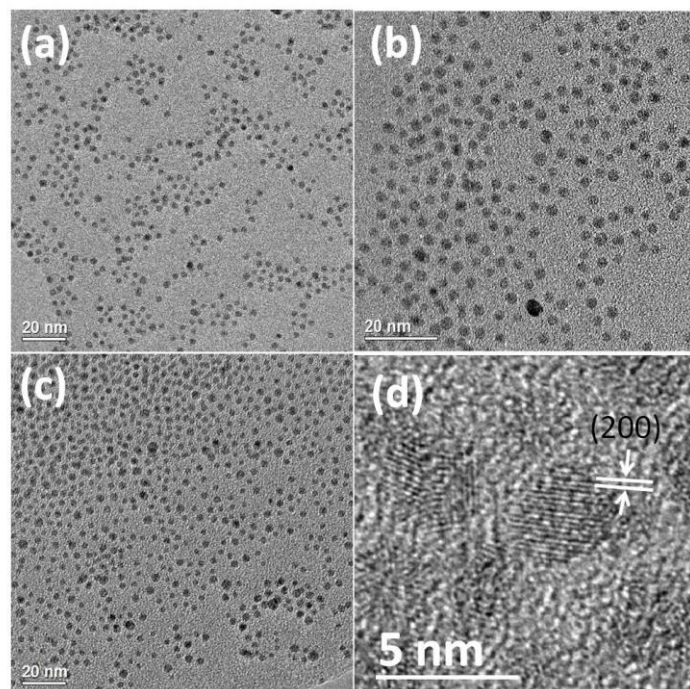


Figure 3.20 TEM images of CuPd nanospheres synthesized with (a) amine: acid = 1: 1, (b) amine: acid = 2: 1 and, (c) amine: acid = 3: 2. (d) HRTEM image of CuPd particles prepared with amine: acid = 1: 1 showing lattice fringes which index to the (200) planes of CuPd.

In standard synthesis, the molar ratio of metal precursor: amine: acid = 1: 9: 9, denoted by amine: acid = 1: 1. Increasing the amount of amine to a ratio of amine: acid = 2: 1 (**Figure 3.20b**), or increasing both capping agents to amine: acid = 3: 2 (**Figure 3.20c**), did not change the morphology of the product.

From previous TGA results of trimetallic CuPdPt nanospheres, we know the ligand adsorption ability of Pd is weaker than that of Pt. Therefore, it can be deduced that the adsorption of amine and acid on the CuPd surface is less than those on CuPt nanorods. Increasing the concentration of capping agents has little effect on increasing the surface ligand density. The situation of CuPd nanospheres is analogous to CuPt nanospheres prepared with half concentration of capping agents as discussed previously.

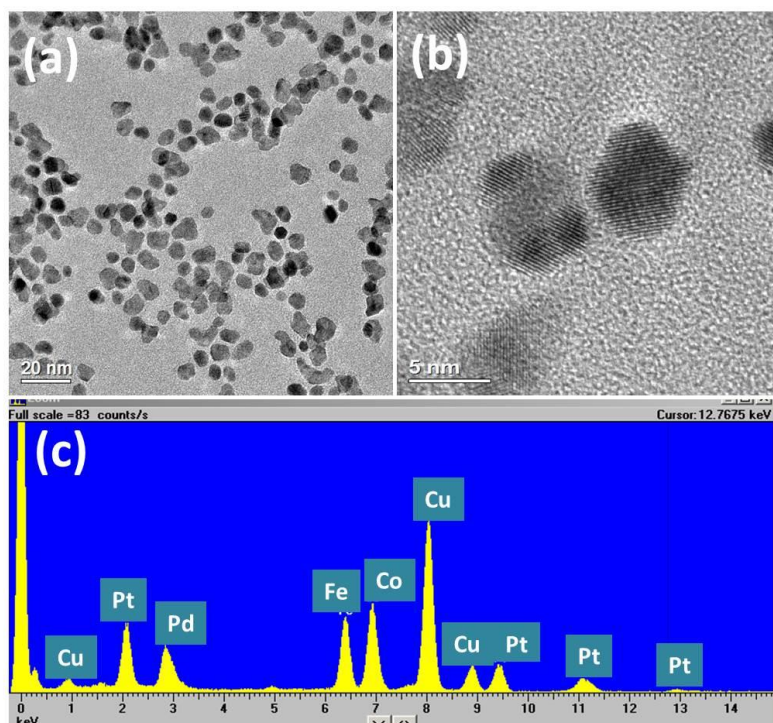


Figure 3.21(a) TEM image showing PdPt nanoparticles with irregular shapes; (b) HRTEM image and (c) EDX results of PdPt nanoparticles.

PdPt nanoparticles with irregular shapes were produced in combination of $\text{Pt}(\text{acac})_2$ and $\text{Pd}(\text{acac})_2$ precursors, as shown in **Figure 3.21**. These nanoparticles were highly crystalline. The rugged edges and polycrystallinity of some larger particles indicate that they are formed

by attachment of smaller particles. Due to the similarity of unit cell of Pt and Pd, it's not easy to examine whether the product is alloy by measuring lattice *d*-spacings or by analyzing the XRD pattern. To confirm the existence of both metals, EDX analysis in **Figure 3.21c** was carried out. Indeed, both peaks of Pd and Pt were detected. Other Cu, Fe and Co peaks came from the grid and column contamination, which exists in all EDX results examined by EDX equipped on TEM. Current experimental conditions are not ideal to control the shape of PdPt nanoparticles. The irregularity of the nanoparticles may be attributed to the weak interaction of ligands with the PdPt surface as well as the high diffusion efficiency of Pt atoms.

3.3 Solvent effect

Surface ligands play an important part in shape control during synthesis, as discussed in the above sections. Other than changing surface ligands themselves, varying external conditions can also have strong influences. By using different solvents, interactions of surface ligands can be tuned indirectly. For example, if the surface ligands are hydrophobic, using a polar solvent will weaken the interaction between them yet enhance that between ligands and nanoparticles. Consequently, nanoparticles are better protected and the effect of surface ligands becomes significant. In the following discussions, several examples are demonstrated on controlling morphology of nanomaterials through solvent effect.

3.3.1 Experimental section

Synthesis of trimetallic CuPdPt nanospheres

CuPdPt nanospheres were prepared with the same method described in section 3.2.1. For CuPdPt nanospheres prepared with octadecene (ODE), all the experiment parameters remain the same except ODE was used as solvent instead of diphenyl ether (DE).

Synthesis of Pt nanoparticles

Synthesis of hexagonal Pt nanoparticles

20 mg of Pt(acac)₂, 10 mg of polyvinylpyrrolidone (PVP), 218 mg of hexadecyltrimethyl-ammonium bromide (CTAB) were mixed together with 5.0 mL of ethylene glycol(EG) in a round-bottom flask equipped with a condenser. The mixture was heated to 200 °C for different reaction times. The particles were isolated by precipitating the colloids from the reaction system using a sufficient amount of acetone followed by centrifugation.

Synthesis of branched Pt nanowires

20 mg of Pt(acac)₂, 10 mg of PVP, 218 mg of CTAB and 35 mg of 1,2-decanediol were mixed in 5.0 mL of ODE. The mixture was heated to 120 °C until the solids were completely dissolved under stirring and further to 200 °C for reaction. The products were collected by centrifugation and washed several times with ethanol.

Synthesis of CuPd nanoparticles

CuPd nanowires can be prepared as following. 15 mg of Pd(acac)₂, 12.5 mg of CuSO₄ 5H₂O, 20 mg of PVP Mw = 55000 were dissolved in 5 mL of EG. Under vigorous stirring, the mixture was heated to 80 °C to produce a clear solution and further heated to 200 °C. After refluxing at 200 °C for 2 h, the mixture was cooled down to room temperature. The product was obtained by centrifugation and washed several times with ethanol.

CuPd nanospheres were prepared with 15 mg of Pd(acac)₂, 13 mg of Cu(acac)₂ and 20 mg of PVP with 35 mg of 1,2-decanediol as a reducing agent in 5 mL of 1-octadecene (ODE) under the same experimental conditions, in order to investigate the effect of solvent.

3.3.2 Solvent effect in the synthesis of CuPdPt nanospheres

Trimetallic CuPdPt nanospheres were prepared with a ratio of Cu: Pd: Pt = 1: 1: 1 in the presence of hexadecylamine, hexadecanoic acid and decanediol in either diphenyl ether (DE) or octadecene (ODE) solvent. It has been discussed in section 3.2.3 that uniform nanospheres were produced and can self-assemble to form superstructures, when DE was used in the synthesis. With all the other experimental parameters unchanged, ODE was used as a solvent instead of DE. Nanospheres with a broad size distribution were produced, and some pear-like shaped nanoparticles were also observed as shown in **Figure 3.22a**. A representative HRTEM image is displayed in **Figure 3.22b**, in which most nanospheres are polycrystalline. The nanoparticles can also assemble together, but in a disordered way (**Figure 3.22c**). This is because the produced nanospheres were not uniform, making it difficult to form an ordered assembly.

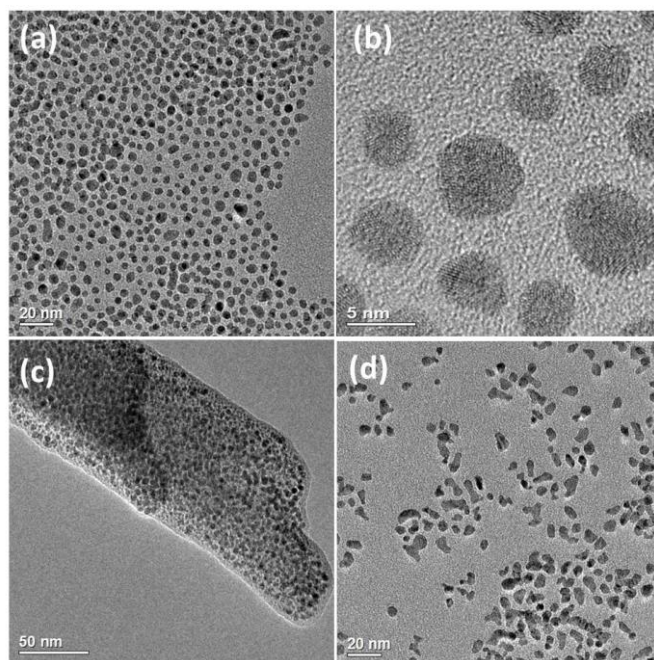
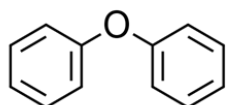
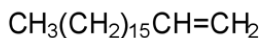


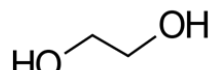
Figure 3.22 TEM images of CuPdPt nanoparticles synthesized in ODE solvent. Nanoparticles in (a-c) are produced with both amine and acid. Nanoparticles in (d) are produced with acid only.



diphenyl ether
1.05D



1-octadecene
0.47D



ethylene glycol
2.28D

Scheme 3.1 Different solvents and their corresponding dipole moments, unit in Debye.

If acid alone was used as a capping agent, nanoparticles with an even less regular shape are obtained (**Figure 3.22d**). When both amine and acid are applied, there is only a small amount ligands absorbed on CuPdPt surface (see TGA results in section 3.2.3). Using acid alone can further reduce the surface adsorption, as that the ligand layer is not dense enough to generate a good protective shell.

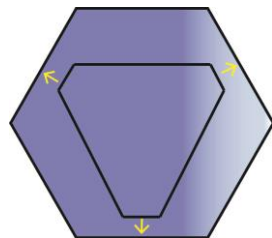
As we can see from the dipole moment in **Scheme 3.1**, DE (1.05D) is more polar than ODE (0.47D). Since the ligands used here are hexadecylamine and hexadecanoic acid, which are bound to the metal surface *via* terminal functionality. The alkyl tails exposed to solvent are hydrophobic. Therefore, the interaction between ligands and solvent in the case of DE is weak. In other words, the ligands are “repelled” to the metal surface, leading to enhanced interaction between ligands and metal surfaces. As a result, more uniform products were obtained in comparison with the ones prepared in ODE solvent.

3.3.3 Solvent effect in the synthesis of Pt nanoparticles

Similar solvent effect was also found in the synthesis of Pt nanoparticles. When EG was used as a solvent in the presence of CTAB and PVP, truncated triangular and hexagonal Pt nanoplates around 8 nm were produced after reaction for 2 h (see **Figure 3.23a**).

Extending the reaction time to 20 h, most triangular nanoplates disappeared and hexagonal plates became the main product, as shown in **Figure 3.23c**. This can be explained using the illustration in **Scheme 3.2**. The fast-growing edges are shortened in the final product,

forming a hexagonal shape. (111) planes are commonly observed in these nanoplates (**Figure 3.23e**).



Scheme 3.2 Shape evolution of Pt nanoplates. The slow growing edges (yellow arrows) elongate at the expense of fast growing ones.

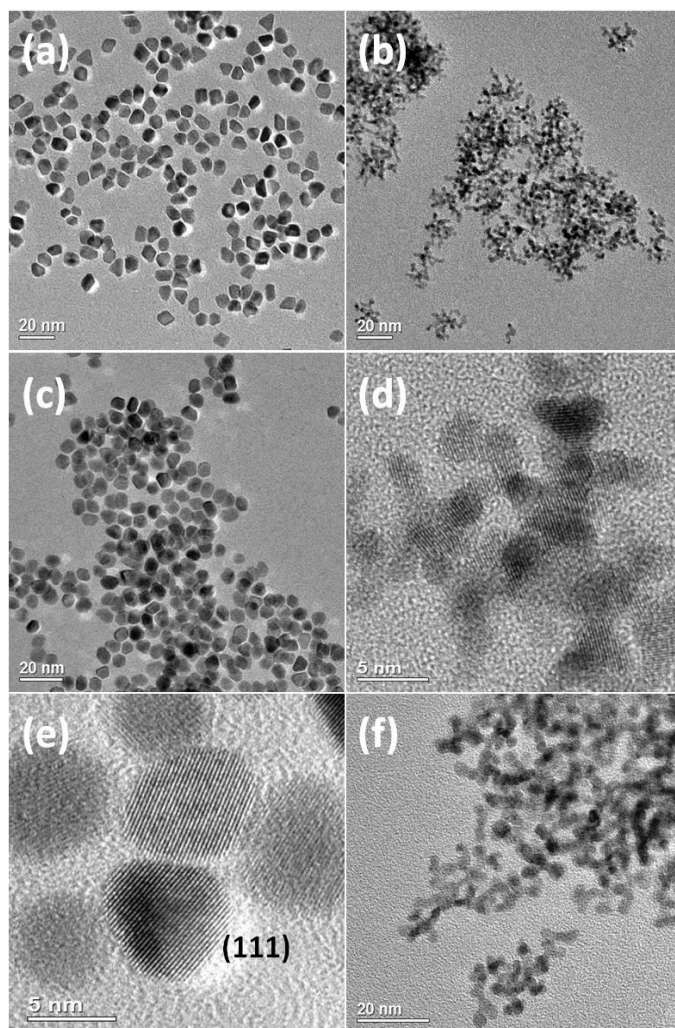
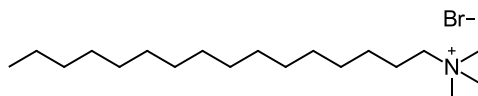


Figure 3.23 TEM images for Pt nanoparticles prepared in either (a, c, e) EG or (b, d, f) ODE. (a) Truncated triangular and hexagonal Pt nanoplates after 2 h; (c) hexagonal nanoplates after 20 h; (e) HRTEM image of Pt nanoplates with (111) planes parallel to the beam incidence direction; (b) TEM and (d) HRTEM images of Pt nanodendrites after 1 h; (f) Pt nanodendrites after reaction for 20 h.

A plate morphology is not favored thermodynamically.⁴⁰ Therefore, surface ligands play an important role in reducing the total surface energy and stabilizing the nanoplates. Synthesis with KBr replacing CTAB led to smaller nanospheres (~4 nm). This implies the effect of a long alkyl chain helps retain a plate shape. PVP helps to well disperse the nanoplates; aggregated products were obtained in the absence of PVP.

If the synthesis was conducted in a nonpolar solvent, ODE, Pt nanodendrites were produced (**Figure 3.23b**). The branched morphology remained the same even after reaction for 20 h (**Figure 3.23f**). From HRTEM images, it is found that the crystalline orientations of the branch units tend to be aligned in one dendrite particle. In **Figure 3.23d**, the lattice fringes can be indexed to (111) planes in each branch, and the nanocrystallites have a uniform orientation. By investigating the intermediates at 10 min, 20 min and 30 min, it is found that the dendrite morphology has formed at very early stage. The branched structure remains as reaction time is prolonged, with gradually increasing crystallinity.

The situation of Pt nanoplates and nanodendrites is very similar to that of CuPdPt nanospheres. We believe CTAB (see the chemical structure below) binds to the metal surface with its functional group and leaves the carbon chain tail exposed to the solvent. The tail is hydrophobic, thus EG as a polar solvent, can “push” the CTAB ligand onto metal surface, leading to formation of well-protected nanoplates.



When nonpolar solvent ODE was used, the interactions between ligands and metals were weakened. Branched structures were produced due to the weakening protection from surface ligands.

3.3.4 Solvent effect in synthesis of CuPd nanoparticles

The previous examples are both hydrophobic ligands. To further demonstrate the solvent effect, the case of PVP, a kind of hydrophilic polymer, is investigated in the synthesis of CuPd nanoparticles.

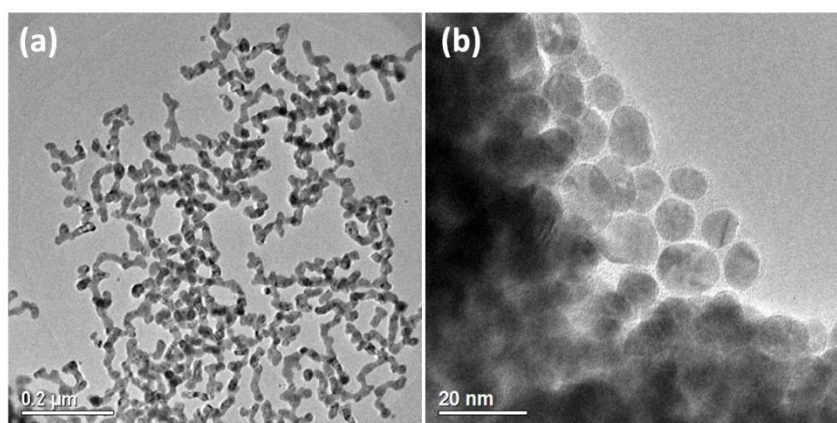


Figure 3.24 TEM images of CuPd nanoparticles capped with PVP, prepared in (a) EG and (b) ODE.

A TEM image of CuPd nanowires prepared in EG is displayed in **Figure 3.24a**. In comparison, nanospheres were produced when the solvent was changed to non-polar ODE (**Figure 3.24b**). These nanospheres are smaller in diameter. Detailed structure characterization of CuPd nanoparticles will be discussed in Chapter 5. Herein we mainly focus on the solvent effect on the morphology. Again, interactions between PVP and solvents will be weakened as polarity of solvents decreases. Thus, the interactions between surface ligands and metal are enhanced in a less polar solvent. In other words, the surfaces of CuPd nanoparticles are better protected by PVP in ODE, resulting in the formation of nanospheres instead of a branched structure.

The growth of nanoparticles is a complicated process, which can be affected by many factors. Solvent is one of them and may influence the morphology of nanoparticles in different ways. For example, epitaxial growth of Fe_3O_4 on Au seed is affected by polarity of the

solvent.⁴¹ The authors claimed that polar solvents can provide charges to compensate for the polarized plane at the Au- Fe₃O₄ interface. In this section, it is demonstrated that solvent can manipulate morphology control *via* changing interactions with ligands: metal surface can get strong protection by choosing combinations of hydrophilic ligands and non-polar solvents, and *vice versa*.

3.4 Implication of ligand-mediated growth mechanism

The present work has found it is the ligands bound to the surface that dominate the 1D growth of CuPt nanorods, in a manner of achieving a stable organization to minimize the energy. The proposed ligand-mediated growth mechanism highlights the influence of surface ligands in rod growth. When the rods grow linearly, then the side surfaces are flat, where parallel surface ligands could obtain strong mutual interactions in this stable configuration. When the density of ligands on surface decreases—caused by a low ligand concentration in solution, poor adsorption of ligands on metal surface, solvent effect and so on—interactions between ligands are weakened and nanocrystals with less regular shapes will form. This implies that when it comes to energy consideration in crystal growth, the energy of the crystal itself and the surface ligands should be taken in account as a whole.

Conventional theories believe the growth of crystal is determined by the crystal itself. The resulting crystal adopts a shape with minimum energy, usually bound with low index facets. The neglect of surface ligands in directing crystal growth can partially be attributed to the fact that ligands are invisible to most characterization techniques or are removed after purification in previous research. The effect of ligands is underestimated and simply regarded as physical template, or adsorbates that slow down the growth rate of certain facets. For the former, concentrated surfactant ligands were believed to form a micellar template to assist the crystal formation. But the surfactant template is soft and dynamic in the solvent, and unlikely to behave as stable assemblies during the reaction.⁴² Current research community commonly

regards surface ligands as adsorbates that affect the surface energy of facets. For instance, calculations using density functional theory (DFT) suggest that oleic acid ($C_{17}H_{33}COOH$), a widely used surface ligands, binds more strongly to the PbSe $\{111\}$ than to the $\{100\}$ planes, which can reverse the surface energy (PbSe bare surface $\gamma_{100} = 11.4$ and $\gamma_{111} = 20.4 \text{ meV}/\text{\AA}^2$) and finally alter the equilibrium shape from cubic to octahedral.⁴³

Our CuPt nanorods, however, were polycrystalline and built up by nanospheres with no well-defined facets. Thus, the selective adsorption of ligands to different facets is not significant in the nanorods. Our novel ligand-mediated mechanism indicates the importance of ligand-ligand interactions, which are neglected in the DFT calculation mentioned above.⁴³

This mechanism can be applied to explain the reported rod growth phenomena. For example, Au nanorods were prepared in the presence of hexadecyl-trimethyl-ammonium bromide (CTAB), and it was found that increasing CTAB concentration can enhance the yield of rods.⁴⁴ The authors suspected concentrated CTAB can form a longer micellar rod template. In another report, FePt nanorods were formed by collisions of nanospheres. It was observed *in situ* by real time TEM and found that winding rods become straight after adding more surfactant (additional 10 % oleic acid).⁴⁵ The authors believed the straightening is caused by eliminating crystal defects and minimizing surface areas, but did not point out why the concentration of surfactants affected the straightening process. Both examples are rather consistent with our ligand-mediated mechanism. Concentrated surface ligands in solution can increase its density on the rod surface, and ligands tend to be parallel to each other. In this stable organization, the mutual interactions of ligands are enhanced, which can further reduce the total energy of the ligand-capped rods.

With limited knowledge in theoretical chemistry, calculations on the degree of interactions between the ligands in different configurations are not accomplished in the current work. Future studies should explore a theoretical model of such ligand-interactions, which could better support our mechanism.

Findings in the present work demonstrate the effect of surface ligands in 1D growth of CuPt nanorods, and reveal that the well-known factors such as crystallographic orientations, specific facet blockings do not dominate the 1D growth in current situations. This is the first time that a ligand-mediated mechanism is proposed for the growth of 1D alloyed nanomaterial, which emphasizes the importance of mutual interactions between ligands. 108Our work offers a new perspective and provides practical knowledge for crystal growth process.

References

1. Y. Xia, P. Yang, Y. Sun, Y. Wu, B. Mayers, B. Gates, Y. Yin, F. Kim and H. Yan, *Adv. Mater.*, 2003, **15**, 353-389.
2. H. Yan, H. S. Choe, S. W. Nam, Y. J. Hu, S. Das, J. F. Klemic, J. C. Ellenbogen and C. M. Lieber, *Nature*, 2011, **470**, 240-244.
3. F. Patolsky and C. M. Lieber, *Mater. Today*, 2005, **8**, 20-28.
4. Z. Su, C. Dickinson, Y. Wan, Z. Wang, Y. Wang, J. Sha and W. Zhou, *CrystEngComm*, 2010, **12**, 2793-2798.
5. E. C. Walter, B. J. Murray, F. Favier, G. Kaltenpoth, M. Grunze and R. M. Penner, *J. Phys. Chem. B*, 2002, **106**, 11407-11411.
6. C. J. Murphy, T. K. San, A. M. Gole, C. J. Orendorff, J. X. Gao, L. Gou, S. E. Hunyadi and T. Li, *J. Phys. Chem. B*, 2005, **109**, 13857-13870.
7. R. L. Penn and J. F. Banfield, *Science*, 1998, **281**, 969-971.
8. J. F. Banfield, S. A. Welch, H. Z. Zhang, T. T. Ebert and R. L. Penn, *Science*, 2000, **289**, 751-754.
9. J. Polleux, N. Pinna, M. Antonietti and M. Niederberger, *Adv. Mater.*, 2004, **16**, 436-439.
10. A. Halder and N. Ravishankar, *Adv. Mater.*, 2007, **19**, 1854-1858.
11. Z. Tang, N. A. Kotov and M. Giersig, *Science*, 2002, **297**, 237-240.
12. K. S. Cho, D. V. Talapin, W. Gaschler and C. B. Murray, *J. Am. Chem. Soc.*, 2005, **127**, 7140-7147.
13. G. Zhu, S. Zhang, Z. Xu, J. Ma and X. Shen, *J. Am. Chem. Soc.*, 2011, **133**, 15605-15612.

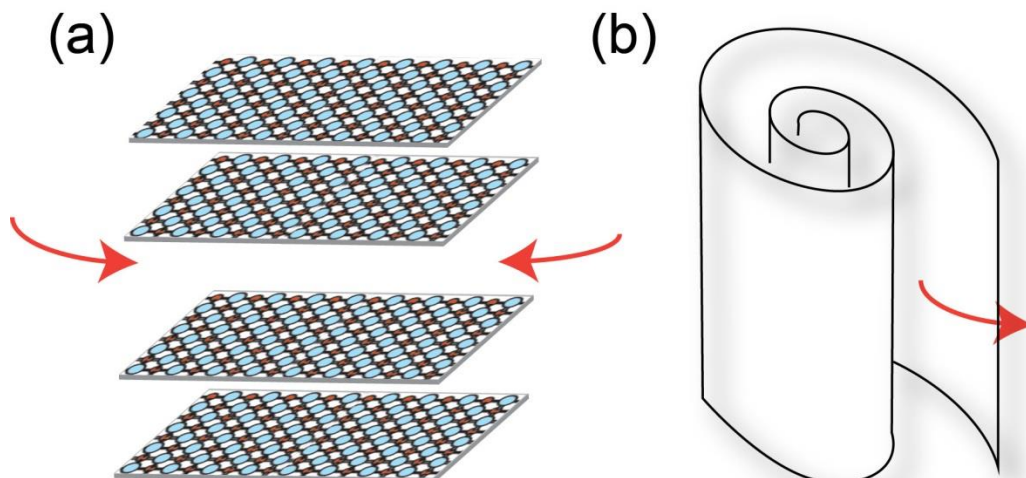
14. Q. S. Liu, Z. Yan, N. L. Henderson, J. C. Bauer, D. W. Goodman, J. D. Batteas and R. E. Schaak, *J. Am. Chem. Soc.*, 2009, **131**, 5720-5721.
15. X. Xu, G. Liu, C. Randorn and J. T. S. Irvine, *Int. J. Hydrog. Energy*, 2011, **36**, 13501-13507.
16. X. Xu, A. K. Azad and J. T. S. Irvine, *Catal. Today*, 2013, **199**, 22-26.
17. A. Dhirani, M. A. Hines, A. J. Fisher, O. Ismail, and P. Guyot-Sionnest, *Langmuir* 1995, **11**, 2609-2614.
18. S. Chen, S. V. Jenkins, J. Tao, Y. Zhu and J. Chen, *J. Phys. Chem. C*, 2013, **117**, 8924-8932.
19. X. G. Peng, J. Wickham and A. P. Alivisatos, *J. Am. Chem. Soc.*, 1998, **120**, 5343-5344.
20. F. Dumestre, B. Chaudret, C. Amiens, M. C. Fromen, M. J. Casanove, P. Renaud and P. Zurcher, *Angew. Chem. Int. Ed.*, 2002, **41**, 4286-4289.
21. T. Kwon, M. Min, H. Lee and B. J. Kim, *J. Mater. Chem.*, 2011, **21**, 11956-11960.
22. L. C. Ciacchi, W. Pompe and A. De Vita, *J. Am. Chem. Soc.*, 2001, **123**, 7371-7380.
23. L. C. Ciacchi, W. Pompe and A. De Vita, *J. Phys. Chem. B*, 2003, **107**, 1755-1764.
24. Z. M. Peng, H. J. You and H. Yang, *Acs Nano*, 2010, **4**, 1501-1510.
25. E. V. Shevchenko, D. V. Talapin, H. Schnablegger, A. Kornowski, O. Festin, P. Svedlindh, M. Haase and H. Weller, *J. Am. Chem. Soc.*, 2003, **125**, 9090-9101.
26. P. A. Rupar, L. Chabanne, M. A. Winnik and I. Manners, *Science*, 2012, **337**, 559-562.
27. M. L. S. Albuquerque, I. Guedes, R. Alcantara and S. G. C. Moreira, *Vib. Spectrosc.*, 2003, **33**, 127-131.
28. J. M. Serratos, W. D. Johns and A. Shimoyama, *Clay. Clay Miner.*, 1970, **18**, 107-113.
29. A. H. M. Sondag and M. C. Raas, *J Chem Phys*, 1989, **91**, 4926-4931.
30. T. Mishra, R. K. Sahu, S. H. Lim, L. G. Salamanca-Riba and S. Bhattacharjee, *Mater. Chem. Phys.*, 2010, **123**, 540-545.
31. M. V. Smoluchowski, *Phys. Chem.*, 1917, **92**, 129-168.
32. J. Zhang, Y. Wang, J. Zheng, F. Huang, D. Chen, Y. Lan, G. Ren, Z. Lin and C. Wang, *J. Phys. Chem. B*, 2007, **111**, 1449-1454.
33. E. M. Hendriks and M. H. Ernst, *J. Colloid Interface Sci.*, 1984, **97**, 176-194.
34. J. Zhang, F. Huang and Z. Lin, *Nanoscale*, 2010, **2**, 18-34.
35. J. A. Edgar, A. M. McDonagh and M. B. Cortie, *Acs Nano*, 2012, **6**, 1116-1125.

36. A. Kudo and Y. Miseki, *Chem. Soc. Rev.*, 2009, **38**, 253-278.
37. D. R. Lide, *CRC handbook of chemistry and physics*, 89th edition, CRC Press, 2008.
38. S. Zhou, B. Varughese, B. Eichhorn, G. Jackson and K. McIlwrath, *Angew. Chem. Int. Ed.*, 2005, **44**, 4539-4543.
39. A. K. Sinha, *Physical Metallurgy Handbook*, McGRAW-HILL, New York, 2003.
40. Y. N. Xia, Y. J. Xiong, B. Lim and S. E. Skrabalak, *Angew. Chem. Int. Ed.*, 2009, **48**, 60-103.
41. H. Yu, M. Chen, P. M. Rice, S. X. Wang, R. L. White and S. H. Sun, *Nano Lett.*, 2005, **5**, 379-382.
42. A. R. Tao, S. Habas and P. D. Yang, *Small*, 2008, **4**, 310-325.
43. C. R. Bealing, W. J. Baumgardner, J. J. Choi, T. Hanrath and R. G. Hennig, *Acs Nano*, 2012, **6**, 2118-2127.
44. N. R. Jana, L. Gearheart and C. J. Murphy, *J. Phys. Chem. B*, 2001, **105**, 4065-4067.
45. H. G. Liao, L. K. Cui, S. Whitelam and H. M. Zheng, *Science*, 2012, **336**, 1011-1014.

Chapter 4 Ligand Assisted Formation of Nanosheets Unrolled from Titanate Nanotubes

4.1 Introduction

Titanate nanomaterials have excellent catalytic and photo-electronic properties¹ and have been applied in a wide range of fields such as lithium batteries, solar cell and various catalytic reactions.^{2, 3} Many structures have been developed: nanotubes, nanospheres, nanodisks, to name a few. Among them, two dimensional nanosheets, as a new class of nanomaterials, possess intriguing properties owing to their high anisotropic feature with ultrathin thickness. For instance, it is reported that quasi- TiO₂ nanosheets display an optical adsorption peak that is significantly blue shifted, compared to bulk TiO₂.⁴



Scheme 4.1 Illustration of nanosheets produced from (a) exfoliation of layered compounds that could be several layers and (b) unrolling of nanotubes that produces single-layer nanosheet.

Conventionally, titanate nanosheets have been prepared by exfoliation of layered titanate crystals. Precursor titanate crystals are prepared by calcination of alkali carbonate and a titanium compound.^{5, 6} The resulting nanosheets, however, are usually not uniform in size,

because precursor crystals exhibit various shapes. Furthermore, exfoliation cannot guarantee the thickness of produced titanate nanosheets, which could have several layers as well as various thickness in different products (see **Scheme 4.1**).

Herein, we conceive to synthesize monolayer titanate nanosheets by unrolling titanate nanotubes. In contrast to exfoliation from layered compounds, nanosheets unrolled from titanate nanotubes are ensured to be monolayer (see **Scheme 4.1**). In chapter 3, the effect of ligands on morphology of metal nanoparticles has been discussed. It is envisioned that introducing ligands into nanotubes can unroll and stabilize them to form nanosheets. In the following work, titanate nanotubes are prepared and unrolled under different experimental conditions. The structure of unrolled nanosheets is studied by HRTEM characterization.

4.2 Experimental section

Synthesis of titanate nanotubes

Titanate nanotubes were prepared by a previously reported method.⁷ 0.1 mol of TiO₂ (rutile) was added into 25 mL of 10 M NaOH solution. After stirring for 30 min, the slurry was transferred to a Teflon autoclave. The autoclave was sealed and then thermally treated at 130 °C in oven for 3 days. The solid product was scraped out, washed with water and collected by centrifugation. The washing step was repeated several times using water to reach a pH of 12. To reach a pH value near 7, the as-prepared product was first stirred in dilute acid (0.1 M HCl) for 30 min and then centrifuged, followed by washing with water for several times. The sample was dried at 70 °C in an oven overnight.

Unrolling nanotubes into nanosheets

25 mg of titanate nanotubes was added into the mixture of ligands and 20 mL solvent, and then reacted under gentle stirring. Hexadecylamine (C₁₆H₃₃-NH₂), octylamine (C₈H₁₇-NH₂), tetrabutylammonium hydroxide (TBAOH), gum arabic and triethylamine (Et₃N) were

used as surface ligands. The detailed experimental conditions are summarized in **Table 4.1**. Ultrasonication was carried out in UW ultrawave sonicator U300 at 50W, 44 kHz. The product was collected by centrifugation and washed with ethanol.

Table 4.1 Experimental conditions of unrolling titanate nanotubes.

	Ligand/solvent	Concentration	Temperature	Reaction time
1	C ₁₆ H ₃₃ -NH ₂ / cyclohexane	0.1M	Room temp.	4d/ 1month
2	C ₁₆ H ₃₃ -NH ₂ / ethanol	0.1M	Room temp.	4d
3	Ethanol (200 mL)	--	Room temp.	4d
4	C ₈ H ₁₇ -NH ₂ / cyclohexane	0.1M	50 °C	4d
5	C ₈ H ₁₇ -NH ₂ / cyclohexane	3M	50 °C	4d
6	TBAOH/ water	0.1M	Room temp.	4d/ 1 month
7	TBAOH/ water	0.5M	50 °C	4d
8	Et ₃ N	--	50 °C	4d
9	C ₁₆ H ₃₃ -NH ₂ / cyclohexane	0.1M	ultrasonication	2h/ 8h
10	Gum arabic/ water	5 wt %	ultrasonication	2h/ 8h

Characterization

Transmission electron microscopy (TEM), and high resolution TEM (HRTEM) images were obtained on a JEOL-2011 electron microscope operating at 200 kV equipped with an Oxford Link ISIS system for energy-dispersive X-ray spectroscopy (EDX). Powder X-ray

diffraction (XRD) was performed on a PANalytical Empyrean diffractometer with Cu K α radiation.

4.3 Titanate nanotubes

Titanate nanotubes were obtained *via* the hydrothermal treatment of TiO₂ and NaOH solution.⁷ The product was washed with deionized water several times to reach a pH value of 12. After this stage, washing with water has little effect on further lowering the pH value. In order to reach a pH value near 7, the sample was stirred in a dilute acid solution, followed by washing several times with deionized water.

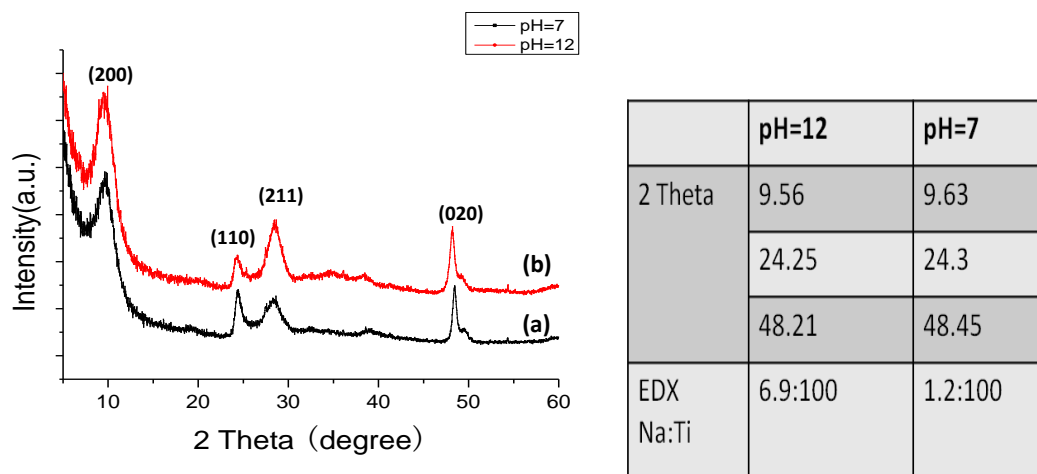


Figure 4.1 XRD patterns of titanate nanotubes with (a) pH = 7 and (b) pH = 12. Table on the right lists the EDX results and 2-Theta peak positions of the two samples.

The XRD patterns of the nanotubes washed to pH 7 and 12 are displayed in **Figure 4.1**, which are consistent with the reported structures of H₂Ti₃O₇ nanotubes.⁸ Small differences can be observed between samples with pH value of 7 and 12. For the sample with pH of 12, the content of Na is higher, and the positions of the XRD peaks are slightly shifted to low angles. This indicates that *d*-spacings of the high pH value sample are slightly larger, which is probably caused by the existence of Na ions. Water can wash away the excess NaOH in the

beginning, but as the NaOH residue is rinsed off, continuing washing won't change the pH much. At this stage, Na ions in the structure need to be exchanged by protons.⁹ Diluted acid can facilitate this process and result in a product with lower pH value.

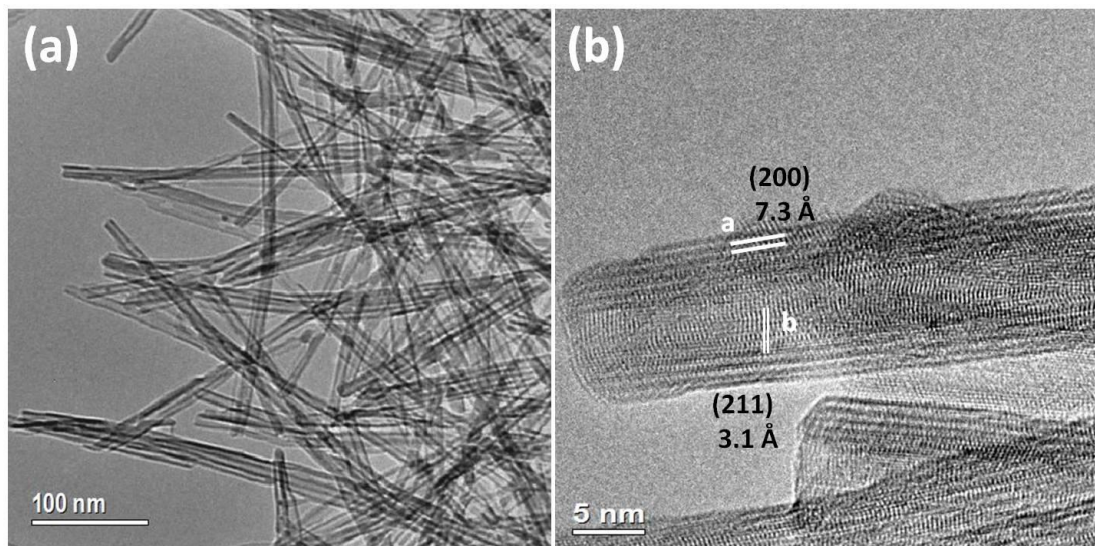


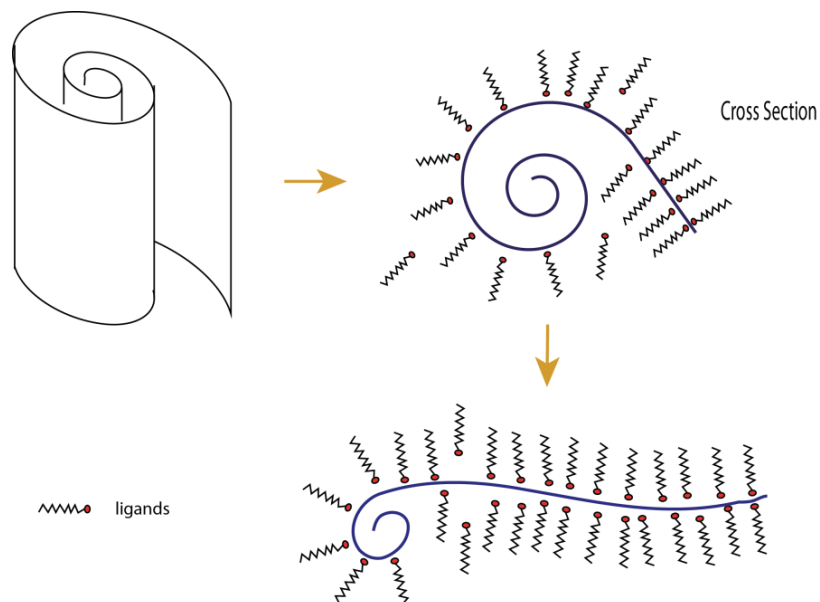
Figure 4.2 (a) Low magnification TEM image of titanate nanotubes and (b) HRTEM image of a nanotube with 5 layers in the wall.

The morphology of nanotubes was examined by TEM and a typical image is shown in **Figure 4.2a**. No obvious difference was observed between samples with pH = 7 and 12. Scroll-shaped nanotubes were as long as several hundred nanometers and ~10 nm wide, usually with 4–6 layers in the wall. The structure of H₂Ti₃O₇ nanotubes has been investigated⁸ to be monoclinic with unit cell parameters $a = 1.603$, $b = 0.375$, $c = 0.919$ nm and $\beta = 101.45^\circ$. In HRTEM image **Figure 4.2b**, the inter-layer distance in the tube wall is ~7.3 Å which corresponds to (200) planes. Notably, it is smaller than the value of 9.1 Å calculated from (200) peak at $2\theta = 9.6^\circ$ in the XRD. It has been studied that H atoms are located in the interlayer space and the “walls” are composed of Ti₃O₇²⁻ ions. The increase of (200) interplane distance could be caused by insertion of H₂O molecules, which are stable under XRD but not in TEM. The loss of H₂O under the high energy electron beam will result in the shrinkage of the d -spacing back to the normal H₂Ti₃O₇ value. Li and co-workers⁹ reported that (200) peak of titanate nanotubes shifted to $2\theta = 11^\circ$ (corresponding $d = 7.8$ Å) after calcination at 550 °C,

confirming our assumption. The fringes marked by “*b*” are parallel to the tube surface and a bit distorted, with a *d*-spacing of 3.1Å, corresponding to (211) planes.

4.4 Unrolling nanotubes into nanosheets

Titanate nanotubes can be regarded as rolls of $\text{H}_2\text{Ti}_3\text{O}_7$ nanosheets. Once these scroll-like nanotubes are unrolled, monolayer Ti nanosheets, similar to graphene, can be obtained, which have intriguing properties. As discussed in chapter 3, interactions between ligands and a surface can have strong effects on nanostructures. To access such a monolayer structure, we envisioned an approach that introducing ligands into the layers to unroll the nanotubes. At first, the outermost layer will expand, leading to an exposed inner part of the tubes. As illustrated in **Scheme 4.2**, with more and more adsorption of ligands, the nanotubes will be gradually unrolled into nanosheets, stabilized by surface ligands. Once the nanosheets are formed and capped with ligands on the surface, it will be difficult to roll them back into tubes.



Scheme 4.2 Proposed formation of nanosheet unrolled from nanotubes with the help of surface ligands. The cross section view demonstrates the insertion of ligands into interlayer spaces.

To test the feasibility of this approach, linear ligands (such as hexadecylamine) and bulky ligands (TBAOH, Et₃N) were both studied. Different solvents and ultrasonic synthesis were investigated to optimize the unrolling process.

4.4.1 Unrolling tubes with primary amine ligands

Nanotubes were treated with hexadecylamine (C₁₆-NH₂) in cyclohexane at room temperature under gentle stirring. The amine ligands are in excess, with a molar ratio of ligand: H₂Ti₃O₇ = 20: 1. After 5 days, some nanosheets formed, as shown in **Figure 4.3**. A number of tubes, however, remained rolled in the product. Some nanosheets are located beneath the tubes or buried under tubes (**Figure 4.3c**). At the edges of the sample, a very thin nanosheet can be observed (**Figure 4.3a**). Since the unrolled sheets are monolayer, they could be very fragile and the contrast is rather low. The ragged edges of the nanosheet are probably caused by damage.

In HRTEM image **Figure 4.3b**, orthogonal fringes with *d*-spacings of 3.50 Å and 2.70 Å are observed, which are discontinuous. The H₂Ti₃O₇ unit cell (*b* = 0.375, *c* = 0.919 nm) illustrated in **Figure 4.4**, shows it is constructed by edge-sharing Ti-O octahedrons. After unrolling, the *a* axis disappears and a two dimensional sheet is formed which originates from the (100) planes. We will use (*k l*), two miller indices, to denote planes on the 2D nanosheet. In the newly formed 2D structure, an inter-fringe spacing of 3.50 Å can be attributed to that of (10) planes (*d*₁₀ = 3.75 Å). While 2.70 Å can be attributed to that of (03) planes (*d*₀₃ = 3.06 Å). This is reasonable considering that *c* consists of 3 Ti octahedrons. Obviously, these two planes are orthogonal. The derivation of the *d*-spacing may be caused by defects and distortion. In **Figure 4.3d**, “ridges” can be observed in the unrolled nanosheet. These are where the “walls” were and therefore a feature of the original tube. Furthermore, orthogonal fringes were also found on the flat sheet, indicating it is the (100) plane.

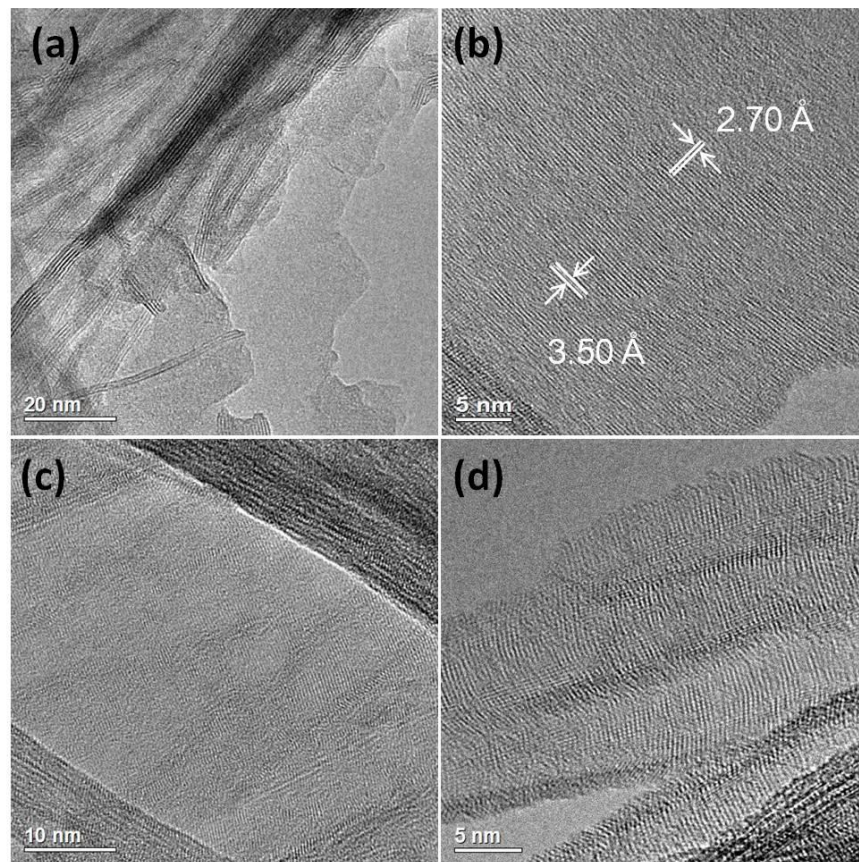


Figure 4.3 TEM images of $\text{C}_{16}\text{H}_{33}\text{-NH}_2$ unrolled nanosheets. (a) Low magnification image showing ultrathin nanosheets at the edges. HRTEM images of (b) flat nanosheet with orthogonal d -spacings of 3.50 Å and 2.70 Å; (c) nanosheet beneath nanotubes and (d) unrolled nanosheet with traces of original tubular shape.

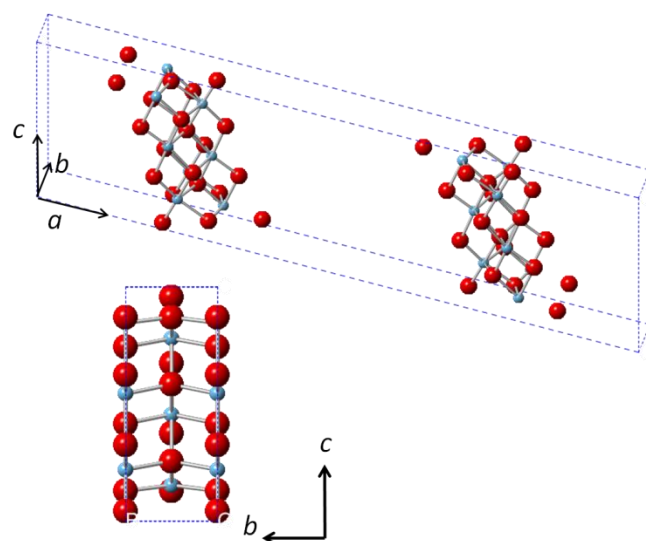


Figure 4.4 Unit cell of $\text{H}_2\text{Ti}_3\text{O}_7$ and structure viewed from [100] direction. Blue spheres represent Ti and red spheres represent O atoms.

Changing the solvent to a protic solvent, ethanol, leads to degradation of the unrolling. Although some nanosheets were still produced, the amount is significantly reduced. This implies that C₁₆-NH₂ ligands are probably bound to the titanate surface by uniting amine and the protons located in the layers. Ethanol may compete to seize the C₁₆-NH₂ ligands and turn them into protonated ammonium, weakening the interaction between ligands and nanotubes. In comparison, cyclohexane is aprotic, thus it facilitates ligands uniting with protons in nanotubes and further unrolling tubes. To clarify that the unrolling process was induced by ligands, a blank experiment was carried out in ethanol solution in absence of C₁₆-NH₂. Nanotubes remained tubular after several days of stirring.

Using octylamine (C₈-NH₂) as the ligand led to a reduced number of nanosheets in the product, even at a higher temperature of 50 °C. Because the unrolling process depends on the inserted ligands, the longer the alkyl tails are, the stronger the interactions are between the surface ligands. As a result, nanosheets are less stabilized in the case of C₈-NH₂, which is very similar to the ligand effect in CuPt nanorods. Increasing the concentration of C₈-NH₂ has a minor effect on improving the nanosheet yield.

Extending the reaction time to one month can slightly increase the yield of nanosheets. Whereas, many nanotubes still existed and some were broken into several parts due to the long time stirring. More efforts are required to optimize this method in order to achieve fully unrolled products. We are able to conclude that nanotubes can be unrolled into nanosheets with the assistance of primary amine ligands, although optimization of the experimental conditions is required to improve efficiency.

4.4.2 Unrolling nanotubes with bulky ligands

We also attempted to unroll titanate nanotubes with the bulky ligand tetrabutylammonium hydroxide (TBAOH). It is conceived that OH⁻ will take away the protons within the tubes and TBA⁺ ions can take place at the same time. With the assistance of this

bulky ligand, the layers could be unrolled. Experimentally, nanotubes were partially unrolled after 4 days of stirring in TBAOH solution. Thin, flat pieces of nanosheets formed, as well as sheets with curled sides (see **Figure 4.5**). Nanotubes still existed in the product.

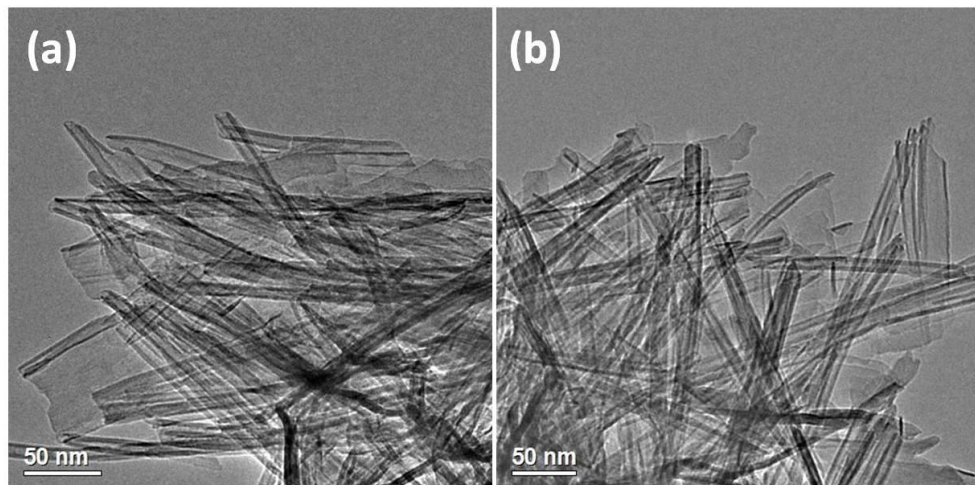


Figure 4.5 TEM images of nanotubes unrolled by TBAOH. Flat and curled sheets were formed in the product, though some nanotubes remained intact.

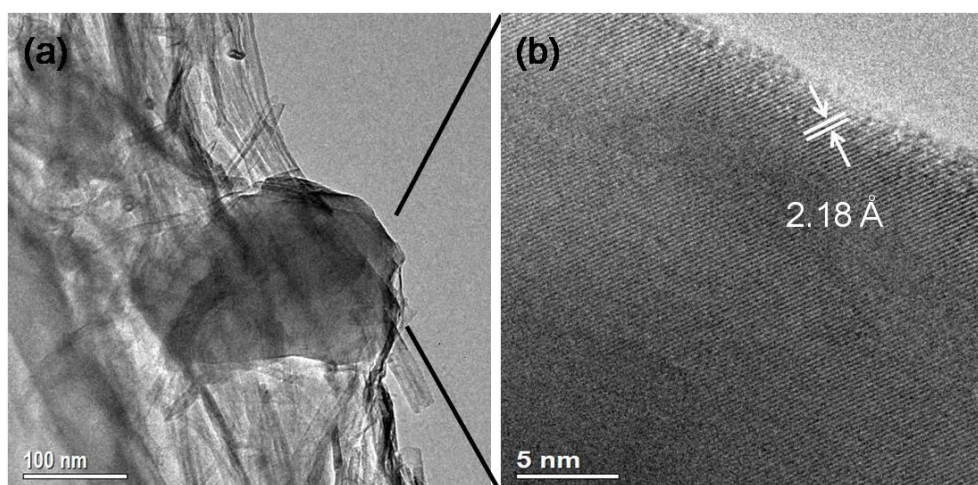
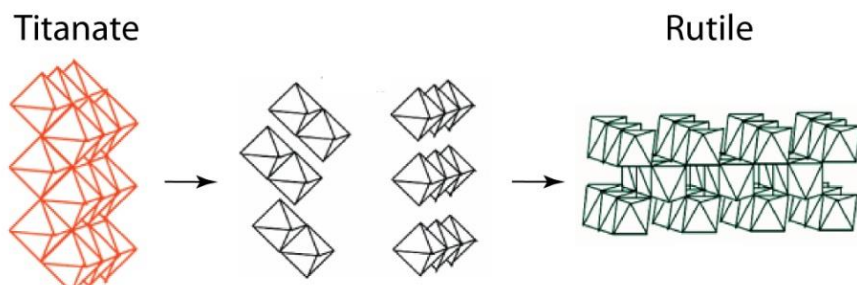


Figure 4.6 By-product formed in the unrolling experiment with TBAOH for 1 month. (a) Low magnification TEM image and (b) HRTEM image showing lattice fringes.

Increasing the reaction time to 1 month or increasing the concentration of TBAOH was not helpful to increase unrolling yield, yet can lead to a dehydrated byproduct. A typical image of the byproduct is given in **Figure 4.6**. Large crystalline particles formed with either a high concentration or long reaction time in the presence of TBAOH, and all the tubular structures

were totally destroyed. The HRTEM image in **Figure 4.6b** shows lattice fringes with a *d*-spacing of 2.18 Å, which does not match the *d*-spacing of any plane of $\text{H}_2\text{Ti}_3\text{O}_7$. It is more likely to be the (111) plane of rutile TiO_2 (JCPDS 00-087-0710, Tetragonal). The phase transition to rutile TiO_2 is likely due to dehydration of some titanate after a long reaction time or in high concentration solution. Transition from titanate nanofibers to rutile has been reported but in high concentration solution of HNO_3 .¹⁰

As for the byproduct, the tubular morphology was completely destroyed. The difference in crystal structure between titanate and rutile can provide an explanation for this morphology change. The structures are illustrated in **Scheme 4.3**. Both phases consist of edge-sharing octahedrons. The octahedrons share four edges in titanate, but share only two edges in rutile.¹¹ In rutile, these edge-sharing octahedrons form linear chains, which link together by sharing vertices to produce a three-dimensional lattice. The zigzag ribbons in the original titanate structure are separated into detached $\text{Ti}-\text{O}$ octahedrons or their clusters,¹⁰ to form these linear chains as a building unit for rutile. As a result, the rutile byproduct crystals have no morphological similarity to the original nanotubes.



Scheme 4.3 Illustration of crystal structures of titanate (left) and rutile (right) and a possible transition process.

Bulky ligand Et_3N was used as both a ligand and solvent to unroll nanotubes. In this experiment, 25 mg of titanate nanotubes was mixed with 20 mL Et_3N . Parts of the tubes were unrolled, whilst others remained tubular. This indicates that a high concentration of ligand cannot guarantee an improvement of the yield of nanosheets.

4.4.3 Unrolling with assistance of ultrasonication

Ultrasonication is reported to be able to assist isolation of carbon nanotubes from the bundles.¹² It is proposed that ultrasonication “frays” the end of the bundle and facilitates additional surfactant adsorption.¹³ An isolated, surfactant coated nanotube will be released in an unzipping way.

A series of experiments were carried out under ultrasonication (50W, 44 kHz) to unroll titanate tubes. In the presence of C₁₆-NH₂ in cyclohexane solvent, a few nanotubes were unrolled into nanosheets after 2 h ultrasonication. However, when the reaction time was extended to 8 h, most nanotubes were broken into shorter ones and some were deformed. There was no obvious increase of nanosheet formation, but the dehydrated product, the same as byproduct observed in the specimen unrolled by TBAOH (**Figure 4.6**), was also found.

Gum Arabic (GA) was used as the surface ligand in the ultrasonication-assisted experiment. GA is a kind of water soluble polysaccharide produced by Acacia Senegal trees. It is a complex mixture with highly branched structure containing glucuronic acid end units and a small portion of protein.¹⁴ Measurements reported an average molecular weight as large as ~200,000 g/mol. No nanotubes were unrolled by GA after 2 h ultrasonication. After 8 h, the nanotubes retained the tubular shape, with a small number of dehydrated byproduct. GA is too large to insert into the interlayers of nanotubes, which is consistent with our assumption.

Although ultrasonication is reported to be helpful for surfactant adsorption, it has little effect in unrolling titanate nanotubes under the current experimental conditions. Extending the reaction time will lead to formation of the byproduct, which might result from the combined contribution of alkaline conditions and increase of temperature caused by ultrasonication.

In summary, we have demonstrated the feasibility to unroll nanotubes with the assistance of ligands. It has been reported that the titanate tubes can maintain their structure up to calcination at 550 °C,⁹ and theoretical calculations have proposed that surface tension is the

principal driving force for tube formation.¹⁵ Therefore, transforming nanotubes into nanosheets is a process that increases the surface energy. By introducing surface ligands onto surface of the sheets, ligand-ligand interactions should be taken into account of the total surface energy. Thus nanosheets, an unstable structure, can be retained with ligands on them. Although this method still needs improvement, it has proven the function of ligand interaction in nanostructuring.

Within these limited experimental results, the best unrolling efficiency was achieved by C₁₆-NH₂ in the aprotic solvent of cyclohexane. C₈-NH₂ has a similar property as C₁₆-NH₂ ligand, but its shorter alkyl chain weakens the interaction between ligand molecules and results in a little decrease in unrolling yield. Bulky ligands didn't show better unrolling performance than primary ligands. Instead, a high concentration of TBAOH can lead to dehydration of some titanate tubes, resulting in the formation of the rutile byproduct. As polysaccharide gum arabic (GA) is too large to insert into the nanotube interlayers, it failed to unroll the nanotubes. Ultrasonication is not helpful in the current experimental condition; on the contrary it facilitates the formation of byproduct.

References

1. A. Riss, M. J. Elser, J. Bernardi and O. Diwald, *J. Am. Chem. Soc.*, 2009, **131**, 6198-6206.
2. D. V. Bavykin, J. M. Friedrich and F. C. Walsh, *Adv. Mater.*, 2006, **18**, 2807-2824.
3. L. Kavan, M. Kalbáč, M. Zukalová, I. Exnar, V. Lorenzen, R. Nesper and M. Graetzel, *Chem. Mater.*, 2004, **16**, 477-485.
4. T. Sasaki and M. Watanabe, *J. Phys. Chem. B*, 1997, **101**, 10159-10161.
5. T. Sasaki, Y. Ebina, Y. Kitami, M. Watanabe and T. Oikawa, *J. Phys. Chem. B*, 2001, **105**, 6116-6121.
6. T. Tanaka, Y. Ebina, K. Takada, K. Kurashima and T. Sasaki, *Chem. Mater.*, 2003, **15**, 3564-3568.
7. Q. Chen, W. Z. Zhou, G. H. Du and L. M. Peng, *Adv. Mater.*, 2002, **14**, 1208-1211.

8. Q. Chen, G. H. Du, S. Zhang and L. M. Peng, *Acta Crystallogr. B*, 2002, **58**, 587-593.
9. X. M. Sun and Y. D. Li, *Chem-Eur J*, 2003, **9**, 2229-2238.
10. H. Y. Zhu, Y. Lan, X. P. Gao, S. P. Ringer, Z. F. Zheng, D. Y. Song and J. C. Zhao, *J. Am. Chem. Soc.*, 2005, **127**, 6730-6736.
11. J. K. Burdett, T. Hughbanks, G. J. Miller, J. W. Richardson and J. V. Smith, *J. Am. Chem. Soc.*, 1987, **109**, 3639-3646.
12. R. Bandyopadhyaya, E. Nativ-Roth, O. Regev and R. Yerushalmi-Rozen, *Nano Lett.*, 2002, **2**, 25-28.
13. M. S. Strano, V. C. Moore, M. K. Miller, M. J. Allen, E. H. Haroz, C. Kittrell, R. H. Hauge and R. E. Smalley, *J. Nanosci. Nanotechno.*, 2003, **3**, 81-86.
14. L. Picton, I. Bataille and G. Muller, *Carbohyd. Polym.*, 2000, **42**, 23-31.
15. S. Zhang, L. M. Peng, Q. Chen, G. H. Du, G. Dawson and W. Z. Zhou, *Phys. Rev. Lett.*, 2003, **91**, 265103.

Chapter 5 One-step Synthesis and Shape-Control of CuPd Nanowire Networks

5.1 Introduction

The morphology of nanomaterials can strongly influence their intrinsic properties. Networks of metallic and alloyed branched nanowires possess promising advantages including high surface areas and a hierarchical structure, and have attracted considerable attention.¹⁻³ Many monometallic and bimetallic nanowire networks have been successfully synthesized so far. For example, Pt nanowire networks have been prepared with the assistance of a template, either a soft one in a two-phase water-chloroform system formed by cetyltrimethylammonium bromide,⁴ or a hard template of mesoporous silica.⁵ Pd polyhedron networks are prepared by introducing Cu²⁺ as foreign ion, which is critical for the network formation.⁶ CuAu nanowire networks were fabricated using ethylene glycol, diethylene glycol, triethylene glycol and glycerol as the solvent. If the solvent was replaced with tetraethylene glycol, discrete CuAu nanocrystals were produced.⁷ The authors speculated CuAu networks formed by coalescence of nanoparticles according to XRD and visible absorption spectra,⁷ but direct observation of the growth process was not presented in their work. PdAg and PdAuAg nanospikes were produced by adding a second or third metal salt sequentially into the solution containing Pd precursor during the reaction.⁸ Reports of a CuPd nanowire network are still rare.

CuPd nanomaterial is widely applied in a range of catalysis reactions, such as combustion of methane,⁹ hydrogen generation in photocatalysis¹⁰ and hydration of acrylonitrile.¹¹ Recently, CuPd catalyst has shown its potential in oxygen reduction reaction (ORR). Wang *et al.*¹² demonstrated the electrocatalytic activity of CuPd catalysts towards ORR. Based on experimental results and theoretical calculations,¹³ the best activity was obtained on CuPd sample with a composition of Cu: Pd = 1: 1. CuPd nanocubes are reported to have enhanced activity for ORR by Zhang and coworkers.¹⁴

In this chapter, a one-step method is demonstrated to prepare CuPd nanowire networks with interconnected, three dimensional structures. Intermediates during the reaction are examined by direct HRTEM observations to reveal the growth process. Effects of surface ligands are studied to achieve shape control and AgPd nanowires are prepared to test the versatility of this method. CuPd nanowires are also loaded on carbon nanoparticles as catalyst, and show morphology dependent performance towards ORR.

5.2 Experimental section

Synthesis of CuPd nanowires and nanoparticles

In a typical synthesis, 15 mg of palladium (II)-acetylacetone [Pd(acac)₂], 12.5 mg of CuSO₄ 5H₂O, 20 mg of polyvinylpyrrolidone (PVP Mw = 55000) were dissolved in 5 mL of ethylene glycol (EG). Under vigorous stirring, the mixture was heated to 80 °C to produce a clear solution and further heated to 200 °C. After refluxing at 200 °C for 2 h, the mixture was cooled down. The product was collected by centrifugation and washed several times with ethanol. Intermediate products were collected at 5 min and 10 min during heating to 200 °C to study the growth process.

To study the effect of the capping agent, the molecular weight of PVP was varied to 10,000 and 40,000 whilst a constant PVP weight of 20 mg and other parameters were unchanged. CuPd nanoparticles were prepared with 15 mg of Pd(acac)₂, 13 mg of Cu(acac)₂ and 20 mg of PVP with either 242 mg of formanilide or 35 mg of 1,2-decanediol added as a reducing agent in 1-octadecene (ODE) under the same experimental conditions, in order to investigate the effect of reducing agent and solvent.

Carbon-supported CuPd networks were prepared as follows. As-prepared CuPd nanowires were dispersed in ethanol by ultrasonication. Pre-weighed Super P carbon nanoparticles (Timcal, size ~40 nm, BET surface area ~60 m²/g) was added into the dispersion

and the mixture was ultrasonicated for 1 h followed by stirring overnight. The product was collected and treated at 400 °C in air for 4 h to remove PVP.

Synthesis of Pd-based nanoparticles

The synthetic procedures were the same as mentioned before except that different metal precursors were used (AgNO_3 , $\text{HAuCl}_4 \cdot 3\text{H}_2\text{O}$ and $\text{CoSO}_4 \cdot 7\text{H}_2\text{O}$).

AuCuPd nanowires were prepared with the following method. 30 mg of $\text{Pd}(\text{acac})_2$, 25 mg of $\text{CuSO}_4 \cdot 5\text{H}_2\text{O}$ and 60 mg of PVP Mw = 55000 were dissolved in 5 mL of EG. The mixture was heated to 80 °C under stirring to dissolve all reactants and further heated to 200 °C for reaction. After reaction for 10 min, 1 mL of EG solution containing 40 mg of $\text{HAuCl}_4 \cdot 3\text{H}_2\text{O}$ was added into the solution. After reaction for another 2 h, the flask was removed from the heating mantle and the product was collected with the same procedures stated before.

Porous AuCuPd nanowires were prepared by a galvanic replacement reaction. 0.5 mmol (8 mg) of as-prepared CuPd nanowires were dispersed in 20 mL of deionized water after ultrasonication for 10 min. Under vigorous stirring (1000 rpm), 5 mL of HAuCl_4 solution (6 mM) was added dropwise into the CuPd dispersion. The mixture solution was stirred for 16 h at room temperature to react thoroughly. The product was collected by centrifugation and washed several times with acetone.

Characterization

Transmission electron microscopy (TEM) and high resolution TEM (HRTEM) images were obtained on a JEOL-2011 electron microscope operating at 200 kV equipped with an Oxford Link ISIS system for energy-dispersive X-ray spectroscopy (EDX). Morphology of the CuPd network was examined by field-emission scanning electron microscopy (FESEM) on a JEOL JSM-6700F microscope operating at 2-5 kV equipped with an Oxford INCA system for EDX. Powder X-ray diffraction (XRD) was performed on a PANalytical Empyrean

diffractometer with Cu K_α radiation. Attenuated Total Reflection Fourier Transform Infrared (ATR-FTIR) was performed on Thermo Fisher NICOLET 6700 FT-IR spectrometer.

Electrochemical characterization

The electrochemical characterization was carried out by Mr Yuhui Chen at University of St Andrews. Inks were prepared by mixing the catalyst powder (1 mg/mL in isopropanol), 0.5 mL nafion solution (0.125 wt % solution in isopropanol) and 0.5 mL isopropanol. 3 µl of the ink was casted on a glassy carbon (GC) cylindrical electrode (diam. 3 mm). Electrochemical measurements were carried out with a VMP3 potentiostat (Biologic) at room temperature. A three-electrode cell was built with Pt counter electrode; Ag wire in 3M KCl saturated with AgCl as reference electrode and Pt electrode or GC electrodes loading with catalyst as working electrode. The ORR measurements were performed in O₂ saturated 0.5 M HClO₄ solution at a scan rate of 100 mV/s.

5.3 CuPd nanowire networks

CuPd nanowire networks were prepared in the presence of PVP in ethylene glycol. **Figure 5.1** shows TEM and SEM images of the networks. CuPd nanowires have an average width of 18.2 ± 2.2 nm. Their branched feature results in pores within the interconnected network structure. In the SEM image, a 3D porous structure can be observed in a large scale. An average Cu/Pd ratio of 58: 42 was obtained by examining ten randomly selected spots in EDX analysis and elemental mapping shows uniform distributions of Cu and Pd elements (see **Figure 5.1**).

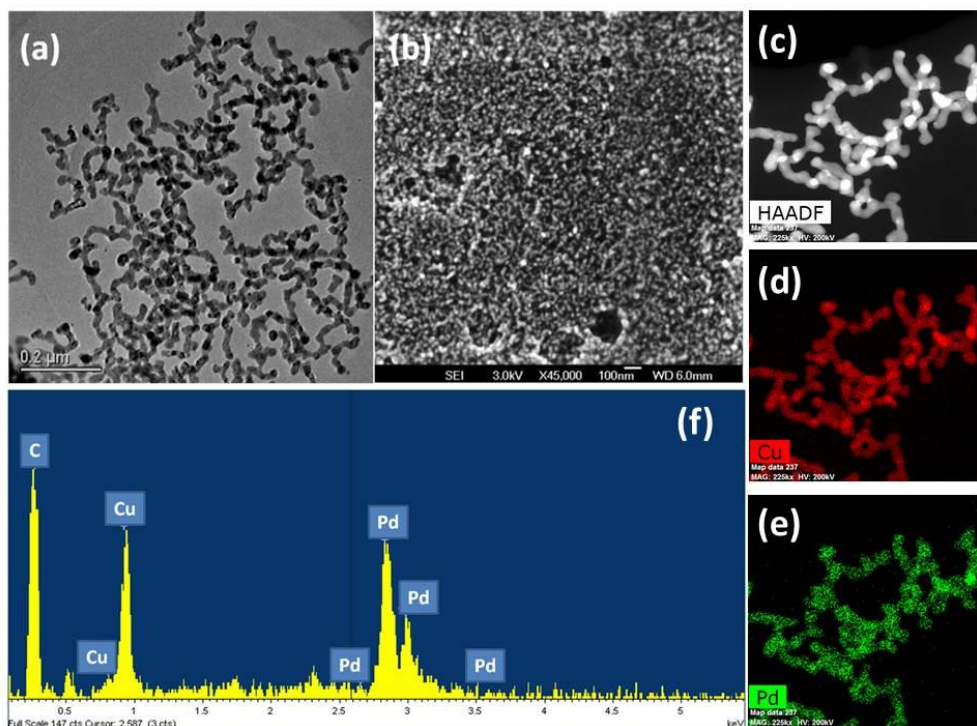


Figure 5.1 (a) TEM and (b) SEM images of CuPd nanowire networks after a reaction for 2 h. (c) HAADF image. Elemental mapping showing the (d) Cu and (e) Pd distribution. (f) A typical EDX spectrum of CuPd nanowires. The data in (c-e) were recorded by FEI company.

Normally both Cu and Pd are face-centered-cubic (fcc) structure, but the fcc and bcc (body-centered-cubic) structures coexist in the CuPd nanowires, according to XRD patterns presented in **Figure 5.2a**.

Upon HRTEM examination, the CuPd nanowires were found to be polycrystalline and consist of single crystalline domains and some defects (**Figure 5.3**). Both fcc and bcc structures are present in different areas within a single nanowire. In **Figure 5.3a**, fcc structure with a *d*-spacing of 2.17 Å was observed, corresponding to the (111) planes of CuPd. Bcc structure with *d*-spacings of 2.97 Å and 2.08 Å was located in the same branch, which can be assigned to the (100) and (110) planes respectively (**Figure 5.3b**).

Nearly pure fcc type CuPd nanoparticles were achieved using formanilide as reducing agent in the solvent ODE (**Figure 5.2b**).

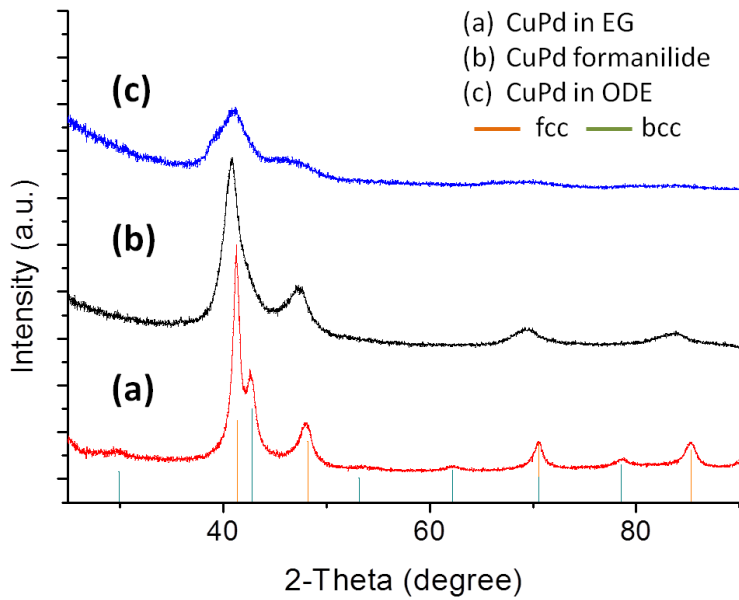


Figure 5.2 XRD patterns of (a) CuPd nanowire networks prepared in EG, (b) CuPd nanoparticles reduced by formanilide in ODE and (c) CuPd nanoparticles reduced by 1,2-decanediol in ODE. Yellow and green vertical lines indicate the position of alloyed CuPd fcc structure (JCPDS 00-048-1551) and bcc structure (JCPDS 01-078-4406), respectively.

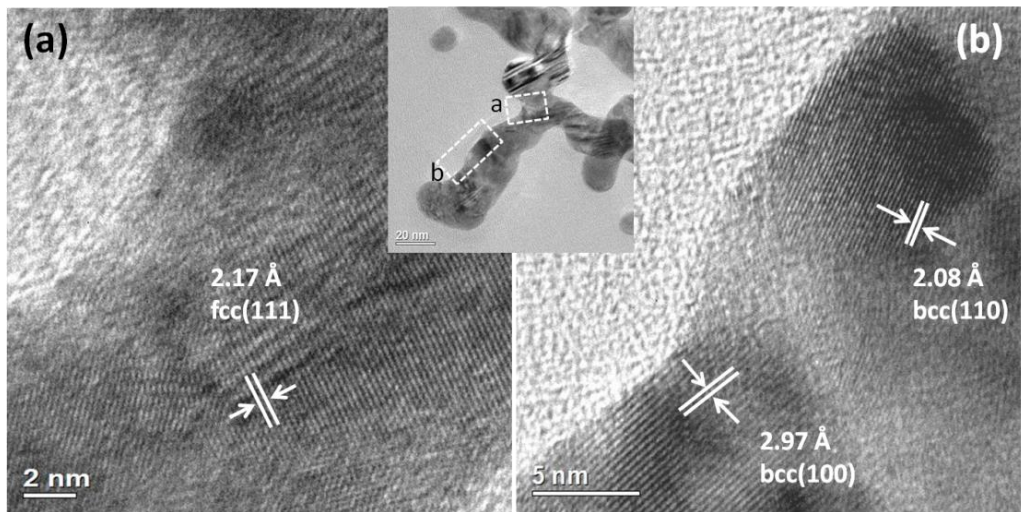


Figure 5.3 HRTEM images of domains with (a) a fcc structure and (b) a bcc structure in a CuPd nanowire. The inset shows a low magnification image of this nanowire, in which the areas marked by *a* and *b* correspond to HRTEM images (a) and (b).

Thermodynamically, the fcc phase is more stable, while the bcc phase is a structure with higher energy. Experimentally, we speculate that strong reducing agents can increase the reduction rate of CuPd clusters, so as to promote the formation of the bcc phase that is more loosely packed than the fcc structure. CuPd with pure bcc phase was produced when NaBH₄ was used as a strong reducing agent.^{10, 15} In the present work, EG with moderate reducing ability was used, resulting in the formation of both bcc and fcc type structures. The use of formanilide produced a more stable fcc structure, probably due to the weak reducing ability of formanilide that leads to a slower formation process (**Figure 5.2b**). CuPd synthesized with formanilide, however, exhibits morphology of spherical nanoparticles rather than branched nanowires (**Figure 5.4**). In **Figure 5.4b**, crystal fringes of a nanosphere with a *d*-spacing of 2.16 Å was observed, which is assigned to (111) planes of fcc-type CuPd alloy.

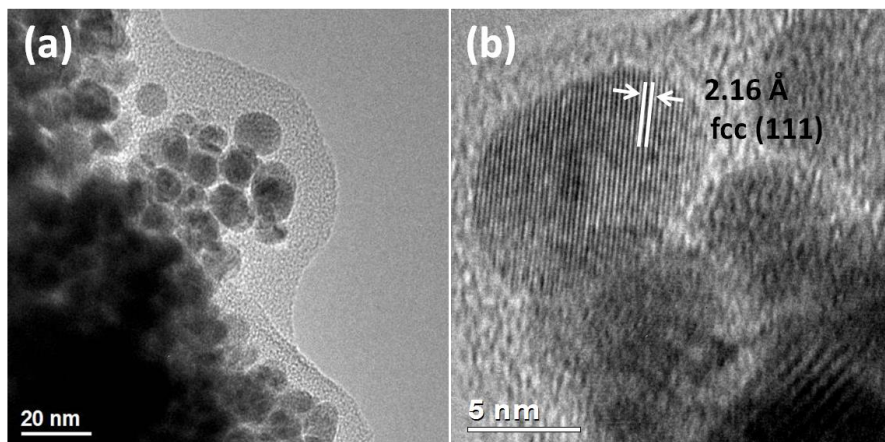


Figure 5.4 TEM images of CuPd nanoparticles reduced by formanilide in ODE, producing fcc structured CuPd nanoparticles.

5.4 Growth process

Intermediates at early stages were collected to study the growth process. After the precursors were totally dissolved at 80 °C, the reaction was stopped at 5 min and 10 min during the process of heating to 200 °C. The images of these intermediates are shown in **Figure 5.5**.

After 5 min of heating, nanospheres with an average size of 10.2 ± 1.3 nm (obtained after measuring 50 particles) had already formed. Most nanospheres are discrete, but some started to attach together to form peanut-shaped particles attached by two spheres or V-shaped particles by three (**Figure 5.5c-e**).

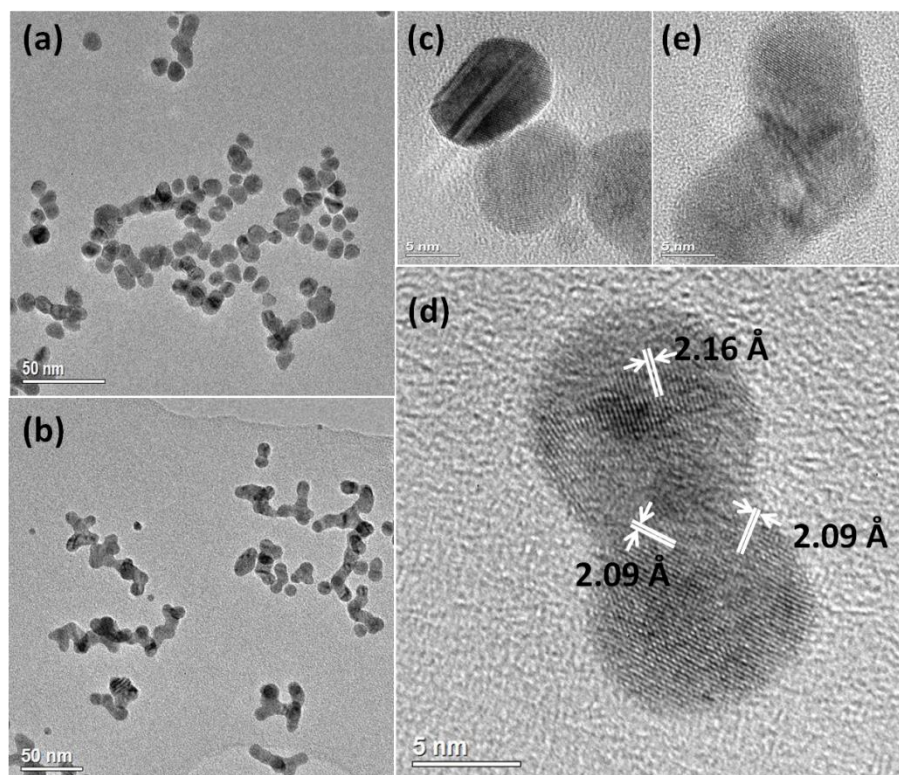


Figure 5.5 TEM images of (a) 5 min, (b) 10 min intermediates. HRTEM images of nanoparticles formed by attachment of (c) one, (d) two and (e) three spheres.

As the reaction was extended to 10 min, branched particles appeared in the product. Spherical units can still be distinguished from the branched rods. These branched rods would continue to join and connect, forming the final three-dimensional structure. The width of 10 min rod is ~ 10.3 nm, which is close to the diameter of 5 min intermediate spheres but much smaller than that of the final nanowires after 2 h reaction. It is expected that width of nanowires increases by the further deposition of CuPd atoms afterwards.

Interestingly, both bcc and fcc structures formed at the early stages. One representative image is given in **Figure 5.5d**, a peanut-shaped particle consists of two spheres. The upper

sphere is fcc-type with a d -spacing of 2.16 Å which corresponds to the {111} planes of fcc CuPd alloy. The lower one exhibits two dimensional lattice fringes that are perpendicular to each other. The d -spacings are both 2.09 Å, which can be indexed to {110} planes of bcc structured CuPd. There is an amorphous boundary lying at the interface.

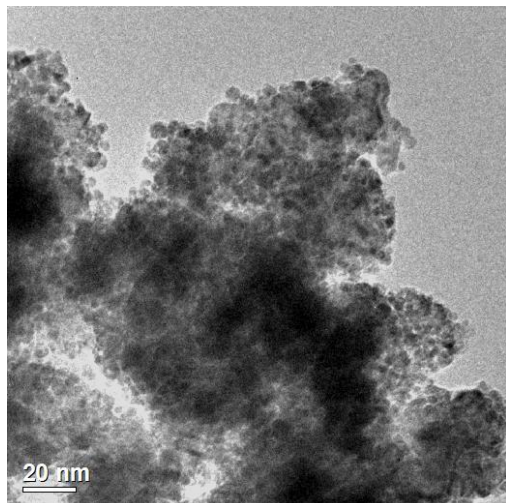


Figure 5.6 TEM images of agglomerated CuPd particles prepared in the absence of PVP.

After examination of many HRTEM images it was found that the crystallographic orientations across the newly-formed particles are not uniform. The oriented attachment mechanism,¹⁶ in which adjacent particles join together by sharing the same crystallographic orientations, is less likely in our work. We suspect the attachment occurs at the sites that are less passivated, *i.e.* with fewer capping agents (PVP) on. When PVP is absent in the synthesis, serious agglomeration happened (**Figure 5.6**), and particles stuck together in large clusters. On the other hand, it indicates the protection of PVP prevents the joint of particles. Therefore, stochastic collisions and attachment are most likely to take place at positions that are not well protected by PVP. Repeating adhesion of nanospheres and short rods led to the formation of nanowires with branches.

5.5 Surface characterization and shape control

As mentioned above, it is speculated that PVP has strong influence during the growth process. Fourier-transform infrared (FTIR) measurements and TEM observation were carried out and the existence of PVP on CuPd surface was confirmed.

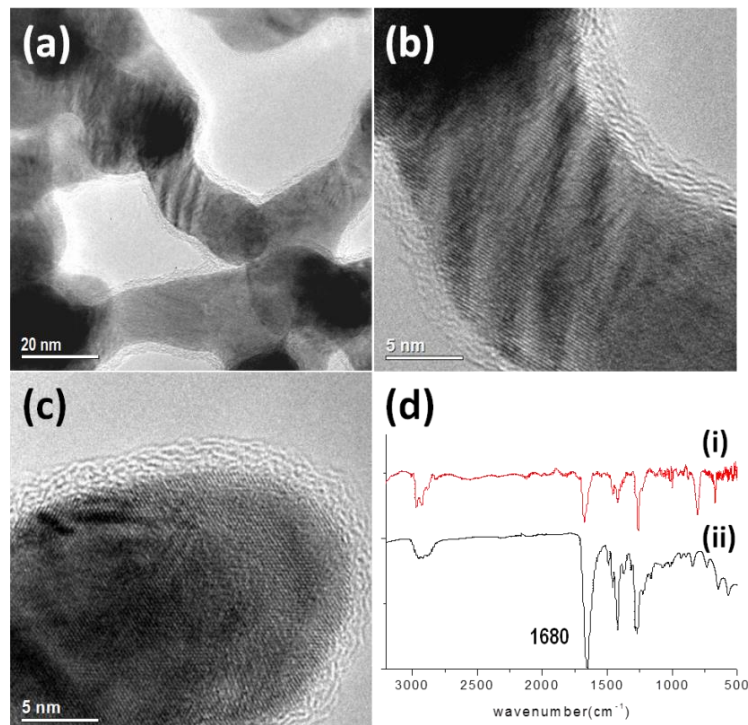


Figure 5.7 (a-c) TEM images demonstrating a thin layer of PVP on the surface of CuPd nanowire. (d) FTIR spectra of (i) CuPd-PVP nanowires and (ii) pure PVP.

Figure 5.7a-7c show that the surfaces of CuPd nanowires are covered by a thin layer, which has low-contrast and is about 2 nm thick. From HRTEM images **Figure 5.7a, 7b**, the low-contrast layer is unlikely to be an oxidized alloy phase. It resembles the polymer coating observed by Chen, *et al.*¹⁷ As the CuPd sample had been washed several times to remove residual reactants and excessive PVP, it can be concluded that the thin surface layer observed is PVP bound on the metal surface.

In the FTIR spectrum of CuPd nanowires (**Figure 5.7d**), the band centered at 1680 cm^{-1} is characteristic for PVP adsorption, which can be assigned to stretch of carbonyl.^{18, 19} The

similarity between spectra of pure PVP (ii) and CuPd nanowires (i) indicates the existence of PVP on metal surfaces. This is consistent with the thin polymer layer observed in HRTEM images.

With this understanding, we are able to tune the morphology of CuPd nanowire networks by changing the property of the surface ligands and solvent. PVP with different molecular weights, 10,000 and 40,000 respectively were used, while the weight of PVP was kept constant in the synthesis. In the presence of PVP 40,000, the morphology of CuPd nanowire networks remain more or less the same, with only a little degradation of pores and branches (**Figure 5.8a**). If the molecular weight of PVP is decreased to 10,000, significant changes can be observed. **Figure 5.8b** shows a TEM image of the product prepared with PVP 10,000, which shows aggregation of spherical particles. The network structure is destroyed and only a few pores were retained. It is known that PVP is polymer, and its average Mw reflects the degree of polymerization. Smaller Mw suggests shorter molecular chain and reduced steric hindrance.²⁰ Assuming there are a fixed number of adsorption sites on the metal surface, long adsorbed molecules are capable of providing better surface protection for the CuPd nanoparticles. As a result, particles have fewer chances to join together, leading to a network morphology as seen in **Figure 5.8a**. On the other hand, smaller Mw means short molecules and worse protection. Therefore, aggregated particles are produced as seen in **Figure 5.8b**.

On the other hand, solvent also has strong influence on morphology by changing the interactions between ligands and metal surfaces, as discussed in chapter 3.3. When 1-octadecene (ODE) was used as a solvent, CuPd nanospheres (XRD pattern is shown in **Figure 5.2c**) were produced as seen in **Figure 5.8c**. The nanospheres were separated, but nanoparticles prepared in EG are interconnected (**Figure 5.8b**).

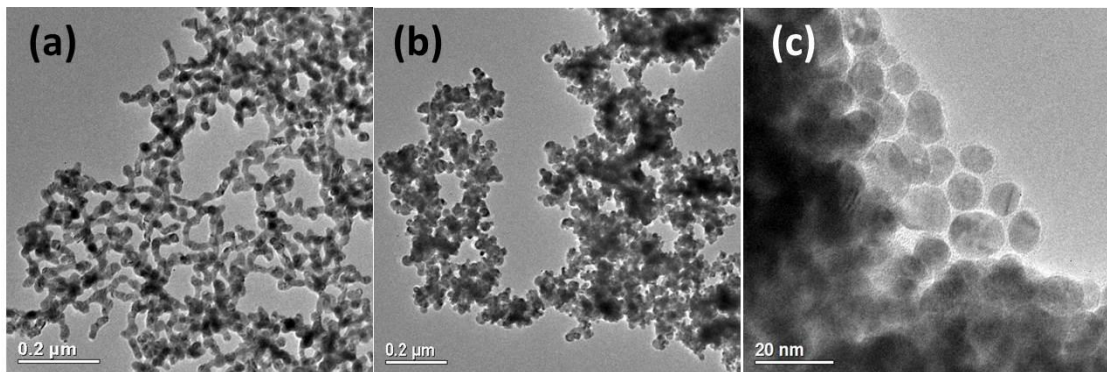


Figure 5.8 TEM images of CuPd nanoparticles prepared (a) in the presence of PVP with Mw = 40,000 (b), Mw = 10,000 in EG and (c) in ODE.

To elucidate the effect of solvent, the polarity of EG and ODE have to be taken into consideration. The dipole moment of ODE is 0.47D (Debye), while EG has a dipole moment of 2.28D. PVP is a kind of hydrophilic polymer. Hence, interaction between solvent and PVP will be weakened as the polarity of solvents decreases. Thus, the interactions between surface ligands and metal are enhanced in less polar solvents. In other words, the surfaces of CuPd nanoparticles are better protected by PVP in ODE, resulting in the formation of nanospheres instead of a branched structure. Similarly, spherical nanoparticles were obtained in ODE when formanilide was used as a reducing agent (**Figure 5.4**). It can also be explained by this solvent effect that better protection of a particle surface by PVP was achieved in ODE solvent, resulting in separated particles.

5.6 Electrochemical performances

The electrochemical test was carried out by Mr Y. Chen at University of St Andrews. Performances of CuPd nanowire networks were tested towards ORR. It was studied by cyclic voltammetry (CV) in 0.5 M HClO₄ aqueous solution saturated with O₂ at room temperature. CuPd nanowire networks prepared in the presence of PVP with different molecular weights are denoted as CuPd PVP 55000 and CuPd PVP 10000 in **Figure 5.9**, which shows the CVs

of CuPd catalysts loaded on carbon and Pt electrode for comparison. The curve in black is a standard CV pattern for O₂ reduction/oxidation and H₂ absorption/desorption on Pt. The peak centered at 0.62 V can be attributed to O₂ reduction on Pt surface. For CuPd PVP 55000, the green curve in **Figure 5.9**, a peak located at 0.65V was observed, which can be assigned to O₂ reduction.^{12, 14, 21} Furthermore, its peak current is very close to that of Pt, which demonstrates their comparable activity. For CuPd PVP 10000, the O₂ reduction peak shifted ~50 mV to the negative direction in comparison with CuPd PVP 55000. Although CuPd PVP 10000 displays reasonable peak potential and current, its catalytical performance towards ORR is not as good as that of CuPd PVP 55000. This could be attributed to its structure: CuPd networks prepared with PVP 10000 has few branches and is heavily aggregated, leading to a decrease of surface area as well as fewer exposed active sites.

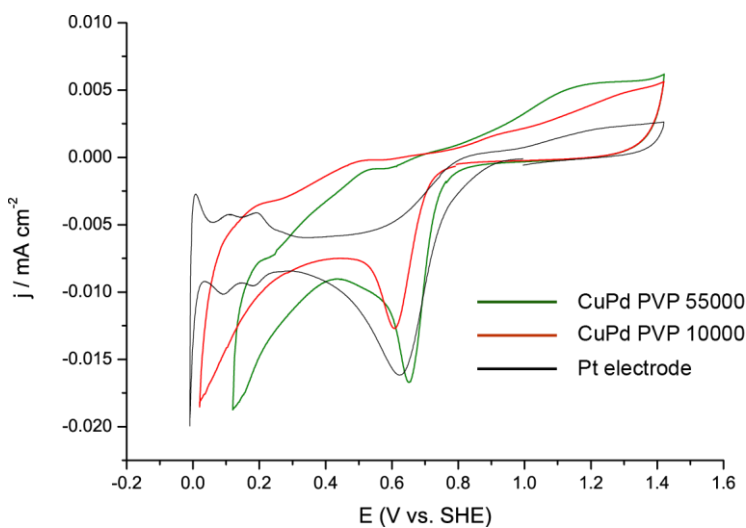


Figure 5.9 CV curves for CuPd catalysts and commercial Pt electrode in O₂ saturated HClO₄ solution.

The structure stability of the nanowires was studied after a higher number of cycles. The loaded CuPd PVP 55000 catalysts were separated from the electrode by dissolution in ethanol, and further examined by TEM. The CuPd nanowires retained their morphology and structure with no obvious changes, as shown in **Figure 5.10**. **Figure 5.10d** displays a HRTEM image of nanowires after reaction, showing they are still polycrystalline. But the current decayed significantly after cycles, possibly due to poisoning of active sites on CuPd catalysts.²²

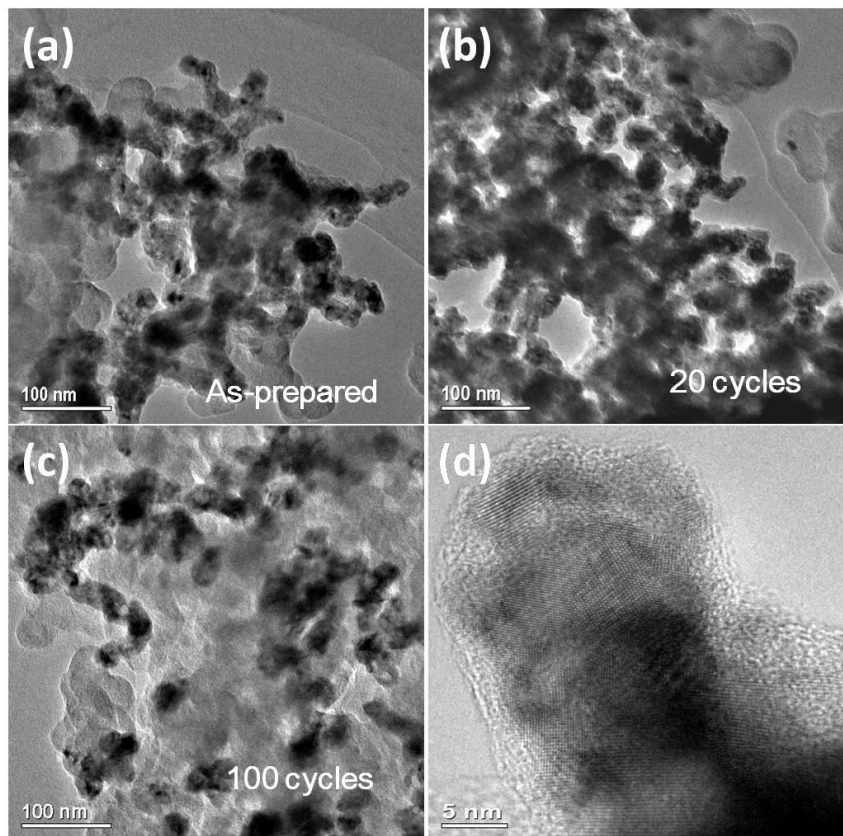


Figure 5.10 TEM images of CuPd nanowires PVP 55000 loaded on carbon. (a) As-prepared, (b) after 20 cycles of CV and (c) after 100 cycles of CV. (d) HRTEM image of the nanowires in (c). After testing, they remain polycrystalline. The structure of CuPd remained unchanged.

5.7 Other Pd-based nanoparticles

Other Pd-based nanoparticles were synthesized under the same experimental conditions. Monometallic Pd nanoparticles, AgPd and AuCuPd alloyed nanoparticles were prepared and characterized by TEM, EDX and XRD.

5.7.1 Pd

When Pd(acac)₂ alone was used as a metallic precursor under the same synthetic conditions, Pd nanoparticles possessing a polyhedron and triangular plate morphology were

produced in the presence of PVP (**Figure 5.11a**). A small amount of rectangular shaped nanoplates were also produced (**Figure 5.11b**).

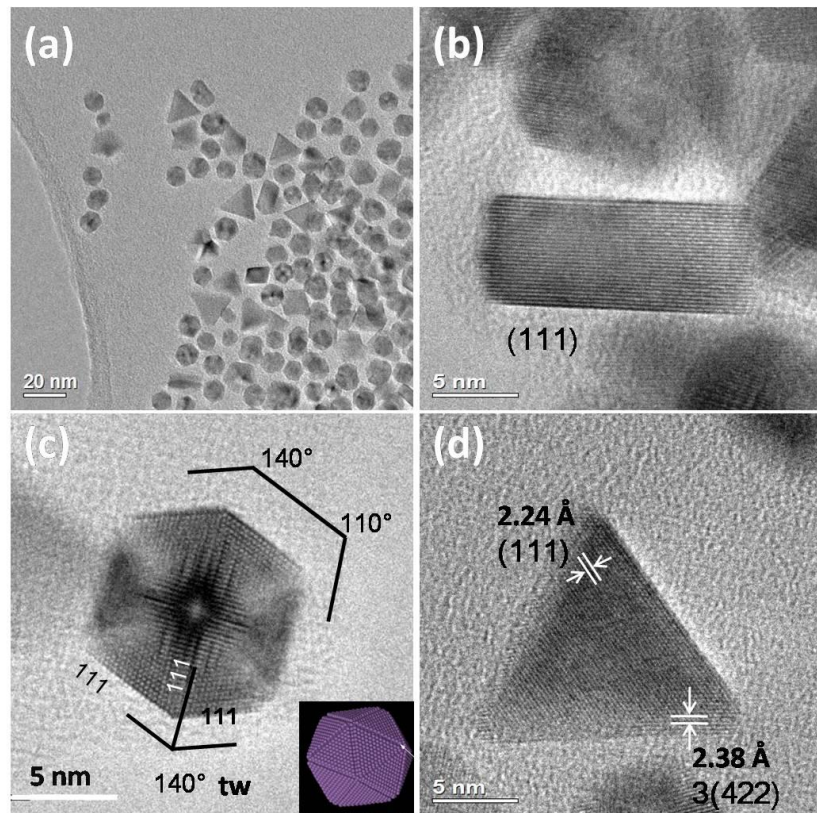


Figure 5.11(a) Low magnification TEM image of Pd nanoparticles. HRTEM images of (b) rectangular plate, (c) polyhedron and inset is an icosahedra model and (d) triangular plate.

Pd polyhedrons with a size of ~10 nm possess twinned facets (see **Figure 5.11c**). The lattice fringes in (c) have a *d*-spacing of 2.24 Å, which can be indexed to (111) planes of fcc Pd. The interplane angle of 70° is consistent with the angle between {111} planes. The morphology of the Pd polyhedron highly resembles icosahedra (see inset of **Figure 5.11c**), and has similarity with the HRTEM image of Pt icosahedra reported very recently.²³

A portion of triangular nanoplates with edge length of ~15 nm were also present. The contrast was uniform across the plate, indicating its plate feature. **Figure 5.11d** shows a HRTEM image of a triangular nanoplate. Two dimensional fringes are observed. One has a *d*-spacing of 2.24 Å, which can be indexed to (111) plane of Pd. The other has a *d*-spacing of 2.38 Å, which equals 3 × {422} fringes ($d_{422} = 0.81$ Å). The measured interplane angle

between {111} and {422} planes is $\sim 59^\circ$, matching the theoretical value of 61.8° . Reflections corresponding to the $3 \times \{422\}$ planes are usually forbidden in a fcc structure, but $3 \times \{422\}$ fringes are commonly observed in metallic nanoplates,^{24, 25} which could be caused by stacking faults.²⁵ Similar Pd nanoplates are also reported by Xia and co-workers²⁶ prepared by oxidative etching with the assistance of Fe^{3+} ions and Cl^-/O_2 pair using sodium palladium (II) chloride as precursor. The XRD pattern of Pd nanoparticles (**Figure 5.12**) can be assigned to fcc structured Pd (JCPDS 00-005-0681).

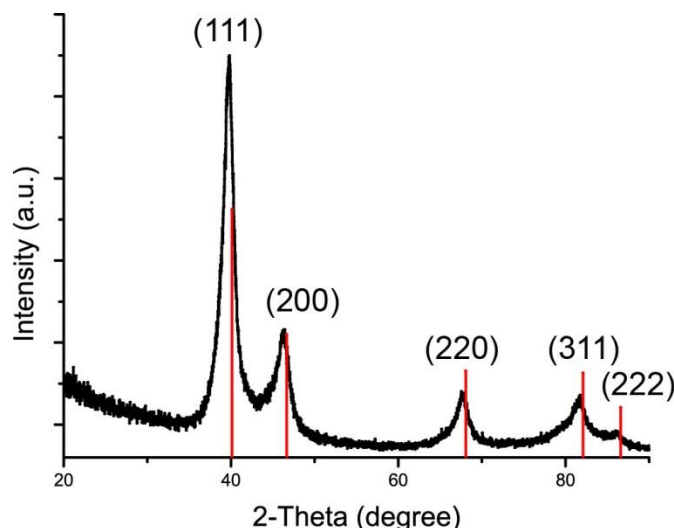


Figure 5.12 XRD pattern of Pd nanoparticles. The red vertical lines represent the peak positions of fcc structured Pd (JCPDS 00-005-0681). The intensity of (111) peak of as-prepared Pd is higher than the reference value.

It is noticed that the intensity ratio of (111) peak in XRD is higher than the literature value for powder samples. For a fcc structured crystal with a lattice constant a , the interfacial free energy, γ of the {100}, {110} and {111} planes can be estimated to be:

$$\gamma\{100\} = 4 (\varepsilon/a)^2$$

$$\gamma\{110\} = 4.24 (\varepsilon/a)^2$$

$$\gamma\{111\} = 3.36 (\varepsilon/a)^2$$

in which ε is the bond strength.

Therefore, low energy {111} facets can compensate the high surface energy caused by shape. For polyhedron particles, the strain energy caused by twin defects will increase as the particle grows up.²⁷ Such strain at the interface will cause distorted regions at the boundaries. Therefore, twinned particles are only favored when they are small in size. Indeed, the polyhedron particles with twin defects were smaller in size than the other two shapes.

5.7.2 AgPd

AgPd nanowire networks were prepared with the same method simply replacing Cu salt with AgNO₃. AgPd was chosen because it has a different catalytic property: CuPd bimetallic alloy serves as an electron acceptor but AgPd alloys serve as a donor indicated by XPS study, due to quantum trapping and charge polarization, respectively.²⁸ The catalytic performance relies on the alloy's intrinsic properties. As a result, AgPd alloy may exhibit totally different catalytic activity in comparison of CuPd.

AgPd nanowires were successfully prepared as shown in **Figure 5.13a**. The XRD pattern proves the alloy phase of AgPd (**Figure 5.13b**). The HRTEM image in **Figure 5.13c** shows fringes with a *d*-spacing of 2.29 Å, which can be assigned to (111) planes of AgPd. EDX spectrum (**Figure 5.13d**) further confirmed the alloy composition with a ratio of Ag: Pd = 55: 45. In EDX spectrum, some peaks from Pd and Ag elements overlap. In order to achieve accurate results, the K_α peaks were chosen to calculate the composition. Ag K_α is located at 2.98 keV while Pd K_α is centered at 2.83 keV, which makes it possible to distinguish between the two elements.

There are only a few reports of one-pot preparation methods for AgPd bimetallic nanowires, but mainly by electrochemical deposition or/and with the assistance of porous aluminum template.^{29, 30} The synthetic method used in the present work is a simple one-pot preparation, which has demonstrated its versatility by the successful fabrication CuPd and AgPd nanowires.

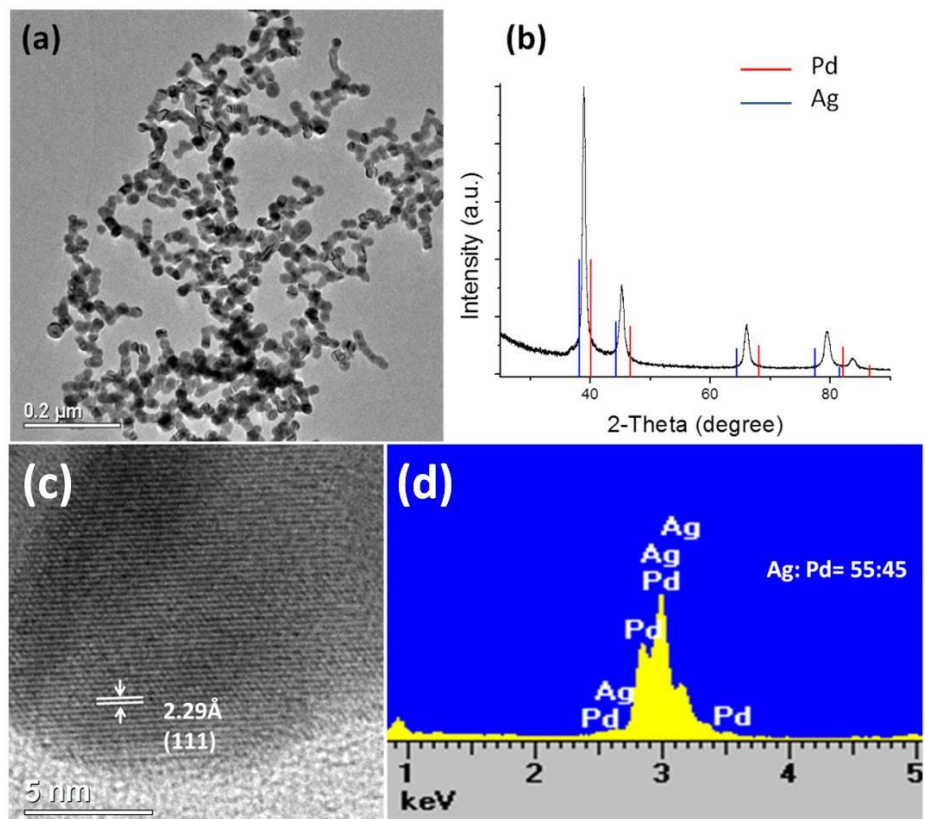


Figure 5.13 (a) TEM image and (b) XRD pattern of AgPd nanowires. Red and blue vertical lines indicate the position of Pd (JCPDS 00-005-0681) and Ag (JCPDS 01-071-3762), respectively. (c) HRTEM image of a AgPd nanowire and (d) EDX spectrum of AgPd alloy, showing a ratio of Ag: Pd = 55: 45.

5.7.3 AuPd and AuCuPd

Using the same synthetic method for CuPd nanowires but replacing the Cu precursor with HAuCl₄ 3H₂O produced small AuPd nanoparticles. A TEM image of AuPd nanoparticles is displayed in **Figure 5.14a**. The size distribution of AuPd nanoparticles was not very uniform. Small particles were ~5 nm in diameter, while large ones were ~15 nm in size.

In the HRTEM image in **Figure 5.14b**, two facets of a polyhedron particle can be observed. The left facets shows (111) and (200) planes of AuPd alloy with a interplane angle of 56 °(Pure Au d₁₁₁ = 2.35 Å, JCPDS 00-004-0784, pure Pd d₁₁₁ = 2.24 Å). While two (111)

planes with an angle of 71° were observed on the right facets. The lattice d -spacings were consistent with the values of alloyed phase. EDX analysis (**Figure 5.14c**) revealed a Au: Pd ratio of 66: 34.

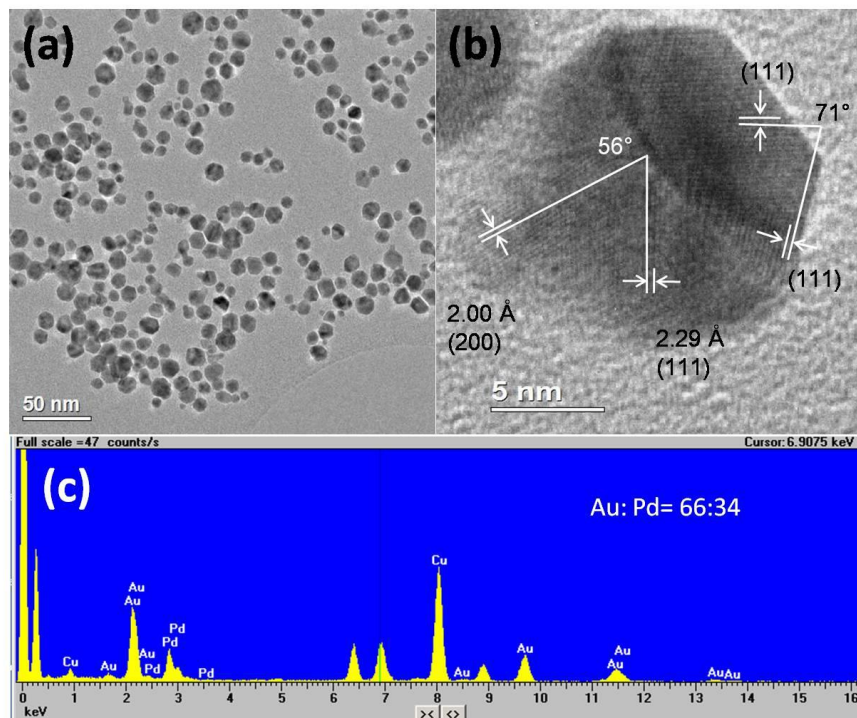


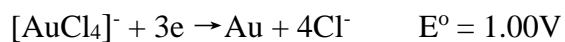
Figure 5.14 (a) TEM image of AuPd nanoparticles., (b) HRTEM image of a AuPd particle with fringes that can be indexed to (111) and (200) planes of AuPd alloy and (c) EDX spectrum showing a ratio of Au: Pd = 66: 34.

The peaks are asymmetric in the XRD pattern of AuPd nanoparticles (**Figure 5.15a**). This indicates the composition of different particle varies; Au particles may coexist with AuPd alloy in the product. This can be attributed to the higher bonding energy of Au-Au (226 kJ/mol)³¹ while the bonding energy of Au-Pd is 143 kJ/mol.³²

In the AuPd system, small nanoparticles instead of nanowires were produced using the same method as for CuPd nanowire synthesis. The rapid reduction rate of $[\text{AuCl}_4]^-$ precursor could be one of the reasons.

The standard potentials E° of the redox pairs are listed below.³³ The standard potentials are measured at a pressure of 101.325 kPa and 298.15 K in aqueous solution. Our experimental

condition can lead to deviations from the standard potentials, but they can still reflect the relative activity of different metals.



$[\text{AuCl}_4]^-$ has more positive potential, so it is easier to be reduced. The rapid rate of nucleation in AuPd system will lead to a large number of seeds, and consequently smaller particles in the final product.³⁴ The reduction rates in Ag^+ and Cu^{2+} system are slower than that of Au system as suggested by the potentials. The CoPd system was also studied, in which Co^{2+} has negative potential and should remain intact. Indeed, only Pd was reduced to Pd nanoparticles with a morphology very similar to that of the Pd alone system.

A nanowire morphology can be obtained by a combination of Au-Cu-Pd elements. Alloyed AuCuPd nanowires were prepared by adding Au precursor after Cu and Pd precursors were reduced. $\text{Pd}(\text{acac})_2$, $\text{CuSO}_4 \cdot 5\text{H}_2\text{O}$ and PVP were dissolved in EG, and heated to 200 °C for reaction after complete dissolution. After reaction for 10 min, EG solution of $\text{HAuCl}_4 \cdot 3\text{H}_2\text{O}$ was added into the solution and further reacted for 2 h. Porous AuCuPd nanowires were synthesized by galvanic replacement reaction between as-prepared CuPd nanowires and $[\text{AuCl}_4]^-$ at room temperature. HAuCl_4 solution was added dropwise into the CuPd dispersion in water and reacted for 16 h under stirring.

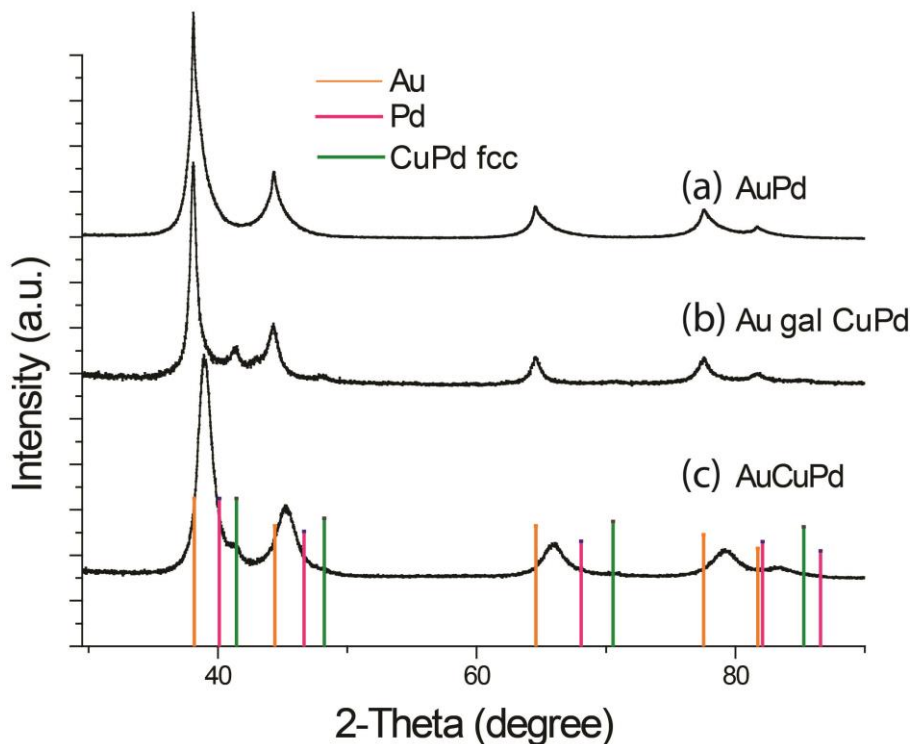


Figure 5.15 XRD patterns of (a) AuPd nanoparticles, (b) CuPd nanowires after galvanic treatment of HAuCl₄ solution and (c) AuCuPd nanowires. The vertical lines represent the peak positions of references. Orange: Au (JCPDS 00-004-0784), pink: Pd (JCPDS 00-005-0681) and green: CuPd fcc (JCPDS 00-048-1551).

Figure 5.16 displays TEM images of nanowires produced by these two methods. AuCuPd nanowires prepared by co-reduction of three metal precursors (**Figure 5.16a, 16b**) were ~25 nm in width. The contrast throughout the nanowires was quite uniform in TEM, indicating an even elemental distribution. EDX mapping was carried out on the AuCuPd nanowires and the distribution of Au and Pd was uniform. The XRD pattern of the nanowires showed no Au peak (or monometallic Cu, Pd peaks) in **Figure 5.15c**, which confirms the alloyed phase.

In contrast, porous AuCuPd nanowires were obtained by the galvanic replacement method. **Figure 5.16c, 16d** show the images of porous nanowires with some particles attached. The XRD pattern in **Figure 5.15b** has very strong Au peaks besides CuPd reflections. It suggests segregated Au particles have formed. EDX analysis gives an atomic ratio of Au: Cu: Pd = 47: 21: 32.

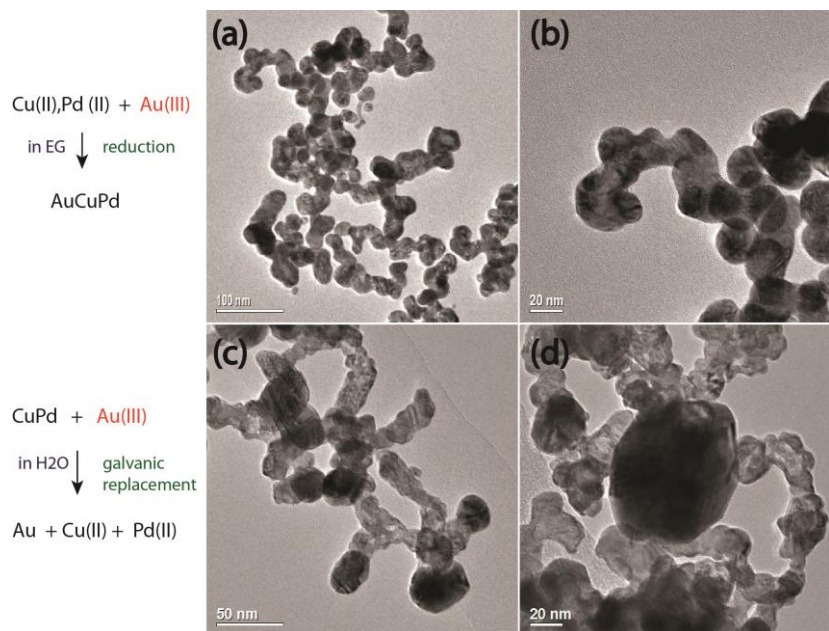


Figure 5.16 TEM images of (a,b) alloyed AuCuPd nanowires prepared by co-reduction and (c,d) porous AuCuPd nanowires prepared by galvanic replacement reaction between Au(III) and CuPd nanowires. Left is the illustration of two different reaction methods.

As suggested by the standard potentials of Cu, Pd and Au below,³³ AuCl_4^- can oxidize both Cu and Pd into ions and produce Au at the same time. The consumption of Cu and Pd leads to the formation of a porous structure.



In summary, AuPd nanowires were not able to be synthesized due to the very positive potential of Au ions. But AuCuPd nanowires can be produced with the assistance of co-reduction or galvanic replacement methods. Co-reduction produces alloyed phase nanowires, while galvanic replacement can generate a porous structure.

References

1. B. C. Tappan, S. A. Steiner and E. P. Luther, *Angew. Chem. Int. Ed.*, 2010, **49**, 4544-4565.
2. J. H. Cui, H. Zhang, Y. F. Yu, Y. Liu, Y. L. Tian and B. Zhang, *J. Mater. Chem.*, 2012, **22**, 349-354.
3. C. W. Cheng and H. J. Fan, *Nano Today*, 2012, **7**, 327-343.
4. Y. Song, R. M. Garcia, R. M. Dorin, H. R. Wang, Y. Qiu, E. N. Coker, W. A. Steen, J. E. Miller and J. A. Shelnutt, *Nano Lett.*, 2007, **7**, 3650-3655.
5. H. J. Shin, R. Ryoo, Z. Liu and O. Terasaki, *J. Am. Chem. Soc.*, 2001, **123**, 1246-1247.
6. Y. Xu, R. Xu, J. H. Cui, Y. Liu and B. Zhang, *Chem. Commun.*, 2012, **48**, 3881-3883.
7. A. K. Sra, T. D. Ewers and R. E. Schaak, *Chem. Mater.*, 2005, **17**, 758-766.
8. C. L. Lee, Y. C. Huang, L. C. Kuo, J. C. Oung and F. C. Wu, *Nanotechnology*, 2006, **17**, 2390-2395.
9. P. Reyes, A. Figueroa, G. Pecchi and J. L. G. Fierro, *Catal. Today*, 2000, **62**, 209-217.
10. M. Yamauchi, R. Abe, T. Tsukuda, K. Kato and M. Takata, *J. Am. Chem. Soc.*, 2011, **133**, 1150-1152.
11. N. Toshima and Y. Wang, *Adv. Mater.*, 1994, **6**, 245-247.
12. X. P. Wang, N. Kariuki, J. T. Vaughey, J. Goodpaster, R. Kumar and D. J. Myers, *J. Electrochem. Soc.*, 2008, **155**, B602-B609.
13. W. J. Tang, L. Zhang and G. Henkelman, *J. Phys. Chem. Lett.*, 2011, **2**, 1328-1331.
14. L. Zhang, F. Hou and Y. W. Tan, *Chem. Commun.*, 2012, **48**, 7152-7154.
15. M. Yamauchi and T. Tsukuda, *Dalton Trans.*, 2011, **40**, 4842-4845.
16. J. Zhang, F. Huang and Z. Lin, *Nanoscale*, 2010, **2**, 18-34.
17. G. Z. Chen, M. S. P. Shaffer, D. Coleby, G. Dixon, W. Z. Zhou, D. J. Fray and A. H. Windle, *Adv. Mater.*, 2000, **12**, 522-526.
18. B. H. Yang, J. R. Li, J. F. Wang, H. Y. Xu, S. Y. Guang and C. Li, *J. Appl. Polym. Sci.*, 2009, **111**, 2963-2969.
19. H. S. Wang, X. L. Qiao, J. G. Chen, X. J. Wang and S. Y. Ding, *Mater. Chem. Phys.*, 2005, **94**, 449-453.
20. D. S. Li and S. Komarneni, *J. Am. Ceram. Soc.*, 2006, **89**, 1510-1517.

21. B. Lim, M. J. Jiang, P. H. C. Camargo, E. C. Cho, J. Tao, X. M. Lu, Y. M. Zhu and Y. N. Xia, *Science*, 2009, **324**, 1302-1305.
22. W. Liu, A.-K. Herrmann, D. Geiger, L. Borchardt, F. Simon, S. Kaskel, N. Gaponik and A. Eychmüller, *Angew. Chem. Int. Ed.*, 2012, **51**, 5743-5747.
23. W. Zhou, J. Wu and H. Yang, *Nano Lett.*, 2013, **13**, 2870-2874.
24. R. C. Jin, Y. W. Cao, C. A. Mirkin, K. L. Kelly, G. C. Schatz and J. G. Zheng, *Science*, 2001, **294**, 1901-1903.
25. V. Germain, J. Li, D. Ingert, Z. L. Wang and M. P. Pilani, *J. Phys. Chem. B*, 2003, **107**, 8717-8720.
26. Y. J. Xiong, J. M. McLellan, J. Y. Chen, Y. D. Yin, Z. Y. Li and Y. N. Xia, *J. Am. Chem. Soc.*, 2005, **127**, 17118-17127.
27. Y. N. Xia, Y. J. Xiong, B. Lim and S. E. Skrabalak, *Angew. Chem. Int. Ed.*, 2009, **48**, 60-103.
28. C. Q. Sun, Y. Wang, Y. G. Nie, B. R. Mehta, M. Khanuja, S. M. Shivaprasad, Y. Sun, J. S. Pan, L. K. Pan and Z. Sun, *Phys. Chem. Chem. Phys.*, 2010, **12**, 3131-3135.
29. E. H. Yue, G. Yu, Y. J. Ouyang, B. C. Weng, W. W. Si and L. Y. Ye, *J Mater Sci Technol*, 2008, **24**, 850-856.
30. Y. K. Xiao, B. C. Weng, G. Yu, J. Y. Wang, B. N. Hu and Z. Z. Chen, *J. Appl. Electrochem.*, 2006, **36**, 807-812.
31. H. Zhang, M. S. Jin, J. G. Wang, M. J. Kim, D. R. Yang and Y. N. Xia, *J. Am. Chem. Soc.*, 2011, **133**, 10422-10425.
32. D. R. Lide, *CRC handbook of chemistry and physics*, 89th edition, CRC Press, 2008.
33. A.J. Bard, R. Parsons and J. Jordan, *Standard Potentials in Aqueous Solutions*, Marcel Dekker, New York, 1985.
34. E. V. Shevchenko, D. V. Talapin, H. Schnablegger, A. Kornowski, O. Festin, P. Svedlindh, M. Haase and H. Weller, *J. Am. Chem. Soc.*, 2003, **125**, 9090-9101.

Chapter 6 Alloying and Dealloying of CuPt Nanoparticles

6.1 Introduction

Research on alloyed bimetallic nanoparticles has been very intriguing and attracted considerable attention. Alloying offers a new perspective to reduce cost and improve durability and intrinsic properties.¹ Among many bimetallic nanoparticles, CuPt nanoalloys have various applications such as in catalysis and fuel cells.²⁻⁴

To achieve controllable fabrication of nanocrystals, a fundamental understanding of growth mechanism is essential. Ostwald ripening mechanism is widely used to explain crystal growth, in which larger particles grow larger at the expense of consuming smaller ones driven by decrease of the total energy.⁵ As synthetic methods of nanocrystals develop and many capping agents are involved in preparation, Ostwald ripening mechanism cannot well explain the growth of crystals in many systems, in which aggregation of small particles significantly disturbs the homogeneous environment. Previous investigations of growth process on zeolite analcime⁶ and zeolite A⁷ reveal that crystallization can start from the surface of amorphous aggregates, and extend from surface to core. This reversed crystal growth route has also been observed during the growth process of perovskites prepared in the presence of poly(ethylene glycol).^{8, 9} Metallic crystals¹⁰ and organic crystals¹¹ have also been found to follow this reversed crystal growth route. Reversed growth in bimetallic nanocrystals, however, has rarely been reported.

Dealloying refers to the selective removal of the more active metal element out of an alloy. Chemical dealloying is a common method to dissolve an active metal by acid and leave the noble metal behind. It has a history of more than 80 years but has mainly focused on corrosion. Recently, dealloying has received renewed attention due to its potential as an effective method to fabricate nanoparticles with interesting properties.¹² For instance, core-shell structured nanoparticles with a noble-metal-rich shell were prepared by dealloying and applied as a fuel cell catalyst.¹³ Nanoporous nanoparticles were fabricated by acid etching.

The products have large surface area and small pores, and show better performance than the solid ones in electrochemical tests.¹⁴

In this chapter, bimetallic CuPt nanoparticles with sizes ranging from 3 to 30 nm were prepared. The growth process of CuPt nanoparticles in the presence of hexadecylamine as capping agent was studied by HRTEM. A reversed crystal growth route of the nanoalloys is demonstrated. We also varied the nominal molar ratios of Cu and Pt in the synthesis and the degree of alloying and alloy compositions were investigated. Nanoalloys with different sizes were treated with chemical dealloying to examine the influence of size on dealloyed morphology. The present work provides practical guidelines for the synthesis of CuPt nanoparticles with various morphologies and structures.

6.2 Experimental section

Synthesis of alloyed CuPt nanoparticles

CuPt nanoparticles capped with hexadecylamine for a study of the mechanism were synthesized as following. 22 mg of platinum acetylacetone [Pt(acac)₂], 14 mg of CuSO₄ 5H₂O and 370 mg of hexadecylamine (HDA) as surface ligands were mixed together with 4.0 mL of ethylene glycol in a round-bottom flask equipped with a condenser. The mixture was heated to 200 °C at a heating rate of ~20 °C/min. Intermediate products were collected at different reaction times during the temperature-rising process. The CuPt nanoparticles were separated by precipitating the colloids using a sufficient amount of ethanol, followed by centrifugation at 3600 rpm for 10 min. The product was re-dispersed in hexane for further characterization.

We also varied the nominal ratios of Cu and Pt precursors while keeping the reaction temperature and concentration of HDA constant. Samples with Cu: Pt molar ratio of 7: 3, 3: 7 and 2: 8 were prepared and the degree of alloying between Cu and Pt were examined.

Synthesis of dealloyed CuPt nanoparticles

CuPt nanoparticles for dealloying treatment were prepared with the same method except replacing HDA with poly(vinylpyrrolidone) (PVP) as the capping agent. 0.11 mmol of platinum acetylacetonate [Pt(acac)₂], 0.11 mmol of CuSO₄ 5H₂O, 3 mg of PVP (Mw 55000), and 5 mL of ethylene glycol were mixed in a round-bottom flask. The mixture was then slowly heated to dissolve the chemicals under stirring. The solution was further refluxed at 200 °C for 2 h, where a black colloid suspension formed. The nanoparticles were separated from the solvent by the addition of acetone followed by centrifugation. In another synthesis, the initial molar ratio of Cu and Pt precursors was changed from 1: 1 to 7: 3 with all the other experiment conditions unchanged to obtain larger CuPt nanoparticles.

To dealloy the specimens, as-prepared Cu-Pt nanoalloys were treated with 25 mL of 1 M H₂SO₄ at 80 °C for 42 h under stirring to selectively dissolve Cu. The products were then washed with de-ionized water several times.

Characterization

Selected area diffraction (SAED) patterns, transmission electron microscopy (TEM), and high resolution TEM (HRTEM) images were obtained on a JEOL-2011 electron microscope operating at 200 kV equipped with an Oxford Link ISIS system for energy-dispersive X-ray spectroscopy (EDX). Samples for TEM characterization were diluted in hexane or acetone and then drop-casted onto a copper grid coated with a carbon film. The grids were dried in air at room temperature. The chemical composition of the nanoparticles was examined by EDX using an Oxford INCA system attached to a JEOL JSM-5600 scanning electron microscope operating at 20 kV. Average EDX results were made on at least ten different regions. Individual compositions of nanocrystals were determined by the measurement of the lattice *d*-spacings after the camera length of the microscope was carefully calibrated, assuming that the

unit cell dimensions of the alloys obey Vegard's law. Powder X-ray diffraction (XRD) was performed on a PANalytical Empyrean diffractometer with Cu K α radiation.

6.3 Reversed crystal growth of CuPt nanoparticles

CuPt nanoparticles were prepared with 1: 1 molar ratio of Pt(acac)₂ and CuSO₄ 5H₂O in the presence of hexadecylamine (HDA). **Figure 6.1a** gives a representative TEM image of CuPt nanoparticles after 10 h reaction. Most of the nanoparticles were single crystals. In **Figure 6.1b** a single crystalline particle with lattice *d*-spacing of 2.18 Å is observed, which is consistent with the expected *d*-spacing of (111) planes of the CuPt alloy (2.191 Å).

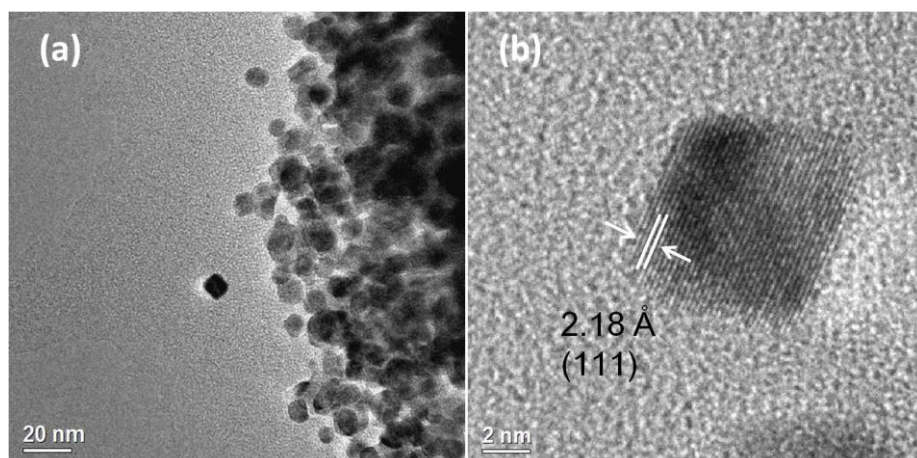


Figure 6.1 Images of CuPt nanoparticles after a 10 h reaction. (a) Low magnification TEM image and (b) HRTEM image showing lattice fringes of the CuPt (111) planes.

After measurements of ten different spots, EDX results indicate an average Cu: Pt ratio of 1: 1.04 ± 0.13, matching well with the 1: 1 CuPt alloy. The broadening of XRD peaks in **Figure 6.2a** suggest a crystallite size in the nanoscale.

Based on classic crystal growth theory, a crystal is developed from a nucleus *via* repeated deposition of atoms onto it. A single crystal state can be expected all through the growth process, with only gradually increased crystal size. Investigations of the early stage products in CuPt nanoalloys, however, revealed a different crystal growth route.

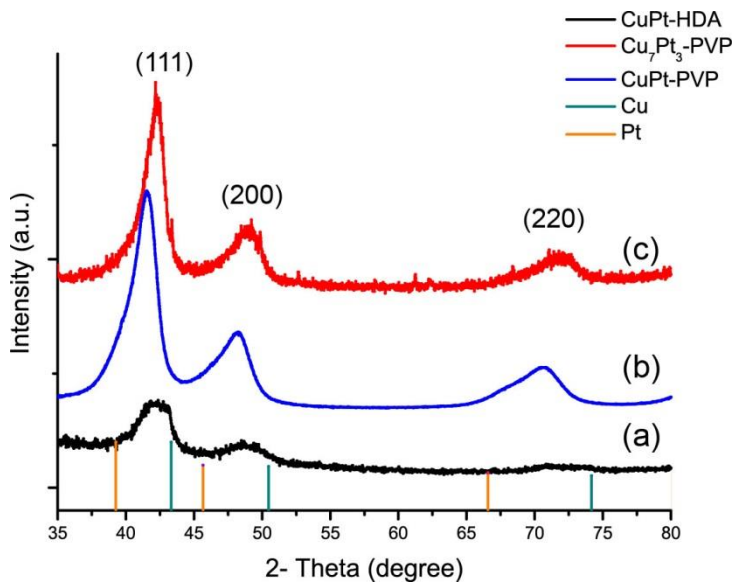


Figure 6.2 XRD patterns of (a) 10 h CuPt nanoparticles prepared with HDA, (b) CuPt nanoparticles synthesized with PVP and (c) Cu₇Pt₃ nanoparticles synthesized with PVP. Yellow and green lines represent peaks of pure Pt and Cu respectively.

The intermediate specimens at early stages were studied to explore the growth mechanism. During the heating process to 200 °C in the synthesis, the solution underwent a quick colour change: from deep green to slightly yellow, then to brown and finally to dark brown, indicating that reduction of metals had occurred. **Figure 6.3a** shows a typical particle collected when the solution colour changed to yellow after reaction for 6 min. This spherical particle is amorphous with a size of about 20 nm. It gave neither diffraction spots in the SAED patterns nor lattice fringes in the HRTEM images. The low density of the spherical particles, as indicated by a significant shrinkage of the particle sizes with elongated reaction time (**Figure 6.3c, 3d**), implies that they consist of the undecomposed precursors and HDA molecules. The original green colour of the solution was attributed to a mixture of yellow from Pt(acac)₂ and blue from CuSO₄ 5H₂O. When the temperature increased to over 110 °C, CuSO₄ 5H₂O underwent a dehydration process and lost the blue colour. The yellow solution suggests that no metal was reduced at this stage and Pt precursors were intact.

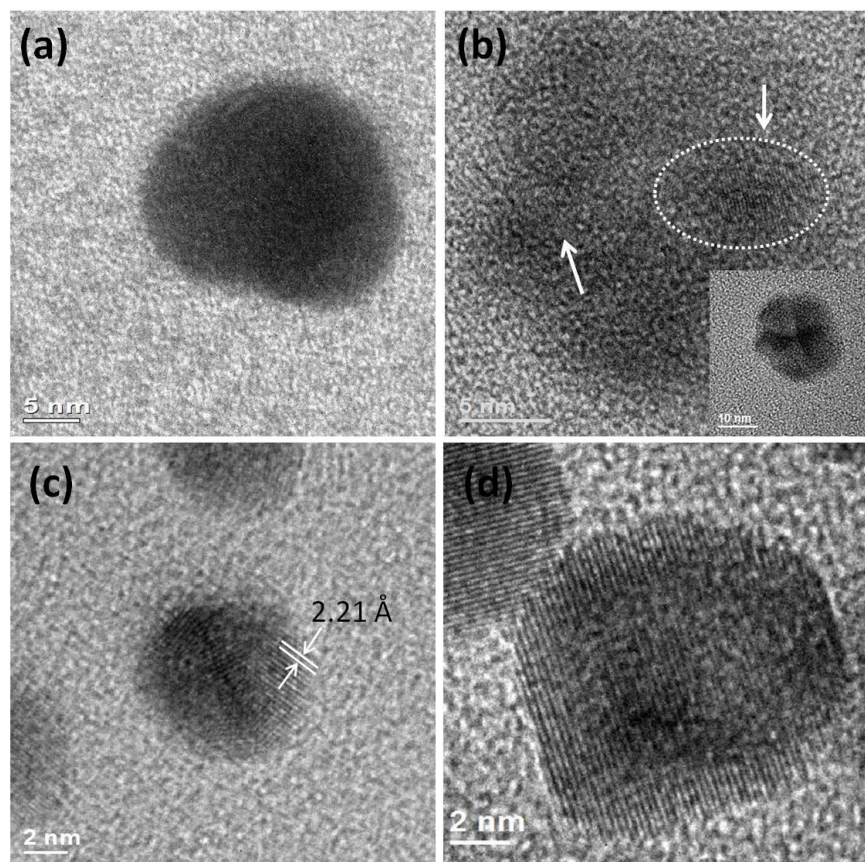


Figure 6.3 HRTEM images of CuPt nanoparticles after different reaction times: (a) 6 min when the solution colour changed from green to yellow, (b) 8 min when the solution colour changed to brown. The arrows indicate some separated nanocrystallites. The inset is the low magnification TEM image of this particle. (c) and (d) HRTEM images of nanoparticles after reaction for 0.5 h and 1.5 h, respectively.

Figure 6.3b displays a HRTEM image of a particle from a specimen collected after 8 min reaction when the solution turned brown. Reduction of metals started at this stage. Some small crystalline islands were observed on the particle, as well as lattice fringes (indicated by the circle and arrows). It indicates that multiple nucleation occurs on the particle surface.¹⁵ The principle reductant is the solvent ethylene glycol in this synthetic system, thus the surface of the spherical particles has the best contact between the precursors and reductant. Therefore, nucleation is most likely to take place on the surface in the first place. The inset of **Figure 6.3b** shows the low magnification TEM image of the same particle. The contrast is not uniform, and the dark areas induced by diffraction contrast correspond to areas where crystallization

occurs. In other words, areas with lattice fringes indicated by the arrows are the dark parts in the low magnification image.

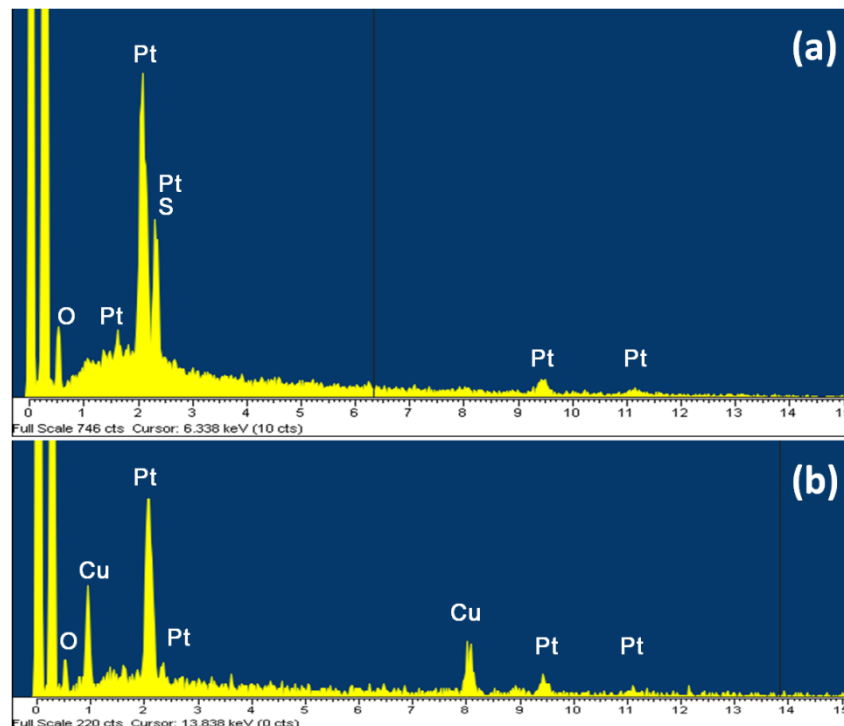
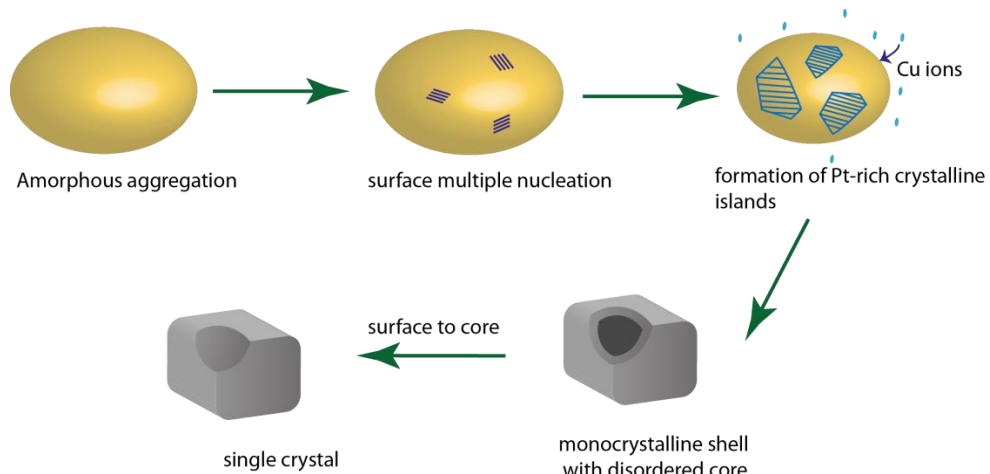


Figure 6.4 EDX spectra from the particles in a sample (a) at early stages of growth and (b) a 10 h reaction time.

Particles in the early growth stages principally consisted of the elements C, O, S and Pt, with only an extremely small amount of Cu if any (see EDX spectrum in **Figure 6.4a**). On the other hand, strong peaks of Pt and Cu are observed in the EDX spectrum from the 10 h sample, with an atomic ratio of about 1: 1 (**Figure 6.4b**). According to the EDX results, it is concluded that the amorphous spheres are mainly composed of $\text{Pt}(\text{acac})_2$, HDA and SO_4^{2-} anions, presumably owing to their much stronger interaction¹⁶ than that between HDA and Cu cations. A Pt-blank experiment was carried out in the absence of $\text{Pt}(\text{acac})_2$ while all the other parameters remained identical. Due to the weak interactions between Cu and HDA, Cu particles as large as 200 nm were produced caused by lack of good protection on the surface.

HRTEM images of particles after reaction for 0.5 h and 1.5 h at 200 °C are displayed in **Figure 6.3c, 3d** respectively. After 0.5 h reaction, the crystalline islands grow into larger pieces, while the whole particle is still polycrystalline. The d -spacing of the marked lattice fringes is 2.21 Å, which can be assigned to the (111) planes of Pt-rich alloy ($d_{111} = 2.19$ Å for 1:1 CuPt alloy). EDX result also shows a Pt-rich composition. The particle from 1.5 h sample in **Figure 6.3d** has a core-shell structure. Polycrystalline pieces fused and adjusted their orientations to form a single crystalline shell, covering an amorphous core. There are clear boundaries between core and shell in the HRTEM image, which separates the crystalline shell and disordered core. The d -spacing of the fringes is 2.20 Å, corresponding to the (111) planes of Pt-rich alloy. It is noteworthy that particles in 0.5 h and 1.5 h samples are ~10 nm in size, which are much smaller compared with the ones in early stages. This shrinkage is believed to be associated with the loss of (acac) anions and HDA molecules and the increase in density.



Scheme 6.1 Proposed growth mechanism of CuPt nanocrystals *via* a surface to core crystallization route. The yellow colour represents a Pt-rich composition.

Based on the experimental results above, a growth mechanism of CuPt bimetallic nanocrystals is proposed and illustrated in **Scheme 6.1**. At a very early growth stage, Pt precursor molecules and HDA aggregate into amorphous spheres. This aggregation process suppresses individual nucleation in solution. Instead, multiple nucleation takes place on the surface of the aggregates where the sites have good contact with the reductant solvent.

Meanwhile Cu ions gradually migrate into the particles to enhance nucleation on the surface, which further develops into Pt-rich crystalline islands. These crystalline islands continue to grow, connect to each other and self-orientate to form a single crystalline shell. Therefore, a core-shell structured particle is produced with a disordered core covered by crystalline shell. Finally, the crystallization will extend from surface to core *via* an Ostwald ripening process. Single crystals are formed after a longer reaction time.

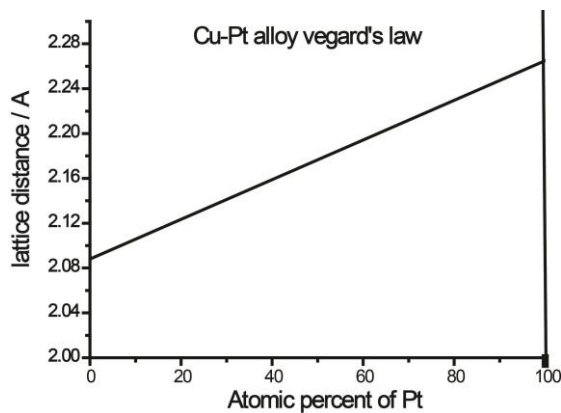
To our best knowledge, this is the first time a reversed crystal growth route has been demonstrated in nanoscale metallic crystallites. Uncovering the growth mechanism of CuPt nanocrystals expands our knowledge on the formation and growth of nanocrystals. It provides opportunity to tune the morphology of nanocrystals by simply controlling the reaction time. For instance, early stage intermediates with crystalline islands could be taken as very small crystallites loaded on support, which could probably exhibit promising catalytic performance with optimization.

6.4 Alloying Cu and Pt by varying nominal ratios

In this series of experiments, the nominal ratio of Cu and Pt precursors is varied and other experimental parameters, such as the reaction temperature and concentration of HDA remain constant. In the following text, products are denoted by the nominal molar ratio of Cu to Pt precursor in preparation. [e.g. (2: 8) Cu-Pt refers to product prepared with a nominal precursor of Cu: Pt = 2: 8.]

Composition of the product is determined by measuring *d*-spacings of nanoparticles, together with EDX analysis. XRD patterns are not used as the main characterization method here, because the XRD peaks are broad, overlapped and asymmetric, due to the small size and maybe continuous compositions of some nanoparticles as well. According to Vegard's law illustrated in **Scheme 6.2**, a linear relation exists in the plot of the crystal lattice parameter against the concentrations of the constituent elements if the specimens are true solid solutions.

By measuring the lattice distance of many solitary particles, we can determine whether they are Cu-rich or Pt-rich alloy and a rough Cu: Pt composition. Though deviations may exist in the real relationship between composition and lattice distances from ideal Vegard's law, the small difference are neglected in the following calculation. EDX can reflect the average chemical composition of particles in large areas.



Scheme 6.2 Variation of lattice distance of the (111) plane in Cu-Pt alloy as a function of Pt atomic percentage according to Vegard's law.

(7: 3) Cu-Pt is taken as an example here to demonstrate how to determine alloy composition by examining *d*-spacings with HRTEM images. Nanoalloys were synthesized with a Cu: Pt precursor ratio of 7: 3 for 1 h, 2 h and 16 h.

Specimen after reaction for 1 h

In most HRTEM images of the 1 h sample, it was hard to observe lattice fringes, which may be caused by poor crystallization because of the short reaction time and thick HDA layer on surface. EDX analysis indicates an average Cu content of 37 % and Pt of 63 %. The Cu: Pt is thus much lower than the nominal ratio of 7: 3. The HRTEM image in **Figure 6.5** shows a particle with a *d*-spacing of 2.20 Å, corresponding to (111) planes of Pt rich Cu-Pt alloy (Cu $d_{111} = 2.088$ Å, Pt $d_{111} = 2.265$ Å, CuPt $d_{111} = 2.176$ Å). Both EDX results and *d*-spacing measurements are consistent when the composition is concerned.

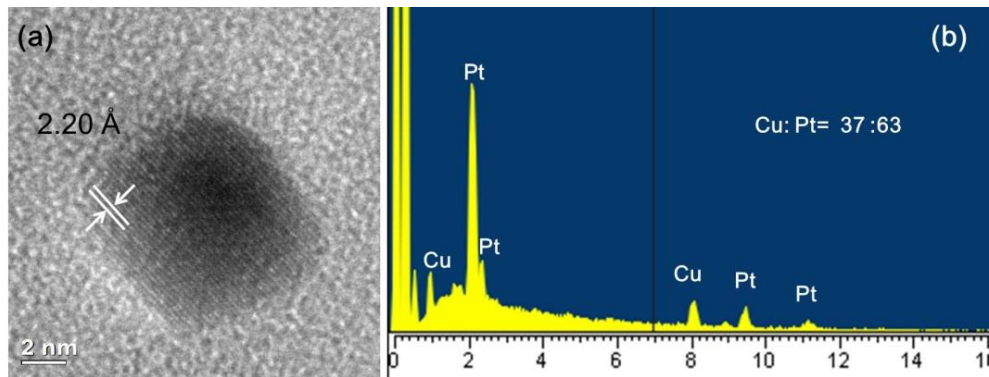


Figure 6.5 (a) HRTEM image and (b) EDX spectrum from 1 h sample (7: 3) Cu-Pt.

Specimen after reaction for 2 h

In the 2 h sample, most particles observed can be attributed to a composition of Cu_7Pt_3 , but many particles are pure Cu. Figure 6.6a gives a representative particle of Cu_7Pt_3 sample, with a d-spacing of 1.846 Å which corresponds to (200) planes of Cu_7Pt_3 . The particle in Figure 6.6b has two dimensional fringes g and h as indicated, which can be indexed to Cu (111) and (200) planes, respectively.

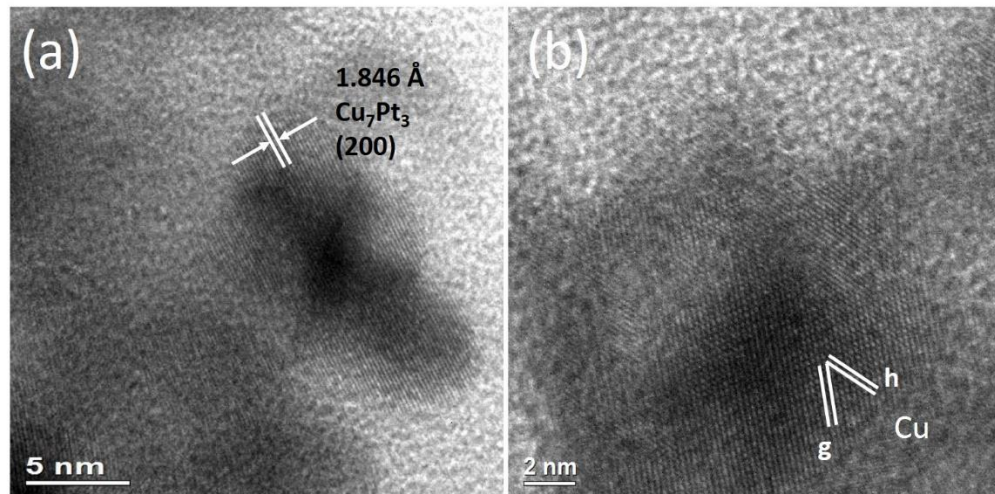


Figure 6.6 HRTEM images of the 2 h sample. (a) A particle with lattice d -spacing of 1.846 Å, corresponding to Cu_7Pt_3 (111) planes. (b) A particle with 2D fringes, $g = 2.086 \text{ \AA}$ and $h = 1.812 \text{ \AA}$, corresponding to Cu (111) and (200) planes, respectively.

The view direction is therefore along the [110] zone axis. The interplane angle is 48° smaller than the standard 55° angle. This could be caused by the distortion of imperfect nanocrystals.

Though many pure Cu nanocrystals were observed, the possibility that a Pt-containing core is covered by a Cu shell cannot be excluded. It is very likely that the Pt-containing core does not have lattice fringes but has a dark contrast due to its low crystallinity at this stage.

Specimen after reaction for 16 h

EDX analysis of the 16 h sample gives an average ratio Cu: Pt = 76: 24. After examining HRTEM images of the 16 h sample, it is found that most particles are Cu₇Pt₃, as shown in **Figure 6.7a**. A core-shell structure was also observed, as shown in **Figure 6.7b**. In the core area, the lattice inter-fringe distance is 2.141 Å, corresponding to (111) plane of Cu₇Pt₃, while the shell is pure Cu with a *d*-spacing of 2.088 Å. The HRTEM image in **Figure 6.7c** shows a Cu₇Pt₃ particle on the left, attached to a Cu particle whose hollow interior could be observed. Some pure Cu particles were present in the sample (**Figure 6.7d**).

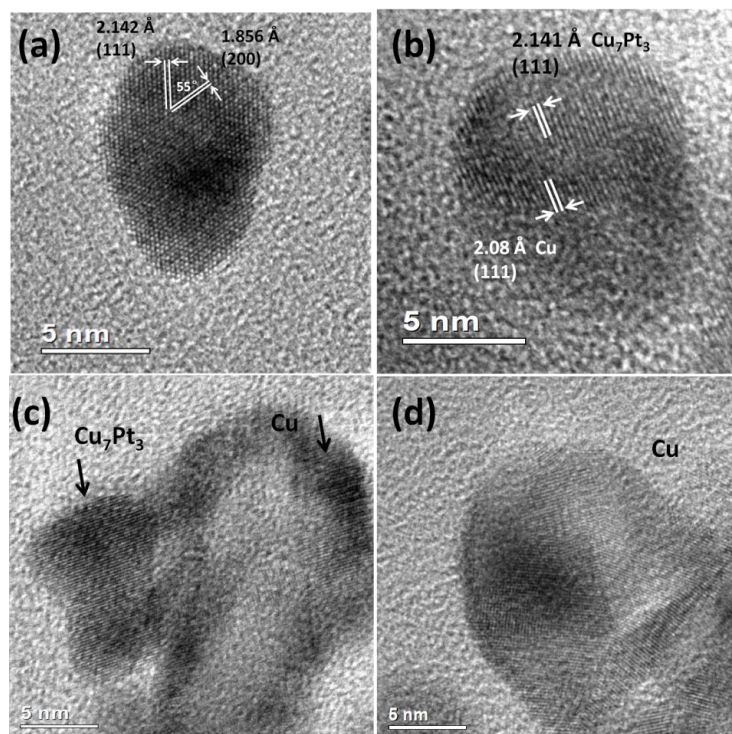


Figure 6.7 HRTEM images of particles from the 16 h sample. (a) A Cu₇Pt₃ particle with two dimensional fringes. (b) A core-shell particle, in which the Cu₇Pt₃ core is covered by a shell of pure Cu. (c) Two particles, the left particle is Cu₇Pt₃ alloy while the right one is Cu and (d) A Cu polyhedron.

The XRD patterns of 2 h and 16 h (7: 3) Cu-Pt samples in **Figure 6.8** are very similar. The peaks can be indexed to (111), (200) and (220) reflections of a face centered cubic lattice. Peaks of the 16 h sample are slightly sharper, owing to better crystallinity after a long reaction time. Both 2 h and 16 h samples exhibit asymmetric peaks. This is because the product contains both Cu-rich alloy and pure Cu, so the final shape of the peaks is a combination of at least two compositions. Pure Cu generates peaks with strong intensity, overlapping the peaks generated by small crystalline domains of Cu-rich alloy. In particular, the (111) peak of 16 h sample is more asymmetric than that of 2 h sample, as there exists a broad hump on the left shoulder of the (111) peak in 16 h XRD patterns. The hump is centered at low angles, which may originate from increased number of Cu₇Pt₃ nanocrystallites with prolonged reaction time due to mutual diffusion of Pt and Cu.

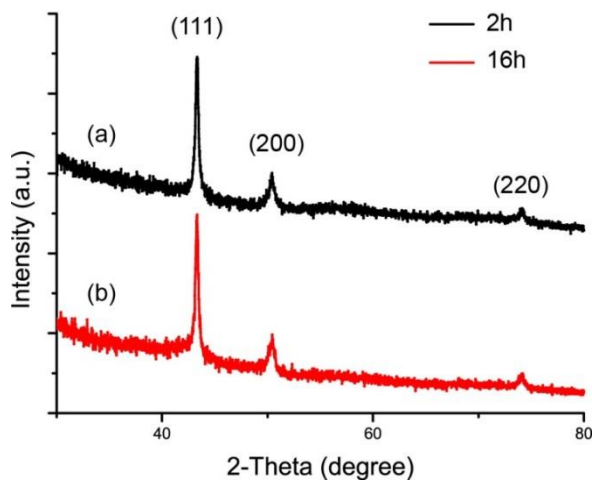


Figure 6.8 XRD patterns of the (7: 3) Cu-Pt sample after reaction for (a) 2 h and (b) 16 h.

Although a high concentration of Cu precursor was used in the synthesis, Pt-rich particles formed first (1 h sample). Pt(II) ions are more easily reduced than Cu(II). Furthermore, HDA, the surface ligands used in the preparation, has stronger interaction with Pt(acac)₂ as discussed before. The excess Cu ions in solution could go through homogeneous nucleation and be reduced to form pure Cu, or nucleate on the existing Pt-rich nanoalloys. For the latter, the Cu ions that are not fully reduced are more mobile, and can migrate into the Pt-rich nanoalloys to increase the Cu content. Some may form a Cu shell surrounding the alloy core. As reaction

time prolongs, Cu and Pt ions are fully reduced to be zero valent. At this stage, Kirkendall mass transport phenomenon^{17, 18} can occur, in which differences in mutual diffusion rates of two metal atoms results in the movement of the interface. The diffusion rate of Pt into Cu is faster ($3.96\text{--}8.28 \times 10^{-7} \text{ cm}^2 \text{ h}^{-1}$ at 960 °C) than that of Cu into Pt ($7.83\text{--}9 \times 10^{-8} \text{ cm}^2 \text{ h}^{-1}$ at 1041 °C).¹⁹ Thus the net flux is Pt diffusing into Cu vacancy. Some core-shell particles transform into uniform Cu₇Pt₃ alloy *via* diffusion of Pt atoms from core to Cu shell. Hollow interiors can be explained by the Kirkendall Effect as well as the surface crystallization process.

The main products prepared with other molar ratios of Cu and Pt precursors are summarized in **Table 6.1**. Based on the results in **Table 6.1**, it can be concluded (1) Pt-rich alloy is first produced under most reaction conditions, even in the sample with high nominal Cu concentration; (2) when Pt is in excess, CuPt 1: 1 alloy seems to be a favoured product. According to phase diagram,²⁰ Cu-Pt solid solution with continuous composition can be obtained at high temperature (above ~800 °C). There is no data below 300 °C. CuPt 1: 1 alloy forms in the range of Pt atomic percentage from 30 % to 90 %, while Cu₃Pt forms when Pt atomic concentration is below 30 %.

Our synthesis of Cu-Pt alloys was carried out at 200 °C with a polyol method. Our observation is consistent with phase diagram in the area of high Pt concentration, that is, CuPt is the main product with pure Pt as well. As for low Pt concentration in phase diagram, the Cu₃Pt alloy can have two different phase: one is (Fm $\bar{3}$ m) disordered alloy and the other is (Pm $\bar{3}$ m) ordered intermetallic phase. The ordered Cu₃Pt phase (Pm $\bar{3}$ m) is recognized in XRD by reflections at 24.1 °, 34.3 °, 55.7 ° and 61.5 °, which are not observed in our product (see **Figure 6.8**). XRD obtained is indexed to disordered fcc alloy (Fm $\bar{3}$ m). The calculated composition Cu₇Pt₃ is actually very close to Cu₃Pt. Pure Cu is also produced when Pt concentration is low.

Table 6.1 Main products and EDX results of the Cu-Pt bimetallic nanoparticles prepared with various Cu: Pt ratios after different reaction times.

Cu: Pt ratio	Time	Main products	EDX results of the alloy composition
7: 3	1 h	Pt rich alloy	Cu ₃₇ Pt ₆₃
	2 h	Cu rich alloy, Cu	Cu ₇₇ Pt ₂₃
	16 h	Cu rich alloy, Cu	Cu ₇₆ Pt ₂₄
1: 1	0.5 h	Pt rich alloy	Cu ₃₂ Pt ₆₈
	1.5 h	Pt rich alloy, CuPt	Cu ₂₆ Pt ₇₄
	10 h	CuPt	Cu ₅₁ Pt ₄₉
3: 7	1 h	Pt rich alloy, CuPt, Pt	Cu ₃₅ Pt ₆₅
	10 h	Pt rich alloy, CuPt, Pt	Cu ₃₁ Pt ₆₉
2: 8	0.5 h	CuPt, Pt	Cu ₁₈ Pt ₈₂
	2 h	CuPt, Pt	Cu ₁₈ Pt ₈₂
	16 h	CuPt, Pt	Cu ₁₇ Pt ₈₃

In summary, Cu-Pt nanoalloys with different compositions were prepared *via* a polyol process. In addition to alloyed particles, unalloyed Cu or Pt was also produced when either precursor is excessive. Under the synthesis conditions used in this study, Pt-rich particles are formed initially, probably owing to the strong interaction between HDA and Pt precursor. As reaction time is prolonged, Cu content in the nanoalloys increases by mutual atom diffusion. CuPt 1: 1 alloy is favored as the concentration of initial Pt precursor increases.

6.5 Size and composition dependent morphology of dealloyed nanoparticles

CuPt nanoparticles used for dealloying were synthesized in the presence of PVP with a molar ratio of Cu: Pt = 1: 1 and 3: 7, with a modified method reported by Zhou *et al.*³ As-prepared CuPt nanoparticles with different sizes and compositions were treated with 1 M H₂SO₄ to selectively dissolve Cu under mild conditions. Chemically dealloyed nanoparticles exhibit morphologies dependent on size and composition.

6.5.1 Dealloying of CuPt nanospheres

CuPt nanospheres were prepared with Pt(acac)₂ and CuSO₄ 5H₂O in the presence of PVP following a previously reported method.³ The sizes of nanospheres were uniform with an average diameter of 3.8 ± 0.3 nm (**Figure 6.9a**). The XRD pattern in **Figure 6.2b** shows broad and wide peaks, caused by the nanoscale size of the particles. No aggregation was observed in this system. This is because PVP is hydrophilic and cannot enhance aggregation with Pt(acac)₂ in the early stages. Consequently, formation of individual crystallites dominated the growth all the times. The crystal growth followed the classic route and crystallites with high crystallinity were produced.

After acid etching, the dealloyed CuPt products maintained their spherical shape with a slightly decreased size of 3.5 ± 0.3 nm in diameter (**Figure 6.9c**). Whereas, enlarged lattice *d*-spacings were observed in the dealloyed particles. Dealloyed nanospheres have a (111) *d*-spacing of 2.23 Å as shown in **Figure 6.9d** while that of as-prepared CuPt is 2.18 Å (**Figure 6.9b**). The increase of lattice *d*-spacing is caused by a decrease of Cu content in the chemically dealloyed nanoparticles. This is further confirmed by EDX analysis which shows a Cu: Pt ratio of 17: 83. Surprisingly, after the dissolution of nearly 80 % Cu out of the alloy the lattice fringes remain perfect without any detectable defects or lattice distortion. One assumption is

that the remaining Cu and Pt atoms re-arranged when Cu was slowly etched out. In this case, volume shrinkage could not be avoided.

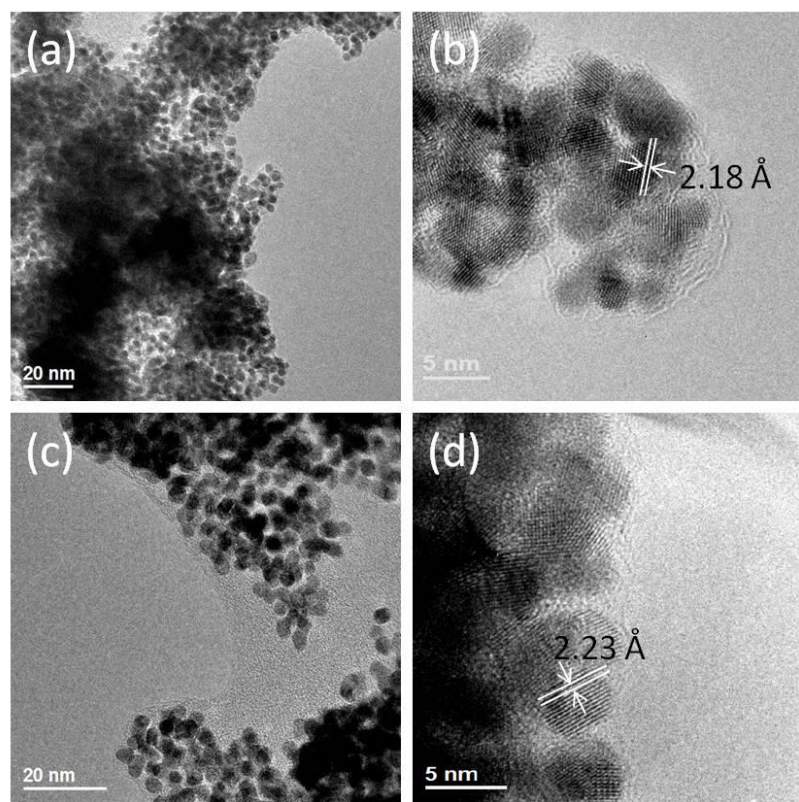


Figure 6.9 TEM and HRTEM images of CuPt nanospheres before and after dealloying. (a, b) As-prepared CuPt nanospheres and (c, d) dealloyed nanospheres.

The reported structure that a Cu-rich core is surrounded by Pt-rich shell in particles dealloyed by a electrochemical method¹³ is not observed in our product. We hypothesize that the dealloying conditions (1M H₂SO₄ at 80 °C) in the present work left the particles enough time to reorganize their structures.

6.5.2 Dealloying of Cu₇Pt₃ nanoparticles

When the nominal Cu: Pt precursor ratio was changed to 7: 3, polycrystalline Cu₇Pt₃ nanoparticles ~30 nm in size were produced under the same experimental conditions (**Figure**

6.10a). From the d -spacings in the HRTEM image in **Figure 6.10b**, it is found that the elemental distribution is not uniform in these particles. Most nanocrystallites on the surface are Cu₇Pt₃ alloy, but the crystallites in the core are mainly Cu. The d -spacings measured from the shell and core areas are 2.14 Å and 2.08 Å respectively, which can be assigned to (111) planes of Cu₇Pt₃ and pure Cu. The XRD pattern of the as-prepared Cu₇Pt₃ nanoparticles is displayed in **Figure 6.2c**. Compared with the pattern of CuPt nanospheres in **Figure 6.2b**, peaks of Cu₇Pt₃ nanoparticles have significantly shifted to a high angle due to the higher content of Cu. There is also a small Cu peak on the right shoulder of (111) reflection peaks, which comes from pure Cu in the Cu-rich cores. By varying the nominal Cu: Pt ratio, a core-shell structure has been produced with a Cu rich core and a polycrystalline shell containing Cu₇Pt₃ nanocrystallites.

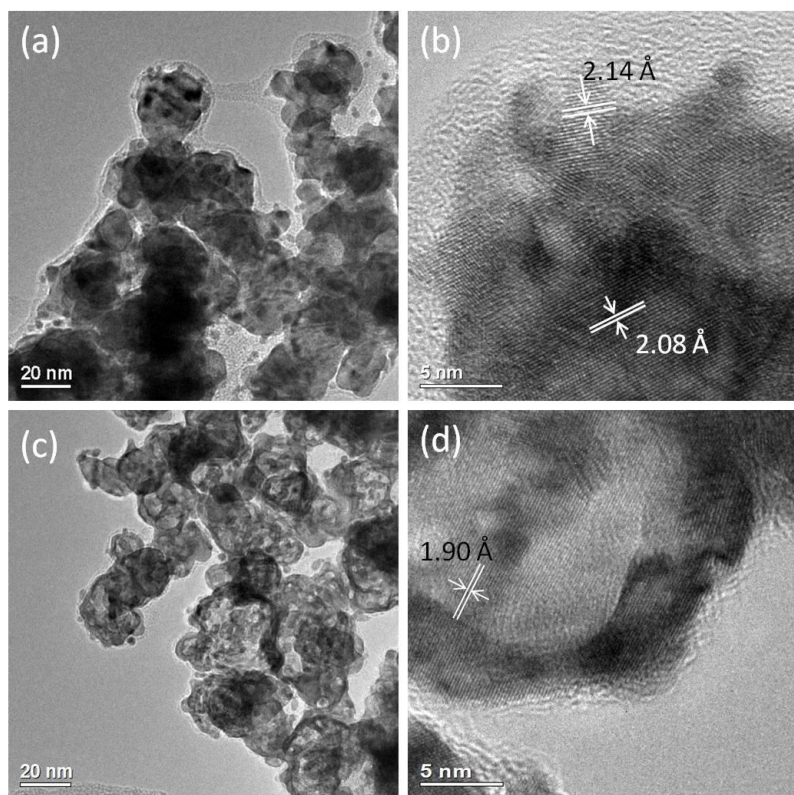


Figure 6.10 TEM and HRTEM images of Cu₇Pt₃ nanoparticles before and after dealloying. (a, b) As-prepared Cu₇Pt₃ polycrystalline core-shell particles and (c, d) hollow nanoparticles after dealloying.

After dealloying Cu₇Pt₃ particles under the same condition as CuPt 1: 1 nanospheres, all dealloyed products showed a hollow structure as seen in **Figure 6.10c**. This is because the original cores of the particles were Cu rich and most Cu atoms have been dissolved out of the interior area. As shown from a typical HRTEM image in **Figure 6.10d**, the shell has higher crystallinity after dealloying. Alloy nanocrystallites on the surface underwent a recrystallization process during dealloying, leading to the formation of single crystal areas extended in the shell. The observed fringes with a *d*-spacing of 1.90 Å can be indexed to the (200) planes of Cu-Pt alloy, which is consistent with the approximate Cu: Pt ratio of 4: 6 detected by EDX. As the size of Cu₇Pt₃ particles is big in comparison with the 3 nm ones, the large loss of Cu in core area leads to the formation of hollow particles.

In summary, when PVP was used as a capping agent, CuPt nanoparticles with different morphologies can be prepared by varying the nominal ratio of precursors. CuPt nanospheres were prepared with a ratio of Cu: Pt = 1: 1. When a high nominal ratio of Cu: Pt was used, large core-shell particles were produced where a Cu rich core covered a polycrystalline shell consisting of Cu₇Pt₃ nanocrystallites. Dealloying these nanoparticles by acid etching produced either solid or hollow particles. Dealloying CuPt nanospheres ~3 nm in size produced solid particles with volume shrinkage. On the other hand, dealloying of Cu₇Pt₃ nanoparticles lead to the formation of a hollow structure.

References

1. R. Ferrando, J. Jellinek and R. L. Johnston, *Chem. Rev.*, 2008, **108**, 845-910.
2. D. Xu, Z. P. Liu, H. Z. Yang, Q. S. Liu, J. Zhang, J. Y. Fang, S. Z. Zou and K. Sun, *Angew. Chem. Int. Ed.*, 2009, **48**, 4217-4221.
3. S. Zhou, B. Varughese, B. Eichhorn, G. Jackson and K. McIlwrath, *Angew. Chem. Int. Ed.*, 2005, **44**, 4539-4543.
4. S. Koh and P. Strasser, *J. Am. Chem. Soc.*, 2007, **129**, 12624-12625.

5. W. Ostwald, *Lehrbuch der Allgemeinen Chemie*, W. Engelmann Leipzig, Germany, 1896.
6. X. Chen, M. Qiao, S. Xie, K. Fan, W. Zhou and H. He, *J. Am. Chem. Soc.*, 2007, **129**, 13305-13312.
7. H. Greer, P. S. Wheatley, S. E. Ashbrook, R. E. Morris and W. Z. Zhou, *J. Am. Chem. Soc.*, 2009, **131**, 17986-17992.
8. X. F. Yang, J. X. Fu, C. J. Jin, J. A. Chen, C. L. Liang, M. M. Wu and W. Z. Zhou, *J. Am. Chem. Soc.*, 2010, **132**, 14279-14287.
9. H. Q. Zhan, X. F. Yang, C. M. Wang, J. Chen, Y. P. Wen, C. L. Liang, H. F. Greer, M. M. Wu and W. Z. Zhou, *Cryst. Growth Des.*, 2012, **12**, 1247-1253.
10. S. H. Xie, W. Z. Zhou and Y. Q. Zhu, *J. Phys. Chem. B*, 2004, **108**, 11561-11566.
11. J. R. G. Sander, D. K. Bucar, J. Baltrusaitis and L. R. MacGillivray, *J. Am. Chem. Soc.*, 2012, **134**, 6900-6903.
12. G. J. Hutchings, *Chemsuschem*, 2010, **3**, 429-430.
13. P. Strasser, S. Koh, T. Anniyev, J. Greeley, K. More, C. F. Yu, Z. C. Liu, S. Kaya, D. Nordlund, H. Ogasawara, M. F. Toney and A. Nilsson, *Nat. Chem.*, 2010, **2**, 454-460.
14. D. S. Wang, P. Zhao and Y. D. Li, *Sci. Rep.*, 2011, **1**.
15. W. Z. Zhou, *Adv. Mater.*, 2010, **22**, 3086-3092.
16. S. Saita and S. Maenosono, *Chem. Mater.*, 2005, **17**, 6624-6634.
17. Y. Yin, R. M. Rioux, C. K. Erdonmez, S. Hughes, G. A. Somorjai and A. P. Alivisatos, *Science*, 2004, **304**, 711-714.
18. H. J. Fan, U. Gosele and M. Zacharias, *Small*, 2007, **3**, 1660-1671.
19. A. K. Sinha, *Physical Metallurgy Handbook*, McGRAW-HILL, New York, 2003.
20. H. Baker and H. Okamoto, *Alloy Phase Diagrams*, ASM International, 1992.

Chapter 7 Conclusions and Future Work

Metallic nanomaterials are a focus of interest, owing to a range of fascinating potentials and their wide applications in both science and engineering. As the morphology of nanoparticles can strongly affect their performance such as catalytic activity, optical, electric or magnetic properties, shape-control is an important topic in the field of nanomaterials. In this project, the influence of surface ligands and solvents on the shape of nanoparticles is studied, to expand the knowledge of shape-control in metallic nanoparticles.

Despite that much effort has been put into the synthesis of nanomaterials in last few decades, research on growth process of nanoparticles is still limited. Our current understanding is not able to present a detailed evolution pathway for nanocrystals. The growth mechanisms of CuPt nanoparticles are studied in this project. This reveals other driving forces instead of conventional oriented attachment can dominate in the growth of nanocrystals.

Synergistic effect makes nanoalloys exhibit enhanced catalytic performances. Photocatalytic testing is carried out on CuPt nanorods in chapter 3, and electrochemical testing on CuPd nanowire networks in chapter 5, in which both alloys show outstanding activity. The CuPt nanorods and CuPd nanowire networks are potential candidates for efficient catalysts.

7.1 Conclusions

Most reported one dimensional nanowires or nanorods form in the following two manners: by deposition of atoms on seeds; or orientated attachment of primary units along one specific direction. In this study, CuPt nanorods are found to grow by coalescence of nanospheres, to form polycrystalline rods. The attachment relies on a stable layer of surface ligands, regardless of the crystallographic orientations of the nanospheres. The total energy of the surface ligands is crucial for their assistance of linear growth. Therefore, the ligand-ligand interaction on the surface determines the final length of the nanorods. The length of the nanorods can be

successfully tuned by varying the ratio, the alkyl chain length and the addition sequences of amine and acid ligands. This new mechanism reveals the importance of surface ligands in nanomaterial synthesis.

Ligand interaction can be varied in different solvents, which is an indirect control method. With all the other experimental parameters the same, different solvents produce particles with distinct morphologies. This is because enhancing the ligand-solvent interaction can reduce the interaction between ligands and nanoparticles, and vice versa.

Surfaces can be stabilized by capping with ligands. With the assistance of surface ligands, monolayer titanate nanosheets were successfully unrolled from nanotubes, which demonstrated the feasibility of this method. Various combinations of experimental conditions, surface ligands and solvents were tried, and the structure of titanate nanosheets is analyzed.

Three dimensional metallic nanostructures, with the advantages of high surface area, enhanced properties and reduced cost, have emerged as a highly intriguing class of materials. To the best of our knowledge, there are no reports of CuPd networks. A one-step synthesis of CuPd nanowire networks has been demonstrated. After investigation of the growth process, it is found that nanowires are formed by attachment of spherical particles and affected by interactions between metal and surface ligands. Preliminary tests of the CuPd nanowires towards ORR were carried out, and showed comparable performance to a Pt electrode. This general method can also be applied to prepare AgPd nanowire networks. Further galvanic replacement reaction can be carried out between as-prepared CuPd nanowires and gold salt, to produce porous nanowires.

Reversed crystal growth route was discovered in CuPt nanoparticles prepared in the presence of hexadecylamine in ethylene glycol. The aggregation was enhanced in this system and surfaces are the most active sites, where nucleation and crystallization start and then extend inwards. This is the first example of reversed crystal growth in nanoscale bimetallic particles. The size and composition dependent morphology of dealloyed particles are studied: dealloying of 3 nm CuPt nanospheres lead to a volume shrinkage; while dealloying Cu₇Pt₃

particles with Cu-rich core resulted in a hollow structure. Varying the nominal ratio of Cu and Pt precursors can produce nanoparticles with different degrees of alloying. The investigation of alloying and dealloying of CuPt nanoparticles provides practical guidelines for controlling the composition and morphology in Cu-Pt system *via* polyol process.

7.2 Future work

In the study of CuPt nanorods, only linear rods were produced in the intermediates, and a triangular shape particle was never observed. It is suspected that attachment of primary spherical units from a side surface is higher in energy and thus not favored in the growth. We cite the theoretical calculations of the energy difference in Au rod system, which has similar situation to ours. To better support the conclusion, simulation and calculation of energy in CuPt nanorod and triangular shape CuPt particles capped with ligands could be done to validate the assumption.

Titanate nanosheets were unrolled from nanotubes in the presence of surface ligands. Many tubes, however, remained their tubular shape in the product. The aim of future work is to increase the unrolling yield, and to find out the most efficient experimental conditions. Application of the monolayer titanate nanosheets could also be tried in photocatalysis, for example as catalysts for solar cells. The ultrathin nature of the nanosheets is very promising for the outstanding performance.

CuPd nanowire networks were applied as electrochemical catalysts for ORR, and the results presents a promising prospect of using them as a cheaper alternative to Pt. The 3D structure of nanowires was well maintained but activity reduced after higher numbers of CV cycles, therefore the further work would focus on improvement of the activity and stability of the CuPd network.

Publications

1. **Fengjiao Yu,*** Wuzong Zhou, Ronan M. Bellabarba, and Robert P. Tooze, *One-step synthesis and shape-Control of CuPd nanowire networks.* Nanoscale, 2014, 6, 1093-1098.
2. **Fengjiao Yu,** Xiaoxiang Xu, Christopher J. Baddeley, Ronan M. Bellabarba, Pascal Lignier, Robert P. Tooze, Federica Fina, John S. T. Irvine and Wuzong Zhou, *Surface ligand mediated growth of CuPt nanorods.* CrystEngComm, 2014, 16, 1714-1723.
3. **Fengjiao Yu** and Wuzong Zhou, *Alloying and dealloying of CuPt bimetallic nanocrystals.* Prog. Nat. Sci.: Mater. Intern., 2013, 23, 331-337.
4. Santosh Bikkarolla, **Fengjiao Yu**, Wuzong Zhou, Paul Joseph, Peter Cumpson, Pagona Papakonstantinou, *Three dimensional Mn₃O₄ network supported on nitrogenated graphene electrocatalyst for efficient oxygen reduction reaction in alkaline media.* ACS Catal., submitted.
5. Yanjun Fang, Zhenbo Xia, **Fengjiao Yu**, Jian Sha, Yewu Wang and Wuzong Zhou, *Formation mechanism of hollow microspheres consisting of ZnO nanosheets.* CrystEngComm, 2012, 14, 8615-8619.
6. Wuzong Zhou, **Fengjiao Yu**, Heather F. Greer, Zheng Jiang and Peter P. Edwards, *Electron microscopic studies of growth of nanoscale catalysts and soot particles in a candle flame.* Appl. Petrochem. Res., 2012, 2, 15-21.
7. Heather F. Greer, **Fengjiao Yu**, and Wuzong Zhou, *Early stages of non-classic crystal growth.* Sci. China Chem., 2011, 54, 1867-1876
8. Shin-Yu Chen, Liang-Chien Cheng, Chieh-Wei Chen, Po-Han Lee, **Fengjiao Yu**, Wuzong Zhou, Ru-Shi Liu, Yi-Yin Doand Pung-Ling Huang, *NIR-assisted orchid virus therapy using urchin bimetallic nanomaterials in phalaenopsis.* Adv. Nat. Sci.: Nanosci. Nanotechnol., 2013, 4, 045006.